Thermodynamics and Kinetics of Oxidation and Temperature Dependent Mechanical Characterization of Pure Indium Solder

BY

HARRY E. SCHOELLER

BSME, State University of New York at Binghamton, 2005

THESIS

Submitted in partial fulfillment of the requirements for
the degree of Masters of Science in Materials Engineering
in the Graduate School of
Binghamton University
State University of New York
2007

UMI Number: 1447566

UMI Microform 1447566

Copyright 2008 by ProQuest Information and Learning Company.
All rights reserved. This microform edition is protected against
unauthorized copying under Title 17, United States Code.

ProQuest Information and Learning Company
300 North Zeeb Road
P.O. Box 1346
Ann Arbor, MI 48106-1346

© Copyright by Harry Schoeller 2007

All Rights Reserved

Accepted in partial fulfillment of the requirements for
the degree of Masters of Science in Materials Engineering
in the Graduate School of
Binghamton University
State University of New York
2007

November 19, 2007

Dr. Junghyun Cho, Department of Mechanical Engineering, Binghamton University

Dr. Bruce Murray, Department of Mechanical Engineering, Binghamton University

Dr. Seungbae Park, Department of Mechanical Engineering, Binghamton University

Abstract

MicroElectroMechanical System (MEMS) devices often require low-temperature, fluxless soldering techniques due to their high temperature sensitivity and the performance requirements of specific components. While seeking the development of a soldering technology using pure indium, the major focus of this study is to assess the thermodynamics and kinetics of indium oxidation at various solder reflow environments that will ultimately provide a processing window for solder reflow and surface oxide cleaning.

The stability of oxidation and reduction reactions for indium is presented in terms of several thermodynamic models. The influence of pO_2, pH_2O, pH_2, pCO, pCO_2 on the location of oxidation and reduction zones is calculated using reaction equilibrium. Due to temperature limitations during processing of electronic packaging materials, pH_2O was found to be the critical parameter in creating a reducing environment using a hydrogen reaction. Additionally, because of the large enthalpy associated with the formation of In_2O_3, pO_2 was found to have little influence on thermodynamic equilibrium in both $H_{2(g)}$ and $CO_{(g)}$ reducing reactions.

Verification of the thermodynamic models is carried out by oxidation experiments performed in various environments. With a glove box employed for precise atmospheric control, pH_2O, pO_2, and pH_2 are varied to examine their effects on the oxidation and reduction behavior of indium. We also explore oxidation mechanisms at different stages of oxide growth, as well as at different regimes of temperature from 145˚C-220˚C. In particular, electron transport from indium to indium oxide is shown to be the rate

controlling mechanism under specific oxidizing conditions based on kinetics curves, and calculation of the activation energy.

For accurate thickness measurements of ultra-thin oxide films, a spectroscopic ellipsometer was employed. Ellipsometry is a non-destructive technique which uses polarized light to determine the thickness of thin films. Because ellipsometry is a very surface sensitive technique, indium samples were prepared by electro-chemical polishing to create a smooth sample surface.

The second part of this study focused on the mechanical characterization of indium and indium oxide using nanoindentation. Before systematic testing, the effect of quasi-static testing parameters was studied to determine their influence on elastic modulus and hardness results. Quasi-static unloading time was found to be the most influential parameter during testing. Fast unloading rates (2000μN/sec) were found to result in the most reproducible elastic modulus values, eliminating errors in the calculation of the contact stiffness caused by creep.

To document the change in mechanical behavior as a function of temperature, both elastic modulus and hardness were tested at 23˚C, 60˚C, 90˚C, and 120˚C using a nanoindentation heating and cooling stage. Indium's elastic modulus was found to decrease from 12.9GPa at 23˚C to 2.06GPa at 120˚C while indium's hardness decreased from 17.8MPa at 23˚C to 8.8MPa at 120˚C. Additionally, indium's time-dependent response was measured at room temperature via constant load nanoindentation creep tests.

Dedication

This thesis is dedicated to the memory of my mother and father

Acknowledgements

Endless thanks are in order to a number of people. First to all of my colleagues in AMML, Andy, Babak, Biplab, Dongmyung, Hyungsuk, Martin, Marvin, Oral, and Shijun, it has been a pleasure working with you all. To Dr. Magnus Bergkvist of NBTC for teaching me the “art” of ellipsometry and Dr. Jenkins for his help with XRD.

Thanks to the Office of Naval Research and the IEEC for funding this work, and Dr. Dan Jean and Dr. Mike Deeds of the Naval Surface Warfare Center for all of their helpful advice. I’d also like to thank my committee members Dr. Seungbae Park, and Dr. Bruce Murray for taking the time to review this work. To my advisor Professor Junghyun Cho, thanks for giving me the opportunity to work on this project and taking me on as a research assistant. All of your advice and our late evening chats helped me immeasurably.

Lastly and most of all I’d like to thank my fiancée Michelle whose love and understanding has been my driving force.

Table of Contents

ABSTRACT iv
DEDICATION vi
ACKNOWLEDGEMENTS vii
LIST OF TABLES x
LIST OF FIGURES xi

CHAPTER 1 - INTRODUCTION 1

CHAPTER 2 – THEORETICAL BACKGROUND 5

2.1 - INDIUM OXIDATION THERMODYNAMICS 5
2.1.1 - Oxidation Reaction 5
2.1.2 - Thermodynamics of Reduction using Hydrogen 14
2.1.3 - Thermodynamics of Reduction using Carbon Monoxide 19
2.1.4 - Thermodynamic Atmospheric Processing Program 23
2.2 - OXIDATION KINETICS 24
2.2.1 – Parabolic Oxidation Kinetics 24
2.2.2 – Inverse Logarithmic Oxidation Kinetics 24
2.2.3 - Logarithmic Oxidation Kinetics 25
2.2.4 - Rate Controlling Interface 26
2.2.5 - Electron and Ionic Transport 33
2.2.6 - Activation energy for Oxidation 35
2.2.7 - Derivation of Rideal and Wansbrough-Jones activation energy 39
2.2.8 - Space Charge Layer 42
2.2.9 - Derivation of Logarithmic Kinetic Equation 45
2.3 - NANOINDENTATION 48
2.3.1 - **Mechanics of Nanoindentation 50**
2.3.2 – Dynamic Nanoindentation 52
2.3.3 – Nanoindentation Creep 53
2.3.4 – Creep Mechanics 54

CHAPTER 3 – EXPERIMENTAL PROCEDURE 56

3.1 - SAMPLE PREPARATION 56
3.1.1 - Electro-Chemical Polishing 56
3.2 - OXIDATION EXPERIMENTS 59
3.2.1 - Oxidation of Indium in Air 59
3.2.2 - Oxidation of Indium under Controlled Environment 61
3.3 - THICKNESS MEASUREMENTS 64
3.3.1 - Ellipsometry 64
3.4 - MICROSTRUCTURAL CHARACTERIZATION 67
3.4.1 - Optical Microscopy 67
3.4.2 - Scanning Electron Microscopy 68
3.4.3 - AFM 68
3.5 - **X-RAY DIFFRACTION** 68
3.6 - MECHANICAL TESTING USING NANOINDENTATION 69
3.6.1 - H-Indent Calibration 71
3.6.2 - Air-Indent Calibration 71
3.6.3 - Tip Area Calibration 71
3.6.4 - Machine Compliance Calibration 72
3.6.5 - Quasi-Static Testing 73
3.6.6 - Heating and Cooling Stage 74
3.6.7 - Creep Testing 76

CHAPTER 4 – RESULTS AND DISCUSSION **78**
4.1 - OXIDATION OF INDIUM 78
4.1.1 – Oxidation of Indium in Air **79**
4.1.2 – Oxidation of Indium in a Controlled Environment **81**
4.2 – OXIDATION KINETICS 86
4.2.1 – Oxidation Kinetics in Air **87**
4.2.2 – Oxidation Kinetics in Glove Box Environment **91**
4.3 – ACTIVATION ENERGY 92
4.4 – REDUCTION OF INDIUM 94
4.4.1 – Reduction of Indium in Glove Box **94**
4.4.2 – Removal of Indium Oxide using Argon Plasma **97**
4.5 – MICROSTRUCTURE CHARACTERIZATION OF INDIUM AND INDIUM OXIDE 98
4.6 – X-RAY DIFFRACTION (XRD) 99
4.7 – MECHANICAL CHARACTERIZATION 101
4.7.1 – Optimization of Quasi-Static Nanoidentation Testing Parameters **102**
4.7.2 – In-situ High Temperature Nanoindentation Testing **107**
4.8 – NANOINDENTATION CREEP 112
4.9 – DYNAMIC INDENTATION OF In_2O_3 113
CHAPTER 5 – CONCLUDING REMARKS **116**
APPENDIX **119**
REFERENCES **121**

List of Tables

TABLE 2.1: THERMODYNAMIC PROPERTIES 7
TABLE 2.2: HEAT CAPACITY CONSTANTS 7
TABLE 2.3: WORK FUNCTIONS AND ACTIVATION ENERGIES FOR SEVERAL METALS 35

List of Figures

FIGURE 1.1: WETTING ANGLE VARIATION AT THE INERT ENVIRONMENT 2
FIGURE 1.2: INDIUM WETTING SHAPE WITH 4 NM OXIDE THICKNESS REFLOWED IN TWO DIFFERENT ENVIRONMENTS. LEFT, AIR. RIGHT, INERT ENVIRONMENT. 2
FIGURE 1.3: INDIUM JOINT STRENGTH AFTER INERT REFLOW. 3
FIGURE 2.1: CHANGE IN ENTHALPY RESULTING FROM THE CHEMICAL REACTION FORMING In_2O_3.. 8
FIGURE 2.2: CHANGE IN ENTROPY RESULTING FROM THE CHEMICAL REACTION FORMING In_2O_3.. 9
FIGURE 2.3: PLOT OF GIBBS FREE ENERGY FOR THE OXIDATION OF INDIUM. 10
FIGURE 2.4: ELLINGHAM DIAGRAM WITH OXYGEN ISOBARS FOR THE OXIDATION OF INDIUM 11
FIGURE 2.5: EQUILIBRIUM OXIDATION PARTIAL PRESSURE AS A FUNCTION OF TEMPERATURE 13
FIGURE 2.6: ELLINGHAM DIAGRAM WITH THE GIBBS FREE ENERGY OF THE H_2 REACTION SUPERIMPOSED 16
FIGURE 2.7: THERMODYNAMIC MAP OF OXIDATION AND REDUCTION ZONES AS A FUNCTION OF TEMPERATURE, HYDROGEN AND MOISTURE 17
FIGURE 2.8: THERMODYNAMIC MAP OF OXIDATION AND REDUCTION ZONES AS A FUNCTION OF TEMPERATURE, EQUILIBRIUM CONSTANT, AND OXYGEN PARTIAL PRESSURE. 19
FIGURE 2.9: THERMODYNAMIC MAP OF OXIDATION AND REDUCTION ZONES AS A FUNCTION OF TEMPERATURE, CO, AND CO_2 CONTENT 21
FIGURE 2.10: THERMODYNAMIC MAP OF OXIDATION AND REDUCTION ZONES AS A FUNCTION OF TEMPERATURE, pCO_2/pCO, AND OXYGEN PARTIAL PRESSURE. 23
FIGURE 2.11: ILLUSTRATION OF POSSIBLE RATE CONTROLLING INTERFACES.. 26
FIGURE 2.12: KINETICS CURVES ILLUSTRATING RATE DEPENDENCE ON CRYSTALLOGRAPHIC ORIENTATION OF PURE COPPER 28
FIGURE 2.13: KINETICS CURVES ILLUSTRATING RATE DEPENDENCE ON CRYSTALLOGRAPHIC ORIENTATION OF PURE IRON 30
FIGURE 2.14: KINETICS CURVES ILLUSTRATING RATE DEPENDENCE ON CRYSTALLOGRAPHIC ORIENTATION OF PURE NICKEL 30
FIGURE 2.15: EFFECT OF CURIE TEMPERATURE ON THE OXIDATION OF PURE IRON 31
FIGURE 2.16: EFFECT OF CURIE TEMPERATURE ON THE OXIDATION OF PURE NICKEL 32
FIGURE 2.17: SCHEMATIC OF ELECTRON FLOW FROM THE METAL TO THE OXIDE. 34
FIGURE 2.18: GRAPH SHOWING THE CHANGE IN PHOTOELECTRON WORK FUNCTION WITH TIME FOR DIFFERENT SILVER CRYSTAL FACES 38
FIGURE 2.19: EFFECT OF CURIE TEMPERATURE ON THE PHOTOELECTRONIC CURRENT FOR PURE NICKEL.. 39
FIGURE 2.20: SCHEMATIC OF POSITIVE SPACE CHARGE UPON INITIAL OXIDATION. 43
FIGURE 2.21: SCHEMATIC OF CHANGING SPACE CHARGE DUE TO THE ACCUMULATION OF ELECTRON AT LATTICE DEFECT SITES.. 44
FIGURE 2.22: SCHEMATIC OF A TYPICAL SOLDER JOINT 49
FIGURE 2.23: LOAD (P) VS. DISPLACEMENT (H) PLOT FOR A TYPICAL NANOINDENTATION LOADING AND UNLOADING CYCLE.. 50
FIGURE 2.24: LOAD (P) VS. DISPLACEMENT (H) PLOT FOR A DYNAMIC NANOINDENTATION TEST. THE DYNAMIC LOAD IS SUPERIMPOSED ON THE QUASI-STATIC LOAD TO MEASURE THE CONTACT STIFFNESS AS A FUNCTION OF DEPTH.. 53
FIGURE 3.1: SCHEMATIC OF ELECTROCHEMICAL POLISHER. 57
FIGURE 3.2: OPTICAL AND SEM IMAGES OF INDIUM MECHANICALLY POLISHED (A) (B) (C) , AND ELECTROCHEMICALLY POLISHED (D) (E) (F). 58
FIGURE 3.3: IMAGE OF HEAT TREATMENT SETUP 60
FIGURE 3.4: IMAGE OF TYPE K THERMOCOUPLE AND DIGITAL LOGGER. 60
FIGURE 3.5: IMAGE OF GLOVE BOX USED FOR ATMOSPHERIC CONTROL IN OXIDATION/REDUCTION EXPERIMENTS.. 62
FIGURE 3.6: DIGITAL TOUCH DISPLAY CONTROL PANEL FOR GLOVE BOX.. 63
FIGURE 3.7: IMAGE OF NANOFILM'S EP3 SPECTROSCOPIC ELLIPSOMETER 65
FIGURE 3.8: ILLUSTRATION OF PRINCIPLES OF ELLIPSOMETERY.. 66
FIGURE 3.9: PLOT OF CALCULATED DELTA VERSES MEASURED DELTA FOR INDIUM MELTED AT 400°C.. 66

FIGURE 3.10: IMAGE OF NIKON OPTICAL MICROSCOPE.....67
FIGURE 3.11: IMAGE OF HYSITRON NANOINDENTATION SYSTEM.....69
FIGURE 3.12: IMAGE OF THE NANOINDENTER STAGE AND TRANSDUCER LOCATED UNDER THE ENCLOSURE.. 70
FIGURE 3.13: MEASURED HEATING STAGE BERKOVICH TIP AREA FUNCTION.....72
FIGURE 3.14: QUASI-STATIC LOADING PROFILE TO DETERMINE ELASTIC MODULUS AND HARDNESS OF INDIUM.....74
FIGURE 3.15: HYSITRON'S HEATING AND COOLING STAGE ASSEMBLY.....75
FIGURE 3.16: SCREEN SHOT OF TRIBOTC CONTROL PANEL.....75
FIGURE 3.17: ALUMINUM SAMPLE HOLDER USED FOR HEATING AND COOLING STAGE.....76
FIGURE 3.18: QUASI-STATIC LOADING PROFILE FOR CONSTANT LOAD CREEP TEST.....77
FIGURE 4.1: INDIUM OXIDE THICKNESS AS A FUNCTION OF TEMPERATURE HEAT TREATED FOR 120MIN IN AIR.....81
FIGURE 4.2: INDIUM OXIDE THICKNESS AS A FUNCTION OF TEMPERATURE HEAT TREATED FOR 120MIN IN A GLOVE BOX ENVIRONMENT WITH pH_2O = 0.3PPM, pO_2 <0.1PPM, AND H_2 = 0.6%.....83
FIGURE 4.3: EVOLUTION OF INDIUM SHAPE AS A FUNCTION OF TEMPERATURE IN AIR.....84
FIGURE 4.4: EVOLUTION OF INDIUM SHAPE AS A FUNCTION OF TEMPERATURE IN GLOVE BOX WITH PH2O = 0.3PPM, PO2 <0.1PPM, AND H2 = 0.6%.....84
FIGURE 4.5: EVOLUTION OF INDIUM SHAPE AS A FUNCTION OF TEMPERATURE IN GLOVE BOX WITH PH2O = 5.5PPM, PO2 <0.1PPM, AND H2 = 0.6%.....84
FIGURE 4.6: THERMODYNAIC MAP OF OXIDATION AND REDUCTION ZONES WITH OXIDATION EXPERIMENTAL RESULTS SUPERIMPOSED.....86
FIGURE 4.7: GROWTH KINETICS OF INDIUM IN AIR AT 145˚C.....88
FIGURE 4.8: GROWTH KINETICS OF INDIUM IN AIR AT 180˚C.....89
FIGURE 4.9: GROWTH KINETICS OF INDIUM IN AIR AT 220˚C.....90
FIGURE 4.10: GROWTH KINETICS OF INDIUM IN GLOVE BOX WITH PO2 <0.1PPM, PH2O = 2.3PPM, H2 = 4% AT 130˚C.....91
FIGURE 4.11: GROWTH KINETICS OF INDIUM IN GLOVE BOX WITH PO2 <0.1PPM, PH2O = 2.3PPM, H2 = 4% AT 145˚C.....92
FIGURE 4.12: INITIAL ACTIVATION ENERGY EXPERIMENTALLY DETERMINED TO BE 62.6 KJ/MOL (.65EV).....93
FIGURE 4.13: THERMODYNAMIC MAP OF INDIUM REDUCTION AT 7PPM MOISTURE.....95
FIGURE 4.14: THICKNESS OF INDIUM OXIDE BEFORE AND AFTER REDUCTION EXPERIMENT.....96
FIGURE 4.15 STEREO-MICROSCOPE IMAGES OF INDIUM BEFORE AND AFTER REDUCTION EXPERIMENT.....96
FIGURE 4.16: THICKNESS OF INDIUM OXIDE BEFORE AND AFTER ARGON PLASMA TREATMENT AT 270 WATTS FOR 60 MIN.....97
FIGURE 4.17: LEFT, STEREO MICROSCOPE IMAGE OF ELECTROCHEMICALLY POLISHED 99.999% PURE INDIUM. RIGHT, OPTICAL IMAGE OF INDIUM GRAINS.....98
FIGURE 4.18 AFM IMAGES OF INDIUM OXIDE GROWN AT 1000 ˚C.....99
FIGURE 4.19: XRD PLOT OF INTENSITY VERSES 2THEATA FOR THE SAMPLE ANNEALED AT 153°C FOR 4 HOURS. THE PEAKS LABELED ARE FROM PURE INDIUM METAL (SUBSTRATE).....100
FIGURE 4.20: XRD PLOT OF INTENSITY VERSES 2THEATA FOR THE SAMPLE ANNEALED AT 200°C FOR 4 HOURS. THE PEAKS LABELED ARE FROM INDIUM OXIDE.....101
FIGURE 4.21: ELASTIC MODULUS OF INDIUM AS A FUNCTION OF QUASI-STATIC UNLOADING TIME.....103
FIGURE 4.22: STANDARD DEVIATION OF INDIUM'S ELASTIC MODULUS AS A FUNCTION OF QUASI-STATIC UNLOADING TIME.....103
FIGURE 4.23: HARDNESS OF INDIUM AS A FUNCTION OF UNLOADING TIME.....104
FIGURE 4.24: ELASTIC MODULUS OF INDIUM AS A FUNCTION OF MAXIMUM LOAD WITH A UNLOADING TIME OF 1 SEC.....106
FIGURE 4.25: HARDNESS OF INDIUM AS A FUNCTION OF MAXIMUM LOAD WITH A UNLOADING TIME OF 1 SEC.....106
FIGURE 4.26: ELASTIC MODULUS OF INDIUM AS A FUNCTION OF MAXIMUM LOAD AT 60˚C.....107
FIGURE 4.27: HARDNESS OF INDIUM AS A FUNCTION OF MAXIMUM LOAD AT 60˚C.....108
FIGURE 4.28: ELASTIC MODULUS OF INDIUM AS A FUNCTION OF MAXIMUM LOAD AT 90˚C.....109
FIGURE 4.29: HARDNESS OF INDIUM AS A FUNCTION OF MAXIMUM LOAD AT 90˚C.....110
FIGURE 4.30: ELASTIC MODULUS OF INDIUM AS A FUNCTION OF MAXIMUM LOAD AT 120˚C.....110
FIGURE 4.31: HARDNESS OF INDIUM AS A FUNCTION OF MAXIMUM LOAD AT 120˚C.....111
FIGURE 4.32: ELASTIC MODULUS OF INDIUM AS A FUNCTION OF TEMPERATURE.....112

FIGURE 4.33: HARDNESS OF INDIUM AS A FUNCTION OF TEMPERATURE.. 112
FIGURE 4.34: LOG-LOG PLOT OF STRAIN RATE VERSES STRESS TO DETERMINE INDIUM'S STRESS EXPONENT AT 23˚C. 113
FIGURE 4.35: DYNAMIC NANOINDENTATION PLOT OF ELASTIC MODULUS OF INDIUM OXIDE VERSES DISPLACEMENT 115

Chapter 1 – Introduction

Recent trends within the microelectronics industry away from the use of lead based solder because of environmental concerns has lead to much new research in the lead-free domain (Wable 2005). A lead-free solder of particular interest in the low temperature regime is pure indium solder, due to its low melting point (157ºC) and unique mechanical properties (Humpston 2005). Ductility and fatigue resistance of indium at low temperatures makes it an ideal candidate for compression seals in many packaging applications (Mil'shtein 1985). However, oxidation of indium, especially in fluxless applications reduces the reliability of the seal (So 2000). It is for this reason a systematic study of the oxidation and reduction behavior of indium is warranted.

In a joint study Kim et al. examined the effect of oxidation on solder joint reliability by performing wetting angle and lap shear experiments (Kim 2007). The influence of oxidation on wetting angle was quantified by reflowing indium samples with predetermined oxide thickness. Wetting angle was measured using a Wyco NT1100, Optical Profiling System. Figure 1.1 is a plot of wetting angle verses initial oxide thickness for indium solder reflowed in an inert environment. Indium's wetting on a Ti/Au pad was found increase, an indication of poor joint strength, with increasing initial oxide thickness.

Wetting was also found to depend heavily on reflow atmospheric conditions. Figure 1.2 shows two images (Kim 2007). On the right indium was reflowed in air, to the left indium was reflowed in an inert environment with pO_2 = 0.1ppm, pH_2O = 1ppm, and H_2 = 1.5%. The sample reflowed in the air environment showed very poor wetting where

the wetting angle could not be determined. On the right, the sample showed excellent spreading with a wetting angle equal to approximately 15°.

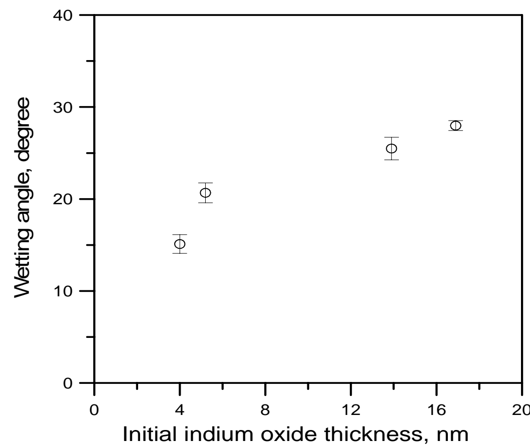

Figure 1.1 Wetting angle variations in the inert environment (Kim 2007).

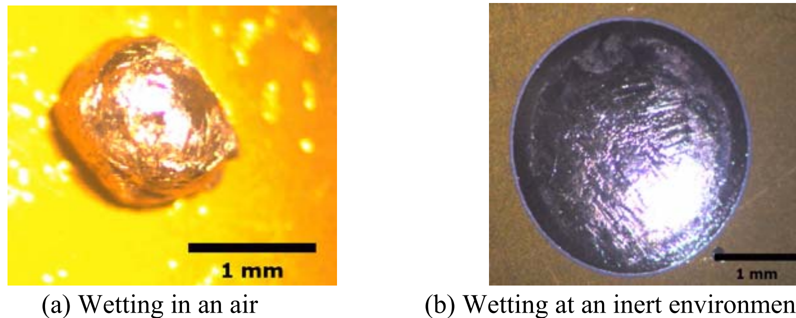

(a) Wetting in an air (b) Wetting at an inert environment

Figure 1.2 Indium wetting shape with 4 nm oxide thickness reflowed in two different environments. Left, air. Right, inert environment (Kim 2007).

For a more direct measurement of joint strength, indium with various initial oxide thicknesses was reflowed between two silicon substrates with Ti/Au metallization and tested by lap shear. Figure 1.3 shows the results of the lap shear test with joint strength plotted as a function initial indium oxide thickness. Similar to the wetting angle experiment, joint strength was found to increase with decreasing oxide thickness.

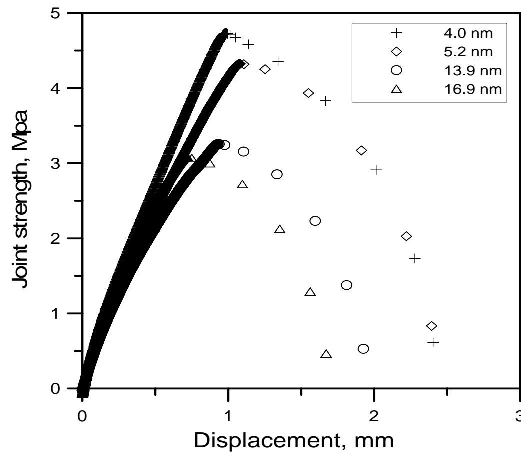

Figure 1.3 Indium joint strength after inert reflow (Kim 2007).

Information about the oxidation behavior in the temperature and time domain will help manufacturers develop reflow profiles, which reduce if not eliminate any oxides present thereby enhancing reliability. Apart from time and temperature there are many factors that can influence the oxidation behavior of metals, such as purity, surface roughness, microstructure, and environment (Kubaschewski 1962). In this study, much emphasis was placed on the influence of the reflow environment, particularly pO_2, pH_2O, pH_2 concentrations. Manipulation of these parameters along with temperature can change the reflow environment from oxidizing to reducing (Schoeller 2006).

Complimenting this thermodynamic study, an investigation into the kinetics of indium oxidation is presented. In air, the oxidation kinetics seems to follow a logarithmic relationship up to the temperature of 220ºC. This observation along with the experimentally measured initial activation energy of oxidation points to Uhlig's electron transport as the rate controlling mechanism for oxide growth (Uhlig 1956).

In addition to the effect of oxidation on solder joint reliability, the mechanical behavior of indium was characterized through nanoindentation techniques. Nanoindentation is particularly useful in that the volume of material tested is more representative of an actual solder joint, significantly lowering material and sample processing costs.

Chapter 2 – Theoretical Background and Calculations

2.1 -Indium Oxidation Thermodynamics

The oxidation of indium is a chemical reaction between pure indium and oxygen to form the stable metal oxide In_2O_3. Since it is a chemical reaction, both the thermodynamics and kinetics should be considered when characterizing the oxidation behavior. The thermodynamic behavior is studied to determine the type of reaction, and whether or not the reaction will occur. Specifically the value of the Gibbs free energy tells whether the reaction is oxidizing, reducing, or if the system is in equilibrium. Additionally, thermodynamic modeling can be used to study the effect of temperature, oxygen partial pressure, moisture, and hydrogen and their importance in oxide film growth. Reaction kinetics is studied to determine the rate at which the reaction occurs. Kinetics can also give some insight into the rate controlling mechanism of oxide growth/decomposition.

2.1.1 - Oxidation Reaction

Gibbs free energy (ΔG°) is frequently used to quantify the stability of a metal relative to its oxide. Its variation with temperature can be given by the follow relationship:

$$\Delta G^\circ = \Delta H^\circ - \Delta S^\circ T \tag{2.1}$$

where ΔH° is the standard change in enthalpy, ΔS° is the standard change in entropy and T is temperature (Gaskell 2003). For a metal to spontaneously oxidize, it must be

unstable relative to the oxide at the temperature of interest. Meaning the Gibbs Free Energy of the reaction must be negative at this temperature. The reaction of indium with oxygen to form indium oxide (In_2O_3) is given in the following equation:

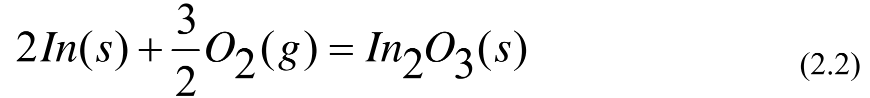

$$2In(s)+\frac{3}{2}O_2(g)=In_2O_3(s) \tag{2.2}$$

When this reaction is in equilibrium, meaning indium is neither oxidizing nor reducing ΔG° is equal to zero. Looking more closely at equation (2.1) it can be seen that the entropy and enthalpy terms "compete" with one another, and for equilibrium to occur the enthalpy should be sufficiently low and the entropy sufficiently high.

Enthalpy described as the "thermal energy of formation" contributes greatly to the stability of the system.

Mathematically, enthalpy at a given temperature is expressed as:

$$\Delta H_T=\Delta H_{298K}+\int_{298K}^{T} c_p dT \tag{2.3}$$

where ΔH_{298K} is the heat of formation of In_2O_3 at 298K (Gaskell 2003):

$$\Delta H_{298K}=\Delta H_{In_2O_3(298K)}-\Delta H_{In(298K)}-\frac{3}{2}\Delta H_{O_2(298K)} \tag{2.4}$$

and c_p is the experimentally measured heat capacity fit to the form:

$$c_p=A+b\cdot 10^{-3}T+c\cdot 10^{6}T^{-2}+d\cdot 10^{-6}T^{2} \tag{2.5}$$

All the necessary constants and other thermodynamic data were obtained from thermo-chemical data available in literature and are listed in table (2.1) and (2.2) (Yaws 1999).

Table 2.1 Thermodynamic Properties (Yaws 1999)

Compounds	**HeatCapacity (298K) (joules/K)**	**Enthalpy (298K) (joules)**	**Entropy (298K) (joules/K)**
In	18.9	0	57.8
In_2O_3	100.4	-925919	104.2
O_2	28.9	0	205.1
H_2	29.1	0	130.7
H_20	31.9	-241856	188.8
CO	28.5	-110528	197.6
CO_2	35.9	-393521	213.8

Table 2.2 Heat Capacity Constants (Yaws 1999)

Compounds	**Heat Capacity Constant A**	**Heat Capacity Constant B**	**Heat Capacity Constant C**	**Heat Capacity Constant D**
In(S)	10.962	39.84	-0.347	-
In (L)	29.87	-0.891	-	-
In_2O_3	122.68	8.1	-2.197	-
O_2	29.15	6.47	-0.184	-1.017
H_2	26.88	3.58	0.105	-
H_20	34.38	7.84	-0.423	-
CO	30.96	2.44	-0.28	-
CO_2	51.128	4.368	-1.469	-

The change in enthalpy as a function of temperature resulting from the chemical reaction forming In_2O_3 is illustrated in figure 2.1. The heat of formation of In_2O_3 can be calculated from a cycle on the enthalpy-temperature diagram.

For example, the change in enthalpy required to form In_2O_3 at 900K is given by:

$$\Delta H_T = \Delta H_{(A \rightarrow E)} + \Delta H_{(E \rightarrow F)} + \Delta H_{(F \rightarrow B)} + \Delta H_{(B \rightarrow D)} + \Delta H_{(D \rightarrow C)} \quad (2.6)$$

Where AE is the enthalpy needed to melt 1 mole of indium and heat (3/2) moles of O_2 to 430K. The discontinuity between E and F represents the latent heat of phase change (7273J) from $In_{(S)}$ to $In_{(L)}$. FB is the enthalpy required to heat 1 mole liquid indium and (3/2) moles of O_2 to 900K. The heat of formation of one mole In_2O_3 at 900K is given BD, and CD represents the change in enthalpy of In_2O_3 from 298K to 900K.

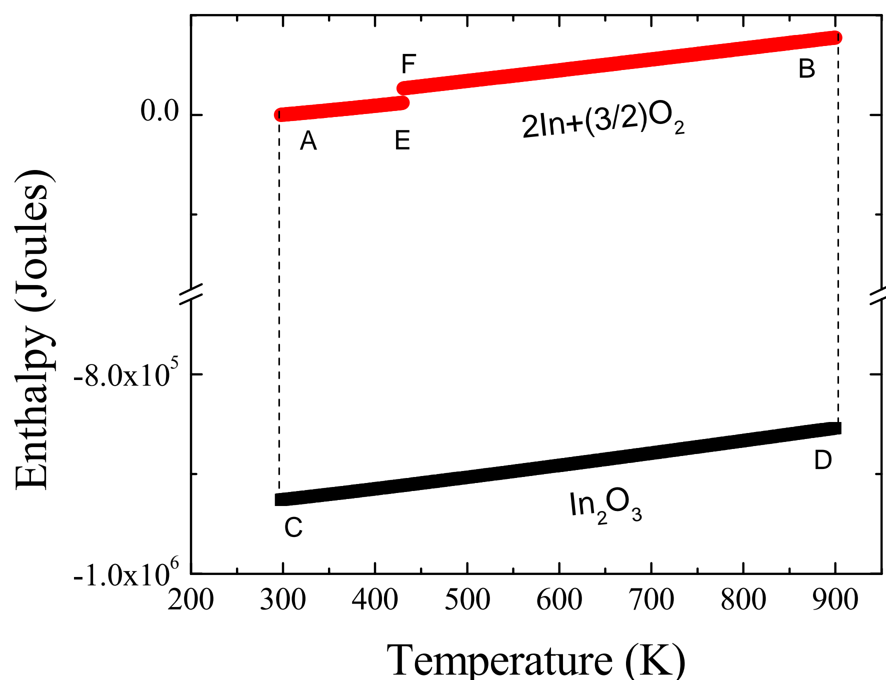

Figure 2.1: Change in enthalpy as a function of temperature resulting from the chemical reaction forming In_2O_3.

The change in entropy resulting from the formation of In_2O_3 is dealt with in a similar manner. From the second law of thermodynamics entropy is defined by:

$$\Delta S_T = \Delta S_{298K} + \int_{298K}^{T} \frac{c_p}{T} dT \quad (2.7)$$

where ΔS_{298K} is the entropy at 298K (Gaskell 2003). As was the case with enthalpy, the entropy of formation can be calculated graphically from the entropy-temperature diagram in figure (2.2).

$$\Delta S_T = \Delta S_{(A \to E)} + \Delta S_{(E \to F)} + \Delta S_{(F \to B)} + \Delta S_{(B \to D)} + \Delta S_{(D \to C)} \quad (2.8)$$

Where again, AE is the entropy needed to melt 1 mole of indium and heat (3/2) moles of O_2 to 430K. EF is the change in entropy resulting from the phase change (18.5 J/K) from $In_{(S)}$ to $In_{(L)}$. FB is the entropy from heating 1 mole liquid indium and (3/2) moles of O_2 to 900K. The change in entropy resulting from the formation of In_2O_3 BC is thought to be the result of the disappearance of 3/2 moles of oxygen gas during the reaction.

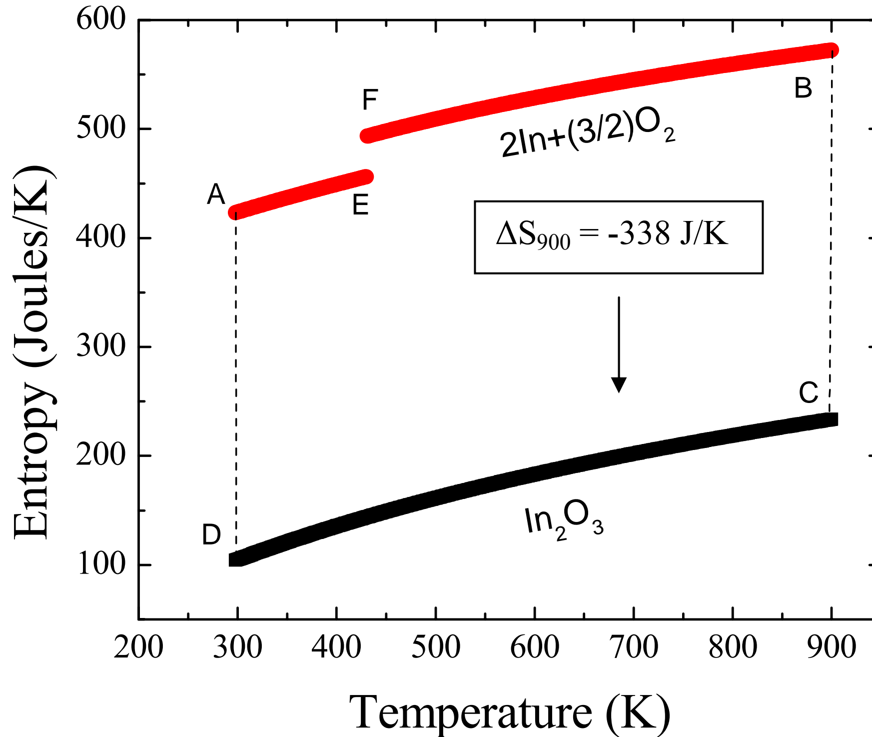

Figure 2.2: Change in entropy resulting from the chemical reaction forming In_2O_3.

As described earlier in equation (2.1) the stability of a reaction is determined by the Gibbs free energy which is a function of both enthalpy and entropy. This phenomenon is often illustrated by an Ellingham Diagram, which plots ΔG° verses temperature. A Gibbs free energy plot for the reaction of In with O_2 to form In_2O_3 is seen in figure 2.3. It is evident from this diagram that In_2O_3 is very stable relative to indium because of the negative value of ΔG. As seen in the earlier enthalpy-temperature diagram this is due to the very large heat of formation (ΔH) necessary to produce In_2O_3. It can also be clearly seen that indium oxide is stable from 0°C to indium's boiling point (2080°C) meaning that indium is always oxidizing at all applicable temperatures. If ΔG were to become positive for the reaction, indium would become stable and In_2O_3 would become unstable and spontaneously disassociate.

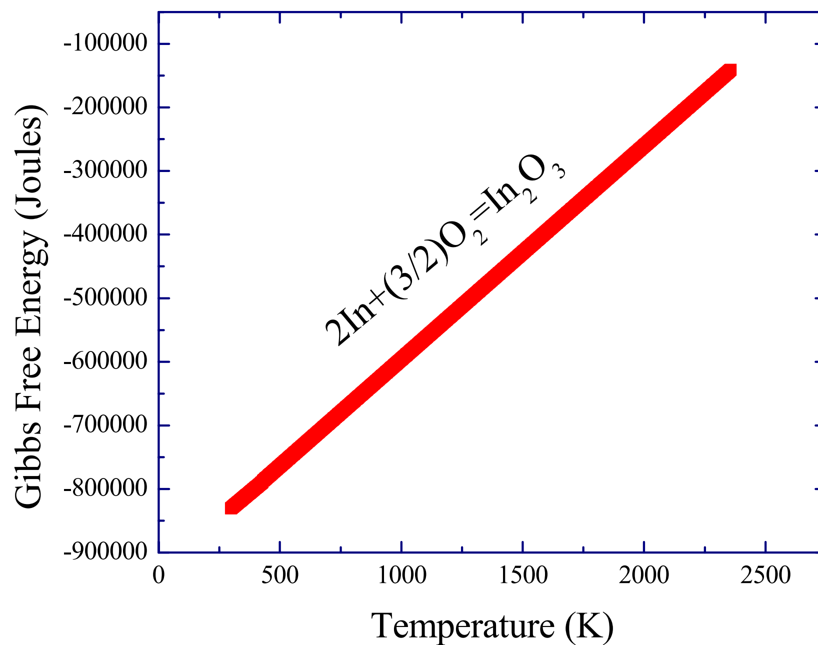

Figure 2.3: Plot of Gibbs free energy as a function of temperature for the oxidation of indium.

In addition to the observed effect of temperature, the Gibbs free energy or stability of the system is also dependent on the partial pressure of each of the constituents of the reaction (Gaskell 2003). Because of the very low vapor pressure of In and In_2O_3, their contributions can be neglected, and the partial pressure of O_2 can be assumed to be the pressure of the system. Therefore, to determine the effect of pressure on the oxidation reaction, the change in Gibbs free energy of 1 mole O_2 can be plotted for different pressures and the results superimposed on the Ellingham diagram shown in figure 2.4.

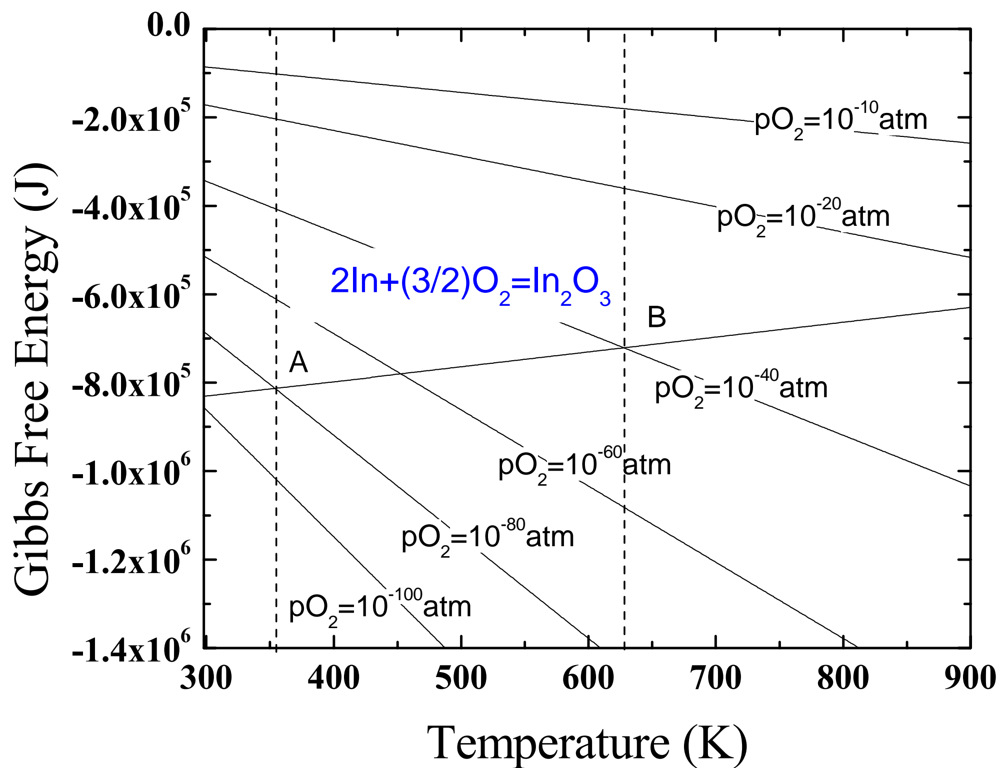

Figure 2.4: Ellingham diagram with oxygen isobars for the oxidation of indium

From figure 2.4, one can see the influence of pressure and temperature on the stability of the oxidation reaction. Point A is a coincident point of the free energy of 1 mole of

oxygen gas at 10^{-80}atm and the free energy of the oxidation reaction. Below point A the oxidation reaction does not occur because there is not enough oxygen present to react with indium. Above point A indium oxidizes until the available oxygen is used up and decreases to 10^{-80}atm. Also evident from figure 2.4 is the increase in free energy from point A to point B, meaning with increasing oxygen partial pressure there is a corresponding increase in Gibbs free energy. However in addition to the increase in oxygen partial pressure there is an increase in the equilibrium temperature which contributes greatly to the higher Gibbs free energy at point B.

To analyze this reaction according to reaction equilibrium of gaseous phases the solids must be express in terms of their vapor species, namely:

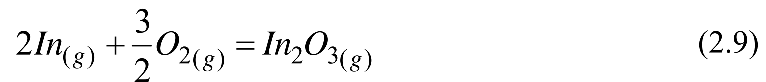

$$2In_{(g)} + \frac{3}{2}O_{2(g)} = In_2O_{3(g)} \tag{2.9}$$

Now applying reaction equilibrium to equation (2.9) gives:

$$\bar{G}_{In} + \frac{3}{2}\bar{G}_{O_2} = \bar{G}_{In_2O_3} \tag{2.10}$$

where G is the partial molar Gibbs free energy. Equation (2.10) can be written in terms of the equilibrium partial pressures in the following form:

$$G^\circ_{In} + RT\ln p_{In} + \frac{3}{2}G^\circ_{O_2} + \frac{3}{2}RT\ln p_{O_2} = G^\circ_{In_2O_3} + RT\ln p_{In_2O_3} \tag{2.11}$$

where G° is standard Gibbs free energy. Rearranging equation (2.11) to obtain the G° in terms of partial pressure at constant temperature gives:

$$G^\circ_{In_2O_3} - G^\circ_{In} - \frac{3}{2}G^\circ_{O_2} = -RT\ln\frac{p_{In_2O_3}}{p_{In}p_{O_2}^{\frac{3}{2}}} \tag{2.12}$$

Since,

$$\Delta G^\circ = G^\circ_{In_2O_3} - G^\circ_{In} - \frac{3}{2}G^\circ_{O_2} \tag{2.13}$$

and
$$K_p = \frac{p_{In_2O_3}}{p_{In} p_{O_2}^{\frac{3}{2}}} \tag{2.14}$$

with the K_p term representing the equilibrium constant. Finally it can be said:

$$\Delta G^\circ = -RT \ln K_p \tag{2.15}$$

To determine the oxygen partial pressure for which reaction (2.9) will not occur, the Gibbs free energy equation can be expressed as:

$$\Delta G^\circ = -RTLn\left(\frac{p_{In_2O_3}}{p_{O_2}^{3/2} p_{In}}\right) \tag{2.16}$$

where R is the gas constant, T is temperature, and p is partial pressure (Gaskell 2003).

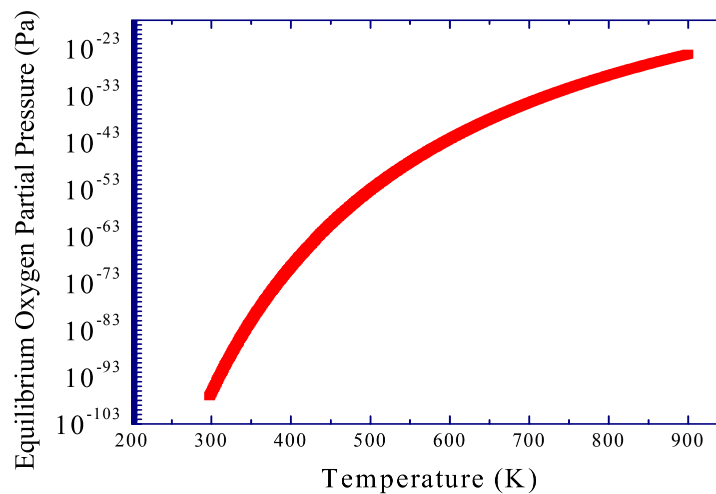

Figure 2.5: Equilibrium oxidation partial pressure as a function of temperature

From this equation the equilibrium oxygen partial pressure was calculated to be 10^{-98} atm at room temperature. Since it is unrealistic to achieve such a partial pressure by purification or under vacuum, another reaction is needed to increase the oxygen partial

pressure to a reasonable level. A plot of equilibrium oxygen partial pressure as a function of temperature is shown in figure 2.5.

2.1.2 Thermodynamics of Reduction using Hydrogen

As discussed earlier, because the equilibrium oxygen partial pressure is extremely low in the practical reflow range for indium solder, a separate reaction is needed halt or reverse the oxidation process. Often an etching gas such as hydrogen (H_2) or carbon monoxide (CO) is added to the reflow environment to increase the oxygen equilibrium partial pressure.

First, consider the reduction of In_2O_3 using pure hydrogen gas:

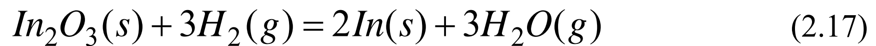

$$In_2O_3(s) + 3H_2(g) = 2In(s) + 3H_2O(g) \tag{2.17}$$

which is the combination of two reactions namely:

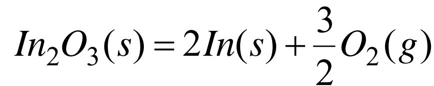

$$In_2O_3(s) = 2In(s) + \frac{3}{2}O_2(g)$$

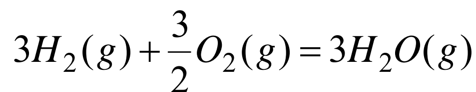

$$3H_2(g) + \frac{3}{2}O_2(g) = 3H_2O(g)$$

To determine stability of the reduction reaction (2.17), Gibbs free energy can be expressed in terms of the partial pressure of H_2O and H_2 as follows:

$$\Delta G^\circ = -RTLn\left(\frac{{p_{H_20}}^3}{{p_{H_2}}^3}\right) \tag{2.18}$$

Just as the effect of oxygen partial pressure was investigated by superimposing the Gibbs free energy of 1 mole of oxygen gas at various pressures against the Gibbs free energy of

the oxidation reaction, the Gibbs free energy of the reduction reaction (2.17) can be superimposed on the Gibbs free energy of the oxidation reaction to determine the ratio of moisture to hydrogen which results in equilibrium (Gaskell 2003). Figure 2.6 shows the Ellingham diagram with the Gibbs Free Energy of the reduction gas reaction superimposed. From figure 2.6 it can be seen the slope of the reduction reaction steadily decreases as $pH2O/pH_2$ decreases from 5 to approximately 0.001 after which the slope becomes negative. This behavior can be attributed to changing entropy of the system. As the hydrogen content is increased or the water vapor concentration decreases there is a decrease in the entropy of the system. Another point which can be drawn from figure 2.6 is the decreasing equilibrium temperature with the decreasing pH_2O/pH_2 ratio. With a pH_2O/pH_2 ratio equal to 5 the equilibrium temperature is approximately 1800K well above the reflow range. However, when the pH_2O/pH_2 ratio decreases to 0.00001 the equilibrium temperature decreases to approximately 423K, well within the reflow range. This highlights the importance of the addition of a separate reducing reaction in obtaining system equilibrium. By manipulating the pH_2O/pH_2 ratio equilibrium can be reached below indium's melting point whereas with out the reduction reaction equilibrium is practically impossible.

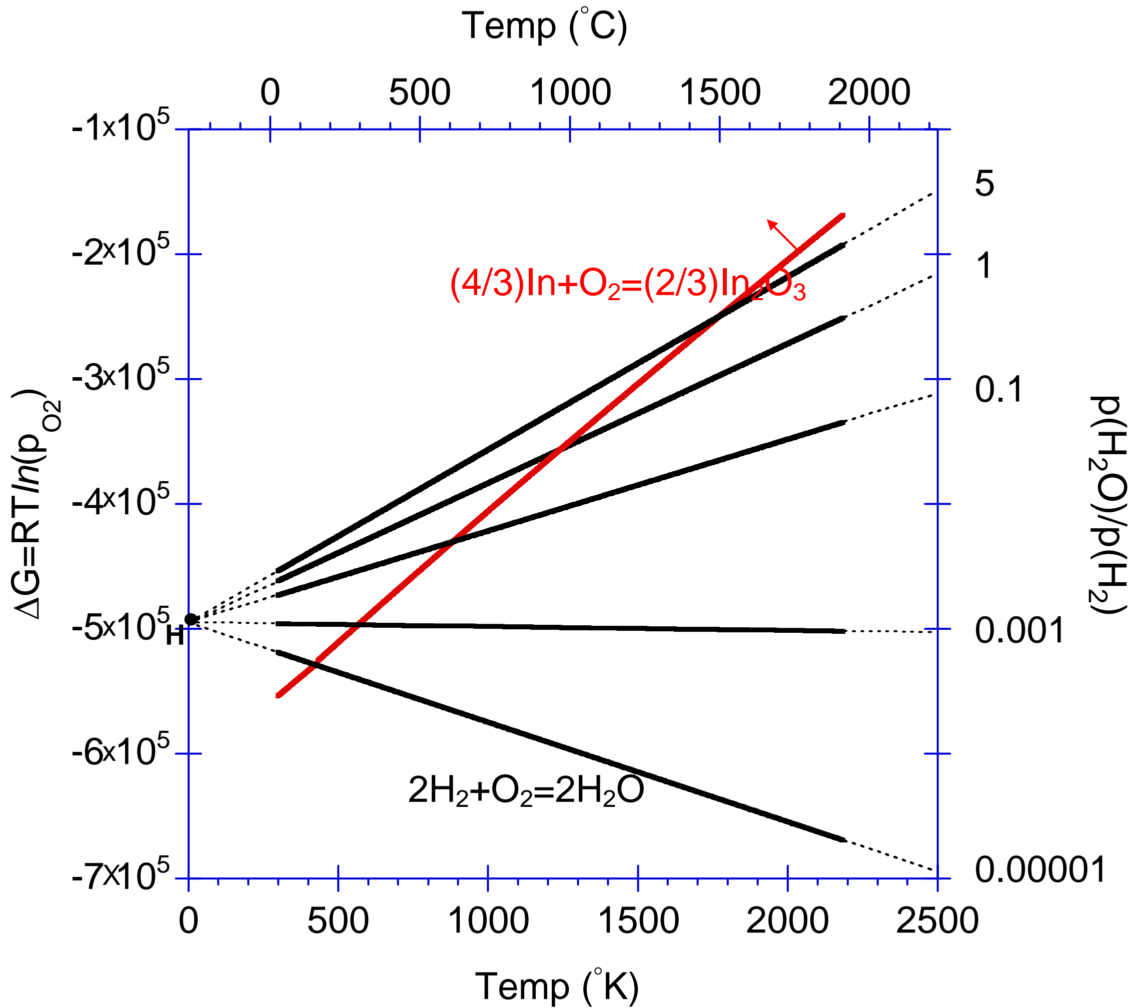

Figure 2.6: Ellingham diagram with the Gibbs free energy of the H_2 reaction superimposed

So at equilibrium ($\Delta G^{\circ} = 0$) the oxygen partial pressure is directly related to the ratio of moisture to hydrogen. This exemplifies the often-overlooked fact of moistures importance in the reflow environment. The plot below, figure 2.7, of percent hydrogen verses temperature with $H_2O_{(g)}$ isobars, illustrates the effect of moisture on the thermodynamic location of the reduction zone. Each of the moisture isobars in figure 2.7 represents where the system is in equilibrium at a particular $H_2O(g)$ partial pressure. This can be related to figure 2.2 in that as the $H_2O(g)$ partial pressure increases there is an increase in entropy which in turn raises the equilibrium temperature. Also because the

relationship of hydrogen to temperature is a decaying exponential, hydrogen in the safe working range has less of an effect the equilibrium temperature than $H_2O(g)$ partial pressure. As the moisture content increases the reduction zone shifts further and further to the right. Therefore at higher moisture concentrations higher temperatures are needed to achieve equilibrium or reduction. For example at 200°C and 4% hydrogen, only environments with < 1ppm moisture are reducing. With 10ppm moisture and 4% hydrogen the temperature would have to be increased to 300°C to enter the reduction zone. Since processing temperatures greater than 300°C are impractical because of component degradation, low moisture concentrations are imperative in the fluxless reflow of pure indium solder.

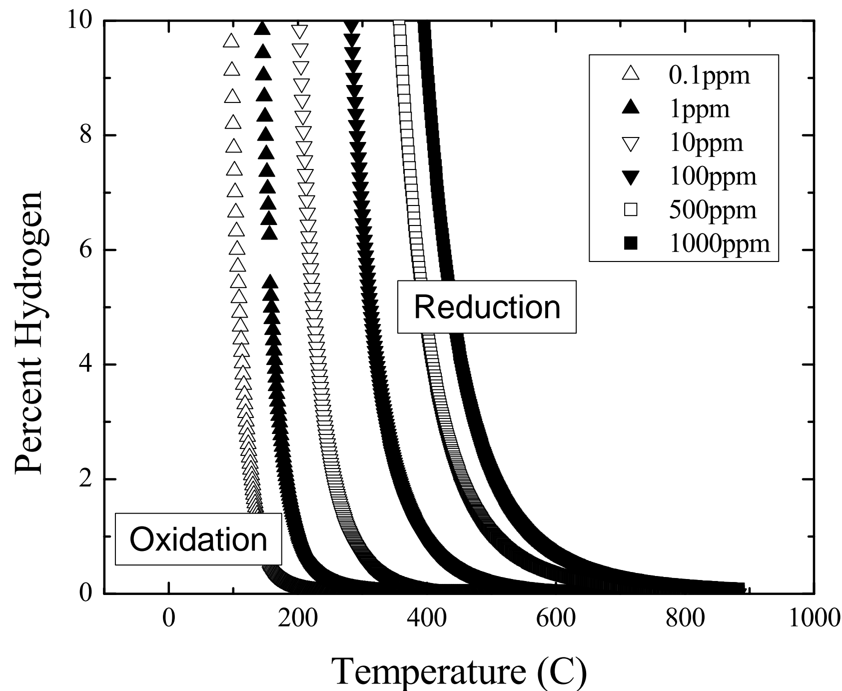

Figure 2.7: Thermodynamic map of oxidation and reduction zones as a function of temperature, hydrogen and moisture.

In contrast the effect of oxygen partial pressure doesn't have much of an impact on the thermodynamic location of the oxidation and reduction zones. The plot in figure 2.8 relates the effect of oxygen partial pressure and pH_2O/pH_2 to the location of the oxidation and reduction zones. In figure 2.8 the curve labeled $In_2O_3 + 3H_2 = 2In + 3H_2O$ shows the variation of pH_2O/pH_2 with temperature for the reduction reaction. Oxygen partial pressure isobars are superimposed on the reduction reaction to determine the location of equilibrium based on four variables namely pH_2, pH_2O, pO_2, and temperature. In figure 2.8 it can be seen that the equilibrium oxygen partial pressure (in the reasonable working range) has little impact on pH_2O/pH_2 or the equilibrium temperature. For example, reducing the oxygen partial pressure from 10^{-9} atm to 10^{-20} atm only results in a slight change in the pH_2O/pH_2 equilibrium ratio. This is due to the logarithmic relationship between $pH2O/pH_2$ and temperature.

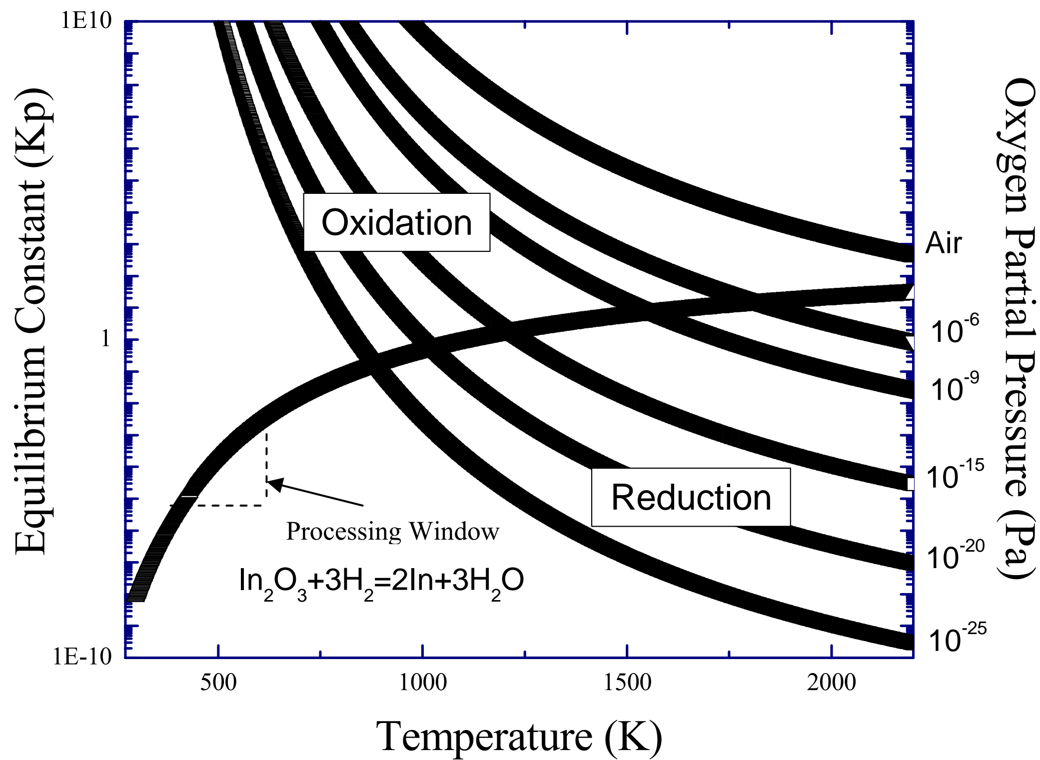

Figure 2.8: Thermodynamic map of oxidation and reduction zones as a function of temperature, equilibrium constant, and oxygen partial pressure.

Also highlighted in figure 2.8 is a reasonable processing window for an environment obtainable using current glove box technology. The lower limit for pH_2O/pH_2 is 10^{-6} which corresponds to pH_2O = 0.1ppm and H_2 = 10%. The upper limit for temperature 573K corresponds to the maximum reflow temperature for pure indium solder.

2.1.3 Thermodynamics of Reduction using Carbon Monoxide

The previous section discussed the reduction of a metal oxide In_2O_3 by controlling the concentration of two key gases, $H_{2(g)}$ and $H_2O_{(g)}$. Similarly the reaction of carbon monoxide (CO) with oxygen to form carbon dioxide (CO_2) can also be used to create a

reduction environment. The equation below shows the chemical equation for the reduction of In_2O_3 using $CO_{(g)}$:

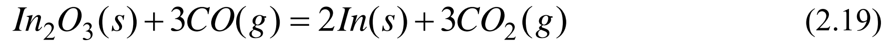

$$In_2O_3(s) + 3CO(g) = 2In(s) + 3CO_2(g) \quad (2.19)$$

which is the combination of two reactions:

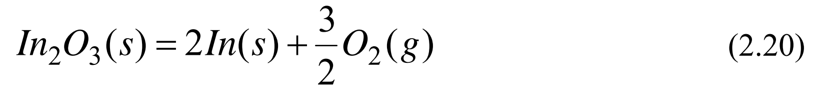

$$In_2O_3(s) = 2In(s) + \frac{3}{2}O_2(g) \quad (2.20)$$

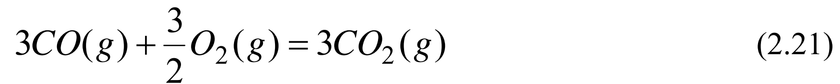

$$3CO(g) + \frac{3}{2}O_2(g) = 3CO_2(g) \quad (2.21)$$

Again the Gibbs free energy can be expressed as a function of partial pressures by:

$$\Delta G^\circ = -RTLn\left(\frac{p_{CO_2}{}^3}{p_{CO}{}^3}\right) \quad (2.22)$$

So just as was the case with $H_{2(g)}$ the equilibrium temperature is highly dependent on the ratio of partial pressures of the gaseous constituents. A significant difference between the reducing agents $H_{2(g)}$ and $CO_{(g)}$ is the enthalpy of the reaction. Since (2.21) has a larger enthalpy, lower pCO_2/pCO ratios or lower temperatures can be used to create a reducing environment (Gaskell 2003). In this sense $CO_{(g)}$ can be a more efficient reducing agent than $H_{2(g)}$. Figure 2.9 is a thermodynamic oxidation/reduction map of reaction 2.19. $CO_{2(g)}$ isobars from 0.1ppm to 300ppm (concentration of $CO_{2(g)}$ in air) were plotted as a function $CO_{(g)}$ and temperature to determine the location of the oxidation and reduction zones.

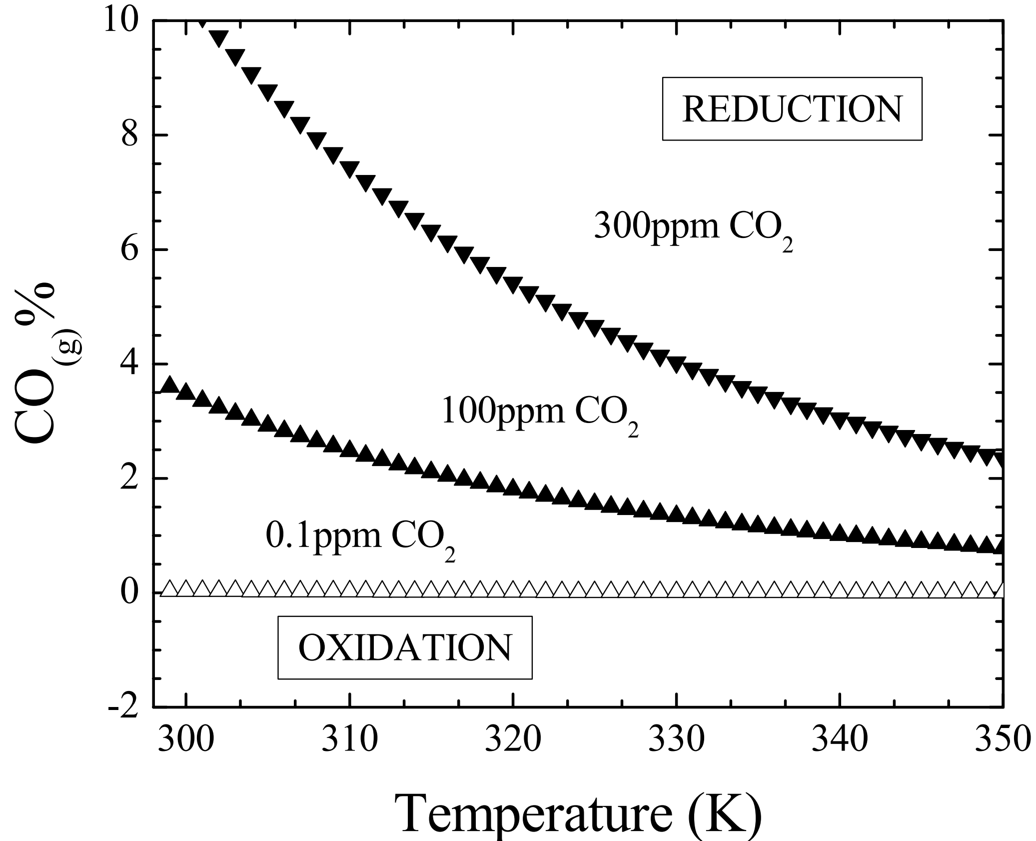

Figure 2.9: Thermodynamic map of oxidation and reduction zones as a function of temperature, CO and CO_2 content.

At 0.1ppm $CO_{2(g)}$, a partial pressure easily obtained by vacuum or purification in glove box, only 0.04% $CO_{(g)}$ is needed at 298K to achieve a reducing environment. As the processing temperature is increased the amount of $CO_{(g)}$ necessary to create a reducing environment decreases. With an increasing atmospheric concentration of $CO_{2(g)}$ both higher temperatures and $CO_{(g)}$ concentrations are needed to disassociate In_2O_3. In air (300ppm) only ~12% $CO_{(g)}$ is needed to achieve equilibrium at 298K. This is significant because reduction is now possible without the use of a vacuum of other purification

techniques. As the temperature is increased to 360K, well below indium's melting point, only 2% $CO_{(g)}$ is needed.

Lastly, the influence of oxygen partial pressure on the $CO_{(g)}$ reduction reaction is gauged on a oxidation/reduction map. In figure 2.10 the curve labeled $In_2O_3 + 3H_2 = 2In + 3H_2O$ shows the variation of pCO_2/pCO with temperature for the reduction reaction. Oxygen partial pressure isobars are superimposed on the reduction reaction to determine the location of equilibrium based on pCO_2, pCO, pO_2, and temperature. Just as with $H_{2(g)}$ the equilibrium oxygen partial pressure has little impact on pCO_2/pCO or the equilibrium temperature. However a significant difference between the $H_{2(g)}$ and $CO_{(g)}$ is the size and location of the atmospheric processing window. Due to the greater enthalpy and consequently greater Gibbs free energy of the $CO_{(g)}$ reduction reaction, relatively larger pCO_2/pCO can be used to etch In_2O_3. This can be visualized by comparing the vertical position of the In_2O_3 reduction reaction in $H_{2(g)}$ (figure 2.8) and $CO_{(g)}$) (figure 2.10) environments. The pH_2O/pH_2 ratio varies from 10^{-9} to 10^{-3} as the temperature is increased from 298K-573K whereas the pCO_2/pCO varies from 10^{-3} to 10^{-1}. The later partial pressure ratios are more easily obtained at lower processing temperatures. One caveat to the proceeding analysis is thermodynamics only indicates whether or not a reaction will occur, no information is given about the rate at which the reaction would occur.

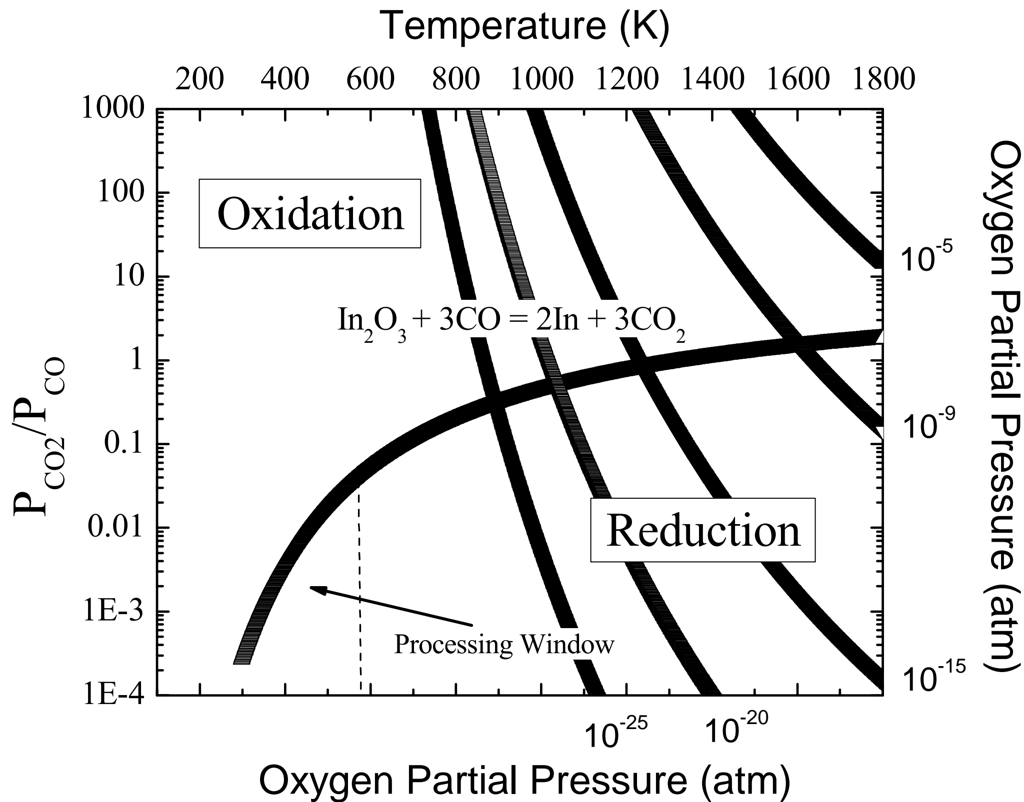

Figure 2.10: Thermodynamic map of oxidation and reduction zones as a function of temperature, pCO_2/pCO, and oxygen partial pressure.

2.1.4 Thermodynamic Atmospheric Processing Program

A simple thermodynamic code was created to help manufacturers easily determine the appropriate atmospheric conditions for reflow and processing environments. The code, generated in Matlab, asks the user a series of questions, and based on the parameters entered, and in return estimates the temperature or atmospheric conditions needed in order to create a reducing environment.

2.2 Oxidation Kinetics

To this point we've only discussed the thermodynamics of oxidation and reduction, now we must discuss the rate at which these reactions occur. There are several kinetics models for oxidation which functionally describe how the oxides grow. These models can be narrowed down to three main categories, parabolic, inverse logarithmic, and logarithmic (Evans 1943).

2.2.1 Parabolic Oxidation Kinetics

Parabolic growth rate kinetics can be most easily described as when the diffusion of ions through oxide is the rate controlling mechanism (Fromhold 1969). Wagner's oxidation equation below shows the oxide growth dependence on time.

$$d^2 = A_1 e^{-Q/kT} t + A_2 \quad (2.23)$$

Where d is oxide thickness, Q is activation energy, k is a rate constant, t is time and A_1 and A_2 are constants.

2.2.2 Inverse Logarithmic Oxidation Kinetics

Cabrera and Mott's theory of oxidation says that the growth of an oxide layer follows an inverse logarithmic relationship:

$$1/X = A - BLn(t) \tag{2.24}$$

where X is oxide thickness and A and B are constants (Fromhold 1969). Here the rate controlling mechanism is the flow of metal ions. Growth of the native oxide layer on many metals such as copper, iron and indium can be described by this mechanism (Eldridge 1972).

2.2.3 Logarithmic Oxidation Kinetics

First Introduced by Tammann and Koster 1922 (Tammann 1922) and then expanded by Uhlig in 1956, logarithmic growth kinetics describes the phenomenon of decreasing oxide growth rate (dy/dt) as a function of time, in the low temperature regime (Uhlig 1956). Differing from parabolic kinetics which is thought to be controlled by the diffusion of ions through the oxide lattice, logarithmic kinetics is thought to be controlled by a space charge layer limiting the flow of electrons from the metal to the oxide. As electrons accumulate in the oxide the space charge become less negative and the flow of electrons slows, resulting in the logarithmic growth behavior.

According to theory the process first begins when oxygen molecules are physically adsorbed on the metal surface, attached only by weak Van Der Waals bonds. Subsequently, an activation energy barrier must be overcome before oxygen is chemisorbed on the metal surface. This activation energy described by Uhlig is the Rideal and Wansbrough-Jones relation (Rideal 1929). After the energy barrier is

overcome and the oxygen is chemisorbed, a metal-oxide complex is formed. Finally there is a sublimation of the metal-oxide complex to form the oxide lattice. The logarithmic model has been used to describe the oxidation kinetics of several metals such as Fe, Cr, Al, Cu, Pb, and W (Uhlig 1956).

2.2.4 Rate Controlling Interface

Before the mechanism of logarithmic oxidation can be fully understood, the location of the rate controlling interface must be identified. After creation of the oxide lattice two interfaces are present, one is the oxygen-oxide interface, and the other at the oxide-metal interface as can be seen in figure 2.11.

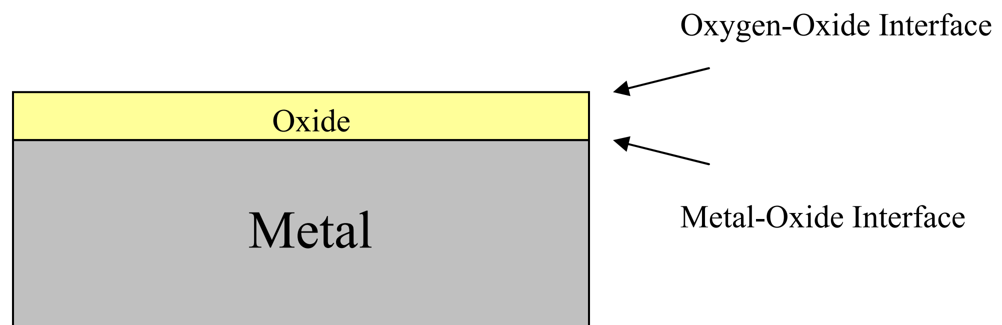

Figure 2.11: Illustration of possible rate controlling interfaces.

Several studies have shown the oxide-metal interface to be the rate-controlling interface whenever thin films are formed. One such study conducted by Chattopadhyay found a discontinuity in the activation energy and rate constant at the allotropic temperature of cobalt (Chattopadhyay 1969). At 722K cobalt experiences a phase transformation from

hexagonal closed packed HCP to face entered cubic FCC. Accompanying this phase transformation is a sudden increase in activation energy, and decrease in the rate constant. The increase in activation energy can be explained by the higher rate of electron emission for the HCP structure opposed to the FCC structure which translates into higher oxidation rates. At the phase transformation temperature there's a reduction in electron emission and more electrons become trapped at defect sites in the oxide lattice leading to slower oxide growth rates.

Another convincing piece of evidence of rate control at the metal-oxide interface comes from studies showing anisotropic oxidation behavior. The most common examples illustrating the effect of crystallographic orientation on oxidation rates are those from iron, copper and nickel.

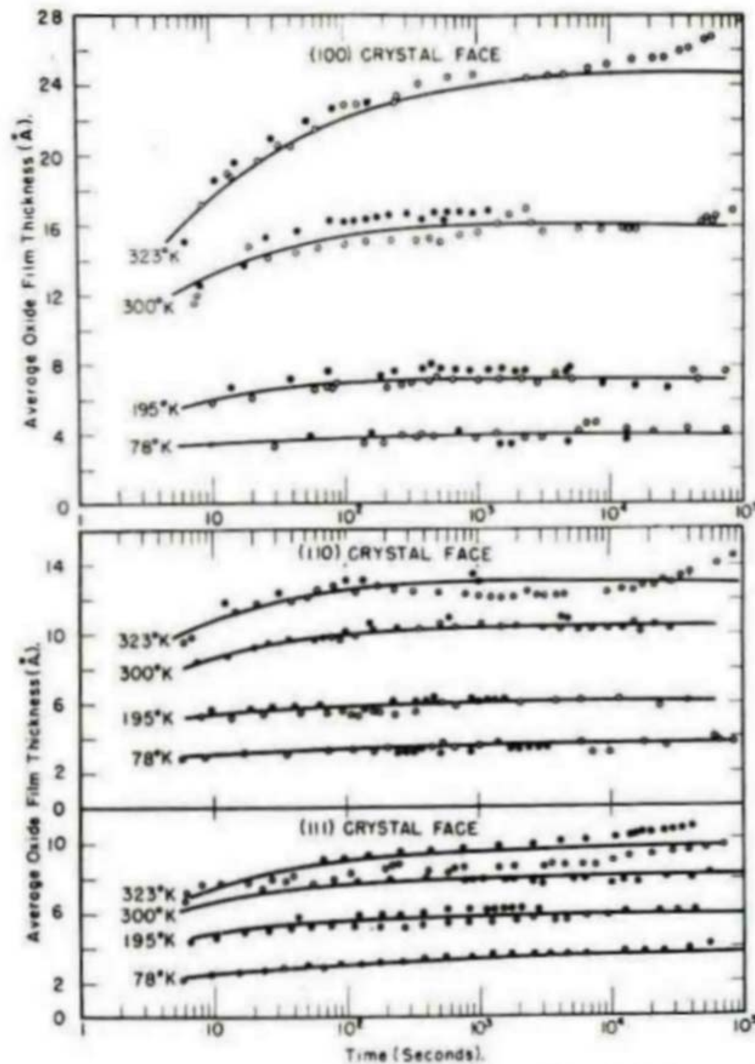

Figure 2.12: Kinetics curves illustrating rate dependence on crystallographic orientation of pure copper (Rhodin 1951).

Rhodin's study clearly proved the dependence of oxide growth on both crystal orientation and temperature. Figure 2.12 shows logarithmic oxide growth on copper from 78K to 323K on three different crystal faces (100), (110), and (111) as a function of time (Rhodin 1951). At 78K only a negligible difference can be detected between the three kinetics curves. However at 323K large differences can be found in the rate of oxidation and the overall oxide thickness following the trend (100) > (110) > (111). This trend

does not coincide with the plane of greatest packing density in an FCC structure where (111) > (100) > (110). Other researchers concluded the difference is related to the easy from which atoms can be removed from a particular plane (Tick 1971). The rate of oxygen uptake for different orientations has also been suggested as a possible reason for anisotropic oxidation, however, Armitage et al. showed oxygen uptake to follow an alternate trend (110) > (100) > (111). It's more likely perhaps a combination of factors is responsible for anisotropic oxidation instead of one specific reason (Armitage 1981).

Another example of anisotropic oxidation comes from Graham et al. in their study of single crystal and polycrystalline iron (Graham 1970). Figure 2.13 shows oxidation kinetics curves for polycrystalline iron and single crystals (110), and (112) at 100˚C. Oxide thickness was found to be highly dependent on crystal orientation where polycrystalline > (110) > (112). Similar investigations by Wagner, and Sewell and Cohen also found anisotropic oxidation for iron (Wagner 1961).

Nickel has also shown an orientation dependence on oxidation behavior. Graham et al. studied the oxidation behavior of electrochemically polished nickel in polycrystalline form and for several single crystals at 873K. Figure 2.14 shows highly anisotropic oxidation behavior. However in this study, the polycrystalline form did not show the greatest oxidation rate or thickness. It was shown (100) > polycrystalline > (111) > (112), where oxidation kinetics and overall thickness was found to be dependent on the overall number of defect sites. Defect sites act as diffuse paths for ions meaning the greater the number of defects the greater the oxidation rate (Graham 1973)

.

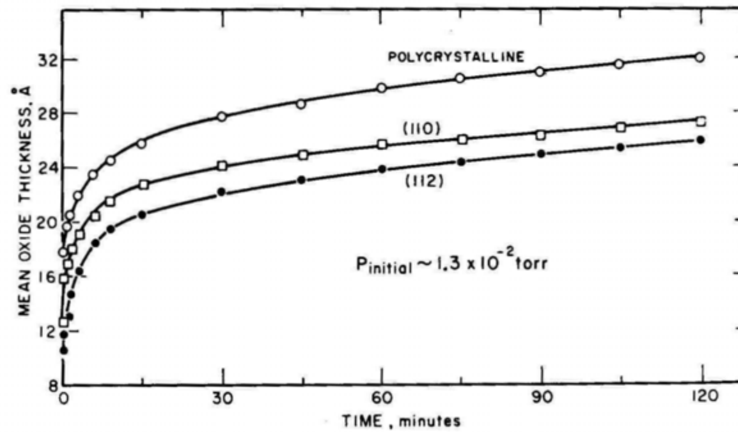

Figure 2.13: Kinetics curves illustrating rate dependence on crystallographic orientation of pure iron (Graham 1970).

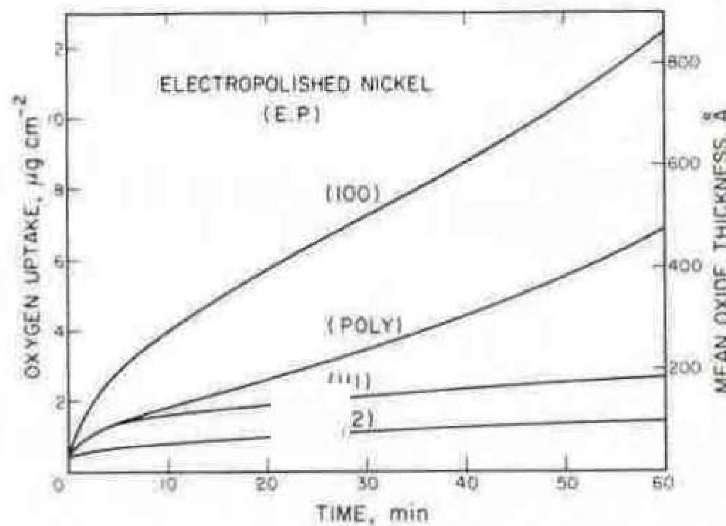

Figure 2.14: Kinetics curves illustrating rate dependence on crystallographic orientation of pure nickel (Graham 1973).

Additional supporting research of oxidation rate control at the metal-oxide interface comes from investigations of oxidation above and below the Curie temperature. West describes the Curie temperature as the temperature above which a material no longer displays ferromagnetic characteristics. Above the Curie temperature the magnetic moments become misaligned destroying the magnetic behavior of the material, at which

point the material becomes paramagnetic (West 2005). The finding of oxidation dependence on magnetic behavior was crucial in the theory of logarithmic oxidation controlled by electron emission because it deals specifically with the electronic state of the material and its affect on oxidation.

In the 1960's Measor's group studied the effect of magnetic behavior on the oxidation of iron (Measor 1964). The oxidation kinetics was examined between 973K-1173K for pure iron which has a curie temperature of 1028K.

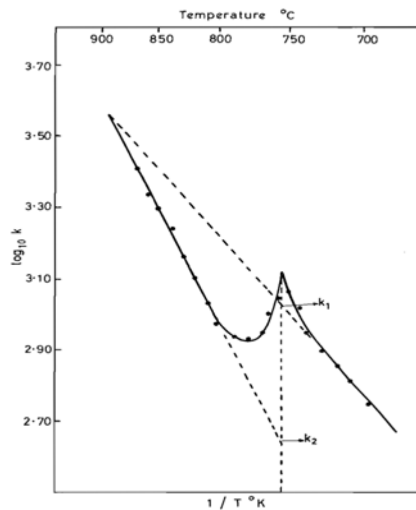

Figure 2.15: Effect of Curie temperature on the oxidation of pure iron (Measor 1964).

Figure 2.15 is a plot of the logarithm of the rate constant verses 1/Temperature for the oxidation of pure iron. A marked difference in the activation energy can be seen from the change in slope after passing the Curie temperature. Results found a sharp reduction in the activation energy after passing the Curie temperature from 21,700cal/mole before the Curie temperature to 33,100cal/mole after the Curie temperature. Chatterjee et al. surmised the difference was due to an alteration in the electronic state which changes the surface potential at the metal-oxide interface (Chatterjee 1976). This finding is supported by the work of Cardwell who found the emission of electron reduces

significantly after the Curie temperature (Cardwell 1953). The reduction in electron emission was attributed to a reduction in free electron density in the paramagnetic state. So the increase in activation energy coupled with the reduction in density of free electrons ultimately leads to a lower oxidation rate in the paramagnetic state.

Rocaries et al. performed a similar study on pure nickel. Nickel like iron has a Curie temperature in which the magnetic behavior changes from ferromagnetic to paramagnetic. Again if oxidation is controlled by electron emission, there should be a change in the oxidation behavior at this point because of the drastic change in electronic state at this temperature. Figure 2.16 is a plot of the rate constant verses 1/temperature for pure nickel oxidized from 603K-743K (Rocaries 1971). Just as with iron, the curve is discontinuous at the Curie temperature. Likewise there is an increase in the activation energy corresponding to the transition from a ferromagnetic to paramagnetic.

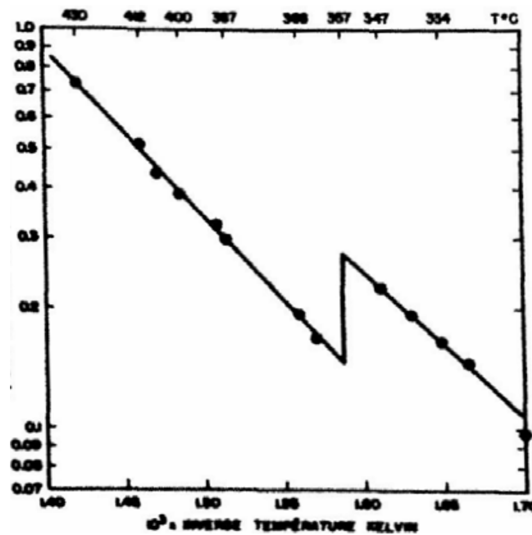

Figure 2.16: Effect of Curie temperature on the oxidation of pure nickel (Rocaries 1971).

The preceding three sections presented three pieces of evidence suggesting thin film oxidation is controlled at the metal oxide interface rather than within the oxide itself. It

was shown that for certain pure metals that experience a change in crystal structure there is a corresponding change in oxidation behavior. Likewise it was shown crystallographic orientation plays a role in oxidation. Several researchers have shown significant differences in oxide thickness and growth rate between polycrystalline metals and single crystals. Differences have also been found in oxidation behavior of single crystals of various crystallographic orientations. Lastly, the magnetic behavior, or more specifically the change in magnetic behavior was found to have an impact on oxidation of specific metals. Both iron and nickel showed changes in activation energy before and after the Curie temperature. This was a significant finding in that it related the importance of the electronic state of the metal at the metal-oxide interface to the oxidation behavior of the metal. Combined these findings show that for thin films, oxidation is controlled at the metal-oxide interface and are dependent on the electronic state of the metal.

2.2.5 Electron and Ionic Transport

Uhlig proposed that the slow escape of electrons from the metal surface is the controlling step in the formation of thin oxide films up to 10^5A thick (Uhlig 1956). This theory is vastly different from Motts postulation favoring the flow of metal ions from the metal to the oxide as the rate controlling step for thin films < 100A (Fehlner 1970). It also runs contrary to Wagner's parabolic theory where diffusion of ions through the oxide

lattice is thought to be the rate controlling step (Wagner 1933).

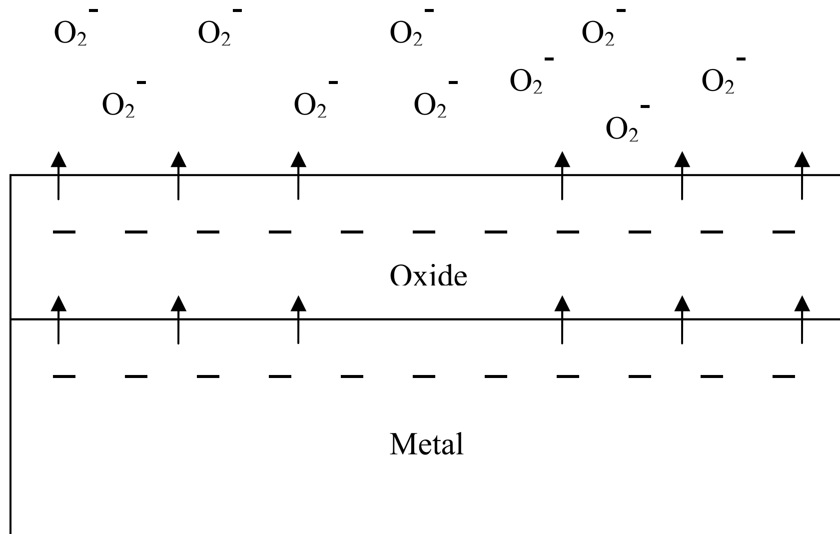

Figure 2.17: Schematic of electron flow from the metal to the oxide.

Central to Uhlig's theory is the idea of a space charge controlling the current of electrons and hence the oxidation behavior. Since the metal oxide has a greater electron affinity than the metal, electrons flow to the oxide creating a more negative space charge. These electrons then accumulate at lattice defect sites within the oxide which slows the flow of electrons (growth of the film) resulting in logarithmic reaction kinetics. Figure 2.17 shows a schematic of electron flow from the metal to the oxide. According to theory, electrons flow to the oxide because of the higher electro-negativity of the oxide, to compensate, an electron is emitted from the oxide into the surrounding atmosphere and enters an oxygen molecule. Then as shown in figure 2.17 the negatively charged oxygen atoms enter the oxide lattice.

2.2.6 Activation energy for Oxidation

The fundamental theorem to Uhlig's idea of logarithmic oxidation is electron flow from the metal to the oxide. This theory was first proposed by Rideal and Wansbrough-Jones in their investigation of the oxidation behavior of platinum and tungsten. Their experiments consisted of heating platinum filaments from 1700K-1900K at different oxygen partial pressures an in vacuum to determine the rate and mechanism of the reaction with oxygen to form PtO_2 (Rideal 1929). By chance, they happened to compare the experimentally measured activation energy for platinum with tungsten, previously measured by another group (Schottky 1928). Converted into eV, E_{Pt} = 2.74 eV and E_W=0.87 eV with their difference being $E_{Pt} - E_W$ = 1.87eV. They then compared the work functions of both materials (Φ_{Pt} = 6.35eV, Φ_W = 4.48eV) with the difference being $\Phi_{Pt} - \Phi_W$ = 1.87eV, the exact same value. Obviously this suggests a possible linear relation between activation energy and the metal's work function. Taking the idea one step further they decided to compare the activation energy and work function for several metals as shown in table 2.3. In each instance the difference $\Delta E - \Phi_{metal} \sim 3.6$eV, this happens to be very close to the electron affinity of the oxygen atom (3.4eV).

Table 2.3 Work function and activation energy of various metals (Uhlig 1956)

Element	**ΔE (eV)**	**Φ (eV)**	**Φ - ΔE (eV)**
Pt	2.74	6.35	3.61
W	0.87	4.48	3.61
C	0.52	4.31	3.79
Ni	0.9	4.5	3.6
Ta	0.55	4.12	3.57
Ti	0.56	3.95	3.39

After these realizations, Rideal and Wansbrough-Jones came up with an express for determining the activation energy for oxidation:

$$\mathrm{E} = \phi_{metal} - K \tag{2.25}$$

where:

$$K = \phi_a - \phi_\varepsilon \tag{2.26}$$

where ϕ_a is the energy of adsorption, ϕ_ε is the electron affinity of the adsorbed oxygen molecule, and ϕ_{metal} is the work function of the metal.

Physically, this phenomenon can be explained as the energy needed to transfer an electron from the metal to an oxygen molecule. If the work function of the metal is less than 3.6eV then there is no activation energy and the metal begins to oxidize immediately. On the other hand, as is the case for most metals, if the work function is greater than 3.6eV than the oxidation of the metal is delayed. Oxygen molecules begin to accumulate on the surface of the metal and are chemisorbed before being sublimated into the oxide lattice. It's important to note here that the molecules are chemisorbed at this point opposed to being physisorped, meaning a strong chemical bond is formed between the metal surface and oxygen opposed to weak van der waals bonds which form during the physisorption process.

The Rideal and Wansbrough-Jones activation energy is also in agreement with the previous evidence insisting control of oxidation at the metal-oxide interface. The argument was made for control at the metal-oxide interface because of convincing evidence directly relating oxidation rate to crystal structure, orientation and magnetic

properties. There is also convincing evidence relating a metal's work function to crystal structure, orientation and magnetic properties. Before citing evidence to this effect the physical meaning of work function should be defined. In their book, Henrich and Cox define a metal's work function as the energy needed to extract an electron from the Fermi level and put it at rest a sufficient distance away. A sufficient distance defined as far enough so the position of the electron does not influence the surface potential of the metal (10-1000A). There are many techniques used to measure a material's work function such as a Kelvin probe, and ultraviolet photoelectron spectroscopy (UPS) each having their advantages and drawbacks.

Evidence relating a metal's work function to its crystallographic orientation was first carried out in the early 20th century (Farnsworth 1940). Farnsworth et al. in particular measured the work function for several metals at several orientations. They showed a slight difference in the values for the work function of silver on (100) and (111) determined by the photoelectron and Kelvin null method (Farnsworth 1940). Figure 2.18 is a graph showing the change in photoelectron work function with time. In the experiment labeled B the work function of (111) was determined to be 4.75eV and (100) was 4.81eV. Previously for a similar experiment Farnsworth reported anisotropic behavior for the work function of copper with the difference between (100) and (111) being 0.46eV (Farnsworth 1940).

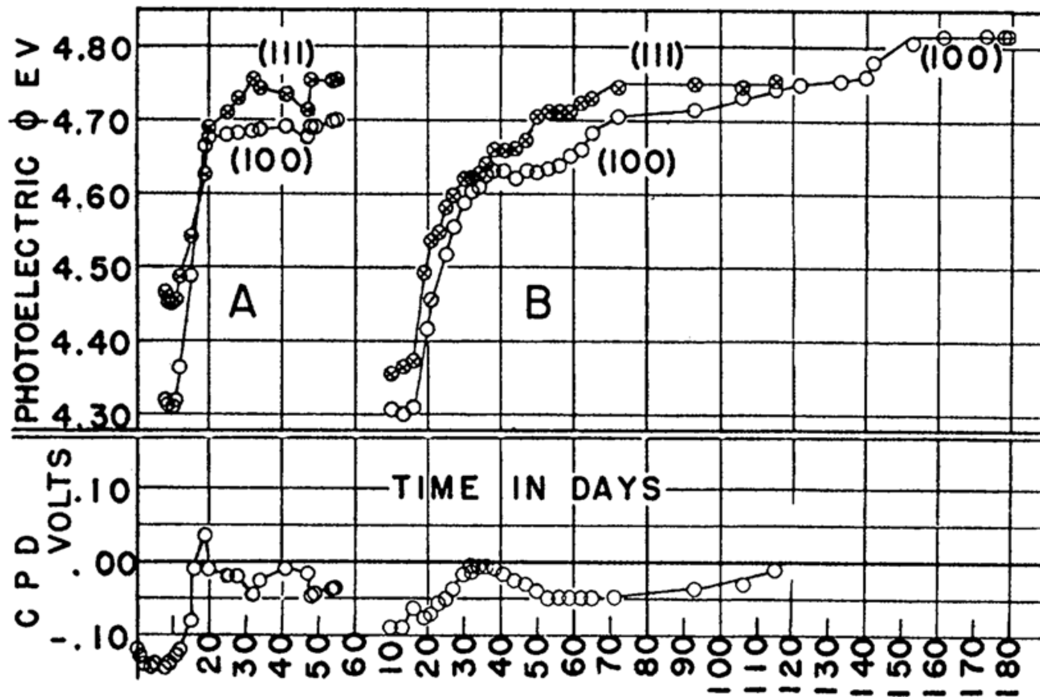

Figure 2.18: Graph showing the change in photoelectron work function with time for different silver crystal faces (Farnsworth 1940).

_Likewise the metal's work function was found to change with crystal structure. Experiments by Houdremont and Rudiger on iron showed a higher work function for austenite than for ferrite. This result is consistent with other studies which show higher activation energy after the transition to austenite (Houdremont 1952).

Finally Cardwell showed a difference in the work function before and after heat treatment above the Curie temperature. Figure 2.19 illustrates the effect of Curie temperature on the photoelectronic current for pure nickel. At 623K a sudden jump in photoelectronic current was observed which correlates to an increase in the work function after the Curie temperature (Cardwell 1949).

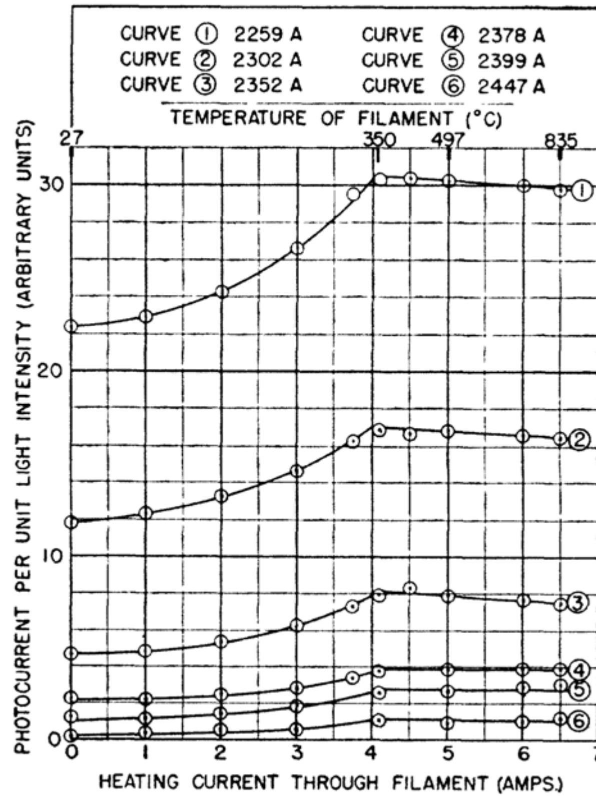

Figure 2.19: Effect of Curie temperature on the photoelectronic current for pure nickel (Cardwell 1949).

2.2.7 Derivation of Rideal and Wansbrough-Jones activation energy

Uhlig derived the Rideal and Wansbrough-Jones activation energy by simply relating the oxide growth rate to electron flow:

$$\frac{dy}{dt} = \mathrm{B}i \tag{2.27}$$

where $\frac{dy}{dt}$ is change in oxide thickness as a function of time , B is a constant, and i is the current between the metal and oxide. The current can be presented in the following form:

$$i = A'e^{\frac{-e(\phi - v')}{kT}} \tag{2.28}$$

where -e is the charge on the electron, φ is the work function of the metal, v' is the applied voltage across the metal-oxide interface, k is boltsmann's constant, T is temperature, and A' is a constant.

Then the rate of oxidation can be expressed as:

$$\frac{dy}{dt} = Ae^{\frac{-e\phi + ev - \frac{4\pi e^2 ly}{\varepsilon}}{kT}} \tag{2.29}$$

where l is the assumed oxide thickness, y is the total oxide thickness and ε is the dielectric constant of the oxide. Then taking the natural logarithm of each side of equation (2.29) gives:

$$\ln\frac{dy}{dt} = \frac{-e(\phi - \nu)}{kT} - \frac{4\pi ne^2 l}{\varepsilon kT} y + \ln A \tag{2.30}$$

Also from the logarithmic equation for oxidation:

$$y = k_0 \ln(\frac{t}{\tau} + 1) \tag{2.31}$$

Next taking the natural logarithm of each side of the derivative of (2.31) gives:

$$\ln\frac{dy}{dt} = \ln k_0 - \ln(t + \tau) \tag{2.32}$$

Next setting equation (2.31) equal to (2.32) and noting:

$$k_0 = \frac{\varepsilon kT}{4\pi ne^2 l} \tag{2.33}$$

Gives:

$$\ln k_0 = -\frac{-e(\phi - \nu)}{kT} + \ln\tau + \ln A \tag{2.34}$$

Now since the constant A is known to be temperature independent and the time constant τ has also been shown to be temperature independent or vary only slightly with temperature then it can be said:

$$\frac{d \ln \tau}{d(1/T)} \approx 0 \qquad (2.35)$$

Therefore equation (2.34) becomes:

$$\frac{d \ln k_0}{d(1/T)} = -\frac{-e(\phi - \nu)}{k} = \frac{-e(\Delta E)}{k} \qquad (2.36)$$

where k_0 is the intial oxide thickness after time τ, ϕ is the work function of the metal modified by contact with the oxide, ν is the positive electric potential within the oxide at the metal surface, and ΔE is the reaction activation energy. So an expression for the activation energy is given by:

$$\Delta E = (\phi - \nu) = \phi_0 - X_1 + [X_2 - (\phi_a + \phi_\varepsilon)] \qquad (2.37)$$

where ϕ_o is the metal work function, X_1 is the work function of the oxide at the metal-oxide interface, X_2 is the work function for the oxide at the oxygen-oxide interface, ϕ_a is the energy associated with the adsorption of oxygen on the metal oxide and ϕ_ε is the electron affinity of oxygen. Finally by saying the work function of the oxide at the metal-oxide interface is equal to the oxide work function at the oxygen-oxide interface the activation energy can be expressed as:

$$\Delta E = \phi_0 - (\phi_a + \phi_\varepsilon) = \phi_0 - K \qquad (2.38)$$

Equation (2.38) is the expression for activation of thin oxide films first presented by Rideal-Wansbourgh Jones in 1929. It should be noted that if the work function at the metal-oxide interface is larger than the work function at the oxide-oxygen interface then

K will be slightly larger than the expected 3.6eV. This was shown to be the case for both Cu (4.3eV) and Fe (4.4eV) (Uhlig 1956).

2.2.8 Space Charge Layer

When two materials of different electron affinities are placed in contact with one another an electric field develops. In the case of two metals with only slight differences in electronic affinity, the electric field only extends tens of angstroms. When a metal is in contact with a semiconductor, as is the case with a metal in contact with an oxide, this electric field can be extended up to several thousands of angstroms (Uhlig 1956). This is because unlike with metals where many electrons are excited into the conduction band, semiconductors have relatively few electrons in the conduction band rather they accumulate at lattice defect sites, so in this sense the space charge extends over a larger volume than in metals (Uhlig 1956).

Now assuming the metal-oxide interface is the rate controlling interface as was discussed earlier, and assuming the flow of metal ions and electrons is the controlling step in oxidation, then the rate of escape of metal ions and electron control the surface charge on the metal and the resulting space charge between the metal and oxide. First looking at the kinetics of metal ion escape which has been shown to follow:

$$\frac{d\alpha}{dt} = K' e^{-W/kT} \tag{2.39}$$

where $d\alpha/dt$ is the rate of metal ion escape, K' is a constant, W is the energy necessary to transfer ions from the metal to the oxide, k is Boltzmann's constant, and T is temperature. Similarly, the rate escape of electrons from the metal to the oxide can be expressed by:

$$\frac{d\beta}{dt} = K'' e^{-e\phi / kT} \tag{2.40}$$

where $d\beta/dt$ is the rate of electron escape, K'' is a constant, -e is the charge on the electron, and ϕ is the modified work function of the metal in contact with the oxide.

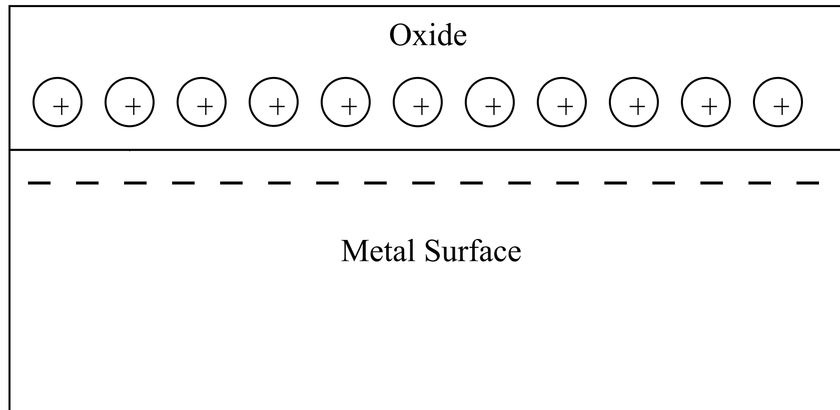

Figure 2.20: Schematic of positive space charge upon initial oxidation.

Due to the fact that electron flow is thought to be the slower process and therefore the rate controlling process it can be reasonably assumed ϕ is greater than W. So, upon initial oxidation there is a positive space charge as seen in figure 2.20 above. This is due to the rapid escape of metal ion at the onset of oxidation. However after some oxide growth, the rate of escape of both metal ions and electrons are controlled by the slower electron release rate. Additionally, as oxidation continues, electrons become trapped at lattice defect sites, which turns the space charge less positive. In some cases the electrons accumulate to the point where the space charge becomes negative as can be seen in figure 2.21 (Uhlig 1956).

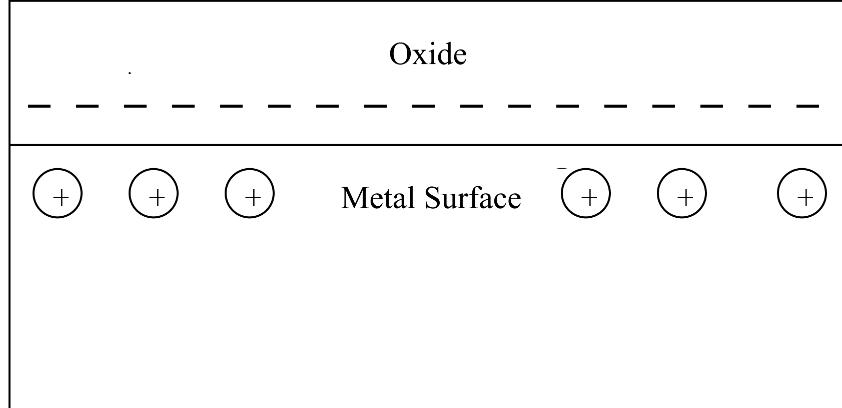

Figure 2.21: Schematic of changing space charge due to the accumulation of electron at lattice defect sites.

The evolution of the space charge layer as a function of oxide thickness is an important factor in the kinetics of thin oxide films. As electrons accumulate at lattice defect sites and the space charge layer becomes more negative or less positive, the flow of electrons from the metal to the oxide slows down (Uhlig 1956). Since the release rate of electrons from the metal is the rate controlling mechanism, this in turn means the oxide growth rate itself begins to decrease. This idea of changing space charge is the fundamental reasoning behind logarithmic growth kinetics.

2.2.9 Derivation of Logarithmic Kinetic Equation

To this point it has already been shown that for thin oxide films, rate control is established at the metal-oxide interface. Furthermore, evidence of electron flow as the rate controlling step was presented from the dependence of activation energy on the metal's work function. This section will relate potential at the metal-oxide interface to the changing space charge layer and therefore to logarithmic oxidation kinetics.

In his famous derivation of the logarithmic oxidation kinetics equation, Uhlig started with two basic assumptions. First, the excess charge in the thin oxide film was assumed to be uniform, corresponding to a uniform defect density throughout the film. Second, it was assumed the space charge layer breaks down at a certain oxide thickness. Remembering a positive space charge develops because of the initial rapid escape of positive metal ions, at some point excess electrons in the oxide layer create a equal an opposite positive charge on the metal side of the interface which cancels out the established positive space charge. At this point the space charge no longer influences the rate of escaping electrons and the logarithmic rate law gives way to linear or cubic oxidation kinetics. Given these assumptions, Uhlig first used Poisson's relation to define the potential at the metal oxide interface:

$$\frac{d^2V}{dy^2} = \frac{4\pi ne}{\varepsilon} \tag{2.41}$$

where V is the potential at the metal-oxide interface, y is the total thickness of the oxide film, n is the density of electrons trapped at lattice defect sites, e is electron charge, and ε is the dielectric constant of the oxide film. Taking the integral of equation (2.41):

$$\frac{dV}{dy} = \frac{4\pi ne}{\varepsilon} y_1 + C_1 \tag{2.42}$$

Now from Uhlig's second assumption it can be said:

$$\frac{dV}{dy} = 0 \tag{2.43}$$

when the total thickness of the film equals L, the oxide thickness at which the space charge layer breaks down. Then, solving for C_1 in equation 2.42 gives:

$$C_1 = \frac{4\pi neL}{\varepsilon}$$

so

$$\frac{dV}{dy} = \frac{4\pi ne}{\varepsilon} y_1 + \frac{4\pi neL}{\varepsilon} \tag{2.44}$$

Now obtaining the surface potential from the integral of equation (2.44):

$$V = \frac{-4\pi ne}{\varepsilon}(Ly_1 - \frac{y^2}{2}) + C_2 \tag{2.45}$$

where C_2 is a constant of integration.

Taking the potential at the metal surface to be:

$$V_0 = -(\phi - v) \tag{2.46}$$

where ϕ is the work function of the metal, and v is the resulting potential difference of the oxide-oxygen interface, and the metal oxide interface. It was shown earlier in the Rideal and Wansbrough-Jones activation energy derivation that v can be approximated by the electron affinity of the oxygen atom. Subsequently, it follows that:

$$C_2 = V_0 = -(\phi - v) \tag{2.47}$$

and for thin oxide films where $L >> y$ the y^2 term can be neglected, therefore equation (2.45) becomes:

$$V = \frac{-4\pi ne}{\varepsilon} Ly_1 - (\phi - v) \tag{2.48}$$

Oxidation kinetics is proportional to the rate of escaping metal ions so it follows:

$$i = C\frac{dy}{dt} = A' e^{\frac{-e(\phi - v')}{kT}} \tag{2.49}$$

where A' and C are a constants ϕ is the modified metal work function, i is current from the metal to the oxide, and v' voltage across the metal oxide interface. It is important to note that equation 2.49 only considers current following from the metal to the oxide. Reverse current from the oxide to the metal can be neglected in this case because of the strong initial positive space charge. Now substituting equation (2.48) into equation (2.49):

$$\frac{dy}{dt} = Ae^{\frac{-e(\phi - v) - \frac{4\pi e^2 ly}{\varepsilon}}{kT}} \tag{2.50}$$

According to equation (2.50) the voltage applied across the metal-oxide region decreases as the oxide thickness increases. Now integrating equation (2.50) with the initial conditions:

$$t = 0;$$
$$y = 0$$

gives

$$y = \frac{\varepsilon kT}{4\pi ne^2 L} \ln\left[\left(\frac{4\pi ne^2 LA}{\varepsilon kT} e^{\frac{-e(\phi - v)}{kT}}\right) t + 1\right] \tag{2.51}$$

Expression (2.51) can be further simplified into the familiar form:

$$y = k_0 \ln\left(\frac{t}{\tau} + 1\right) \tag{2.52}$$

where $$k_0 = \frac{\varepsilon kT}{4\pi ne^2 L}$$

and $$\tau = \frac{\varepsilon kT}{4\pi ne^2 LA} e^{\frac{-e(\phi - v)}{kT}} = \frac{k_0}{A} e^{\frac{-e(\phi - v)}{kT}}$$

Physically τ can be interpreted as the time constant indicating the time needed to oxidize to a thickness k_0. Thus far data showing the temperature dependence of τ has been inconclusive (Uhlig 1956).

2.3 Nanoindentation

As its name implies, nanoindentation is an indentation test able to obtain material properties from sub-micron depths. Like other hardness tests, nanoindentation involves the penetration of the sample with an indenter, however, in nanoindentation a new depth sensing parameter is introduced, the contact depth (h_c) (Oliver 1992). The contact depth in conjunction with tip area function allow for the estimation of the contact area without imaging. This technique allows for the gathering of mechanical data at sub-micron depths. In addition to measuring hardness, depth sensing capabilities also allows for the measurement of elastic modulus, storage and loss modulus, continuous stiffness measurements as a function of depth, and several creep parameters.

Nanoindentation also offers many practical benefits over more traditional mechanical testing methods. The most obvious of these is the ability to obtain mechanical properties from a very small volume of material. This holds for applications were tensile testing is impractical such as the testing of very thin films or grains on an individual solder ball.

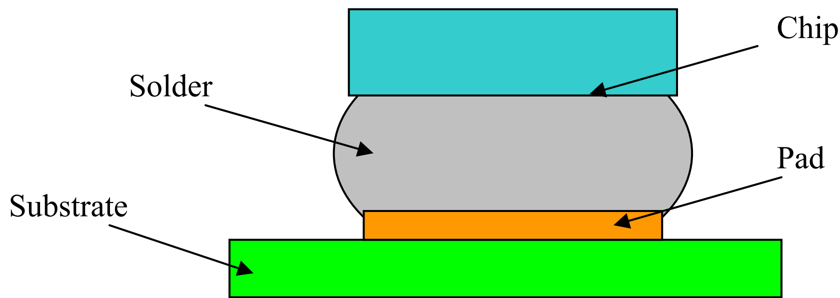

Figure 2.22: Schematic of a typical solder joint.

Testing of assembled parts is also possible with nanoindentation. For example, figure 2.22 shows one solder ball of a flip chip assembly. With nanoindentation, one could test the mechanical properties of the solder ball, IMC, pad, substrate and chip. This is highly desirable since mechanical properties can change after the reflow process.

Another practical benefit of nanoindentation is the cost of testing. It has already been mentioned, only a very small volume of material is needed for mechanical testing with nanoindentation. This dramatically reduces the costs of testing as compared to traditional tensile tests. A tensile test would require a minimum of three dog-bones at several different strain rates. This would require much more material, and material processing costs. The cost difference is significant for the testing of a material such as indium, which runs anywhere from $990-$1040 per kilogram.

It must be mentioned, however, that nanoindetation has certain limitations compared to other mechanical testing methods. Uniaxial tensile tests for instance, measure many more mechanical properties than a single nanoindentation test, most notably the plastic properties of a material. Apart from elastic modulus, a single tensile

test can also measure the yield stress, ultimate tensile stress, strain hardening exponent, total elongation, etc.

2.3.1 Mechanics of Nanoindentation

Defined as, the depth to which the sample is in contact with the indenter, the contact depth is measured by extending the slope of the upper portion of the unloading curve to the x-intercept as shown in the figure 2.23 below.

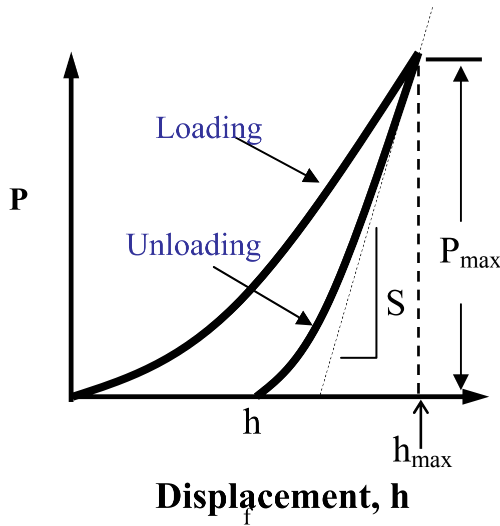

Figure 2.23: Load (P) vs. displacement (h) plot for a typical nanoindentation loading and unloading cycle.

Algebraically, the contact depth can be expressed as:

$$h_c = h_{\max} - \varepsilon \frac{P_{\max}}{S} \qquad (2.53)$$

where h_{max} is the maximum depth of the indentation, P_{max} is the maximum load of the indentation, S is the measured contact stiffness, and ε is a constant related to the shape of the indenter tip (Doerner 1986).

The contact depth can then be used in conjunction with an area function to determine the projected contact area. Each indentor tip (berkovich, conical, pyramid, etc.) has a specific area function which estimates the projected contact area based on the contact depth. For example the projected contacted area for a Berkovich tip takes the form:

$$A = 24.5{h_c}^2 + C_1 h_c + C_2 {h_c}^{1/2} + C_3 {h_c}^{1/4} + C_4 {h_c}^{1/8} + C_5 {h_c}^{1/16} \qquad (2.54)$$

where the first constant is 24.5, and C1-C6 are tip specific constants determined from the tip area calibration. From the area function and the resulting projection of the contact area, both hardness and reduce modulus can be calculated.

Calculation of the hardness is fairly straight forward. As defined in equation (2.55) the hardness is simply the maximum load divided by the projected contact area.

$$H = \frac{P_{\max}}{A} \qquad (2.55)$$

Calculation of the reduced modulus, on the other hand, is a bit more complex. In their groundbreaking nanoindentation study, Oliver and Pharr define reduced modulus as:

$$E_r = \frac{\sqrt{\pi}}{2\beta}\frac{S}{\sqrt{A}} \qquad (2.56)$$

where Er is the reduced modulus, S is the contact stiffness, and A is the projected contact area, and β is a constant dependent on tip geometery. Contact stiffness defined as:

$$S = \frac{dP}{dh} \qquad (2.57)$$

is measured from the initial slope of the unloading curve shown in figure (2.24) (Doerner 1986). Depending on the elasticity of the material being indented, the percentage of the unloading curved used in contact stiffness calculations could have a significant impact on

the reduced modulus. Therefore most researchers only use the upper 25%-90% of the unloading curve. The reduced modulus calculated from equation 2.56 is not the true elastic modulus of a material because it includes elastic deformations from the material as well as the indenter. To determine the true elastic modulus, elastic strains from the indenter must be subtracted from the reduced modulus by:

$$\frac{1}{E_r} = \frac{1-\upsilon^2}{E} + \frac{1-\upsilon_i^2}{E_i} \tag{2.58}$$

where E_i is the elastic modulus of the indenter tip, ν_i is Poisson's ratio for the indenter tip, and E and ν are the elastic modulus and Poisson's ration for the material being indented (Oliver 1992).

2.3.2 Dynamic Nanoindentation

Quasi-static nanoindentation has certain limitations in the characterization of materials that exhibit time dependent plasticity (Li 2002). For such applications, a continuous stiffness indentation method was developed to remove the effect of creep on the measured contact stiffness (Li 2002). Dynamic nanoindentation superimposes a sinusoidal load on top of a quasi-static load to obtain contact stiffness measurements continuously as a function of displacement. Figure 2.24 shows the typical loading curve for a dynamic nanoindentation test. From the contact stiffness, elastic modulus and hardness can be calculated as a function of depth.

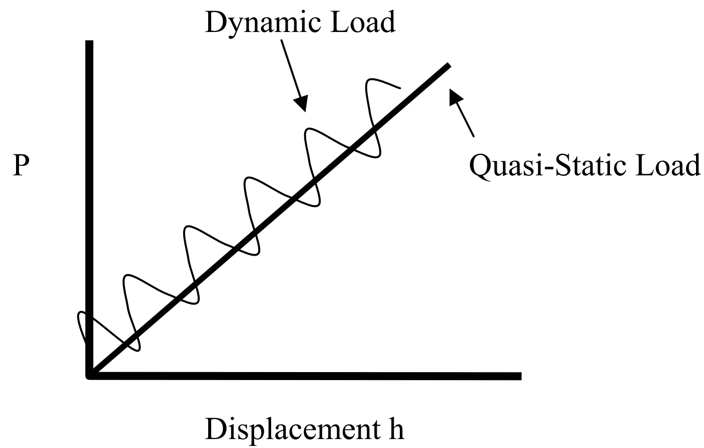

Figure 2.24 Load (P) vs. displacement (h) plot for a dynamic nanoindentation test. The dynamic load is superimposed on the quasi-static load to measure the contact stiffness as a function of depth.

2.3.3 Nanoindentation Creep

In addition to measuring elastic modulus and hardness, nanoindentation has also been used to characterize the creep behavior of materials. Nanoindentation creep offers several advantages over traditional constant load uniaxial creep tests. Uniaxial creep tests often require anywhere from several hours to several months to complete, whereas nanoindentation creep tests are often completed within a couple of minutes. Also as was mentioned in the previous section, much less material is need, so tests can be completed at a fraction of the cost.

2.3.4 Creep Mechanics

The rate-controlling mechanism and overall creep behavior of a material is dependent on several material and environmental parameters. A material's crystal structure, grain size, and microstructural constituents all determine how it reacts under constant load. When comparing materials of similar composition, factors like precipitate strengthening and grain size become of greater importance. The morphology, crystal structure, and dispersion of second phase precipitates in the matrix all influence the creep behavior of a material. Likewise, when grain boundary diffusion is significant, grain size becomes an important factor in the overall creep behavior (Dieter 1986).

In addition to material variables, environment also influences the creep response. As was stated earlier, creep becomes significant as the ambient temperature approaches 0.5Tm. This is because creep is a thermally activated process driven by diffusion. As the diffusion of vacancies increase at higher temperatures, so do the mobility of dislocations throughout the lattice. Creep is also highly dependent on the level of stress. The level of stress determines whether the rate-controlling mechanism is dislocation climb, glide, or grain boundary sliding (Dieter 1986).

For most crystalline materials, a power law relation is used to quantify the time-dependent plastic response:

$$\dot{\varepsilon} = b\sigma^n \exp\left(\frac{-Q}{RT}\right) \tag{2.59}$$

where $\dot{\varepsilon}$ is the strain rate, b is a stress coefficient, n is the strain hardening exponent, Q ia the activation energy, R is the gas constant, and T is the absolute temperature in Kelvin (Dieter 1986). The stress exponent, activation energy, and stress coefficient can all be

measured via nanoindentation techniques to determine the creep mechanism. Several studies have shown good agreement between nanoindentation and traditional constant load tensile tests, for measured values of stress exponent and activation energy. However because of the different stress states (multiaxial for nanoindentation and uniaxial for tensile) a new definition of strain rate must be defined.

For uniaxial tensile test strain rate is defined as:

$$\dot{\varepsilon} = \frac{\varepsilon_2 - \varepsilon_1}{t_2 - t_1} = \frac{d\varepsilon}{dt} \tag{2.60}$$

where ε is strain and t is time (Lucas 1999). Since strain isn't explicitly measured in a nanoindentation test, indentation stain rate is defined as:

$$\dot{\varepsilon} = \frac{1}{h}\left(\frac{dh}{dt}\right) \tag{2.61}$$

where h is defined as the current plastic depth, and $\dot{\varepsilon}$ is the indentation strain rate. To determine the stress exponent of the power-law equation, the indentation strain rate is plotted verses indentation contact stress, similar to strain rate verse stress in uniaxial testing (Lucas 1999). The slope of the curve on a log-log scale gives the stress exponent. A preliminary estimation of the controlling mechanism is based on the value of the stress exponent. When the stress exponent is 1, creep is said to be controlled exclusively by dislocation climb. Higher stress exponents from 3-8 are thought to be a mix of dislocation climb and dislocation glide. Finally at relatively higher stresses, when the stress exponent is greater than 8, the power-law relationship breaks down and creep is solely controlled by dislocation glide.

Chapter 3 – Experimental Procedure

3.1 - Sample Preparation

Sample surface preparation is a very important step in oxidation experiments. Surface roughness, purity, and microstructure all impact the oxidation behavior of the material. For repeatable oxide thickness measurements, it is necessary to create a sample with an ultra smooth surface condition. Samples with a rough surface will have greater oxidation because of increased surface area.

3.1.1 – Electro-Chemical Polishing

Creation of a smooth surface finish for indium initially proved to be quite difficult. Traditional mechanical polishing of indium produces a poor surface finish because of indium's very low hardness at room temperature. Mechanical polishing attempts were unsuccessful. Polishing starting with 600 grit silicon carbide and was incremented to diamond slurry, and finally 20nm silica slurry. Silicon carbide, diamond, and silica particles all embedded on indium's surface. This obviously would impact the oxidation behavior, kinetics, mechanical response, etc.

To solve this problem we adopted an electrochemical polishing (ECP) approach. To implement this approach we built an electrochemical polisher (figure 3.1) which consisted of a rectifier, anode, cathode, and a beaker for the electrolyte solution. The electrolyte solution was a 3:1 ethanol to nitric acid bath which had to be maintained at 0˚C because the solution becomes unstable at room temperature.

ECP has many benefits over traditional mechanical polishing. First, ECP only takes a fraction of the time of mechanical polishing. To mechanically polish indium to a scratch free surface takes well over an hour because of the many steps involved, whereas ECP only takes 2-5 minutes. Second, ECP produces a much smoother finish compared to mechanical polishing because material is removed from the peaks at a much faster rate than the valleys. Third, ECP is a stress free polishing technique. Unlike mechanical polishing where residual stresses develop on the surface, ECP does no mechanical work on the surface. Finally, ECP produces a hygienically clean debris free surface finish. As mentioned earlier, particles embedded in the sample surface when mechanically polishing, making repeatable oxidation experiments nearly impossible.

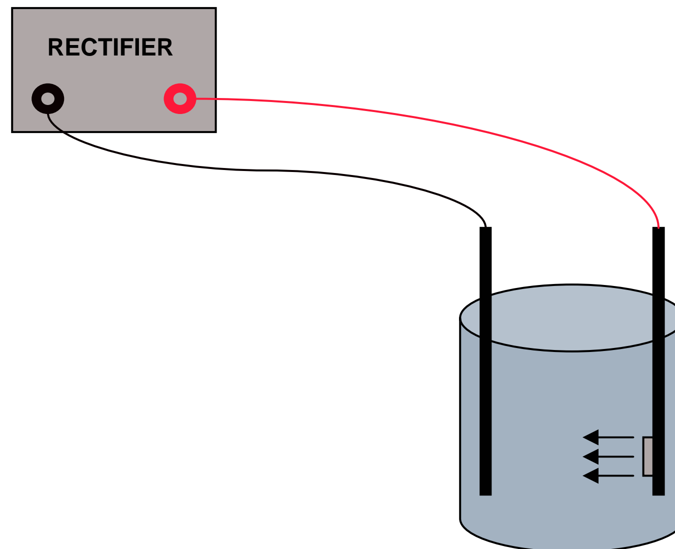

Figure 3.1 Schematic of electrochemical polisher.

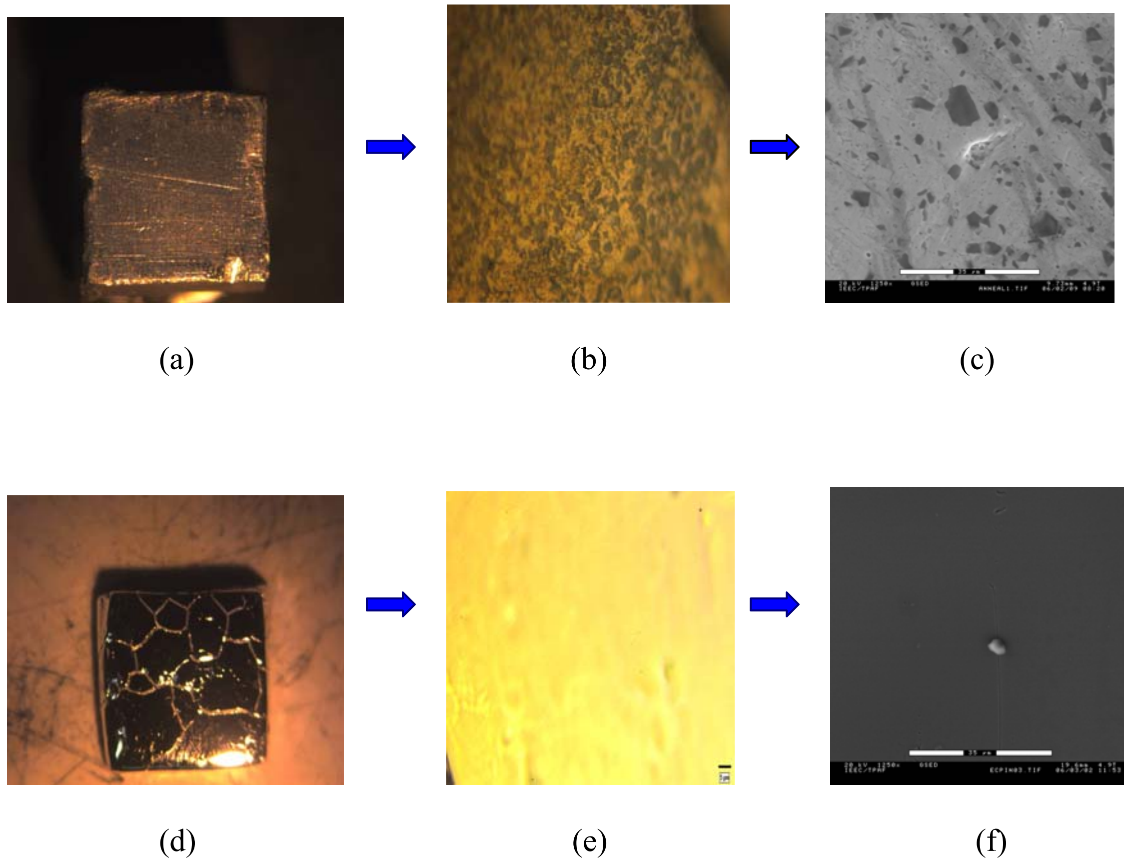

Figure 3.2 Optical and SEM images of indium mechanically polished (a) (b) (c) , and electrochemically polished (d) (e) (f).

The images shown above in figure 3.2 show a side by side comparison of indium mechanically polished and electrochemically polished. As we can see in images (a), (b), and (c) mechanical polishing produces a poor surface finish. Silicon carbide particles cover the sample surface, making repeatable thickness measurements near impossible. However in images (d), (e), (f) we see an ultra smooth surface finish where grain boundaries are exposed. Images e and f show a nearly featureless indium surface which is highly desirable for oxidation and nanoindentation experiments.

3.2 – Oxidation Experiments

Oxidation experiments were carried out using 99.999% indium foil obtained from Goodfellow UK, cut by razorblade into 50mm x 5mm strips. These strips were then electrochemically polished in a 3:1 ethanol to nitric acid solution for 2-5 minutes at approximately 4 volts. Mechanical polishing was avoided because SiC/slurry particles embed in indium's surface. Immediately after polishing, the samples were rinsed in distilled water for 2 minutes and then dried and stored in a nitrogen environment. Before oxidation the samples were cut into 5mm x 5mm squares.

3.2.1 – Oxidation of Indium in Air

Oxidation was carried out by placing the samples on a glass slide on a hot plate. The temperature of the solder was monitored by a K-type thermocouple placed on the glass slide, about 1mm from the sample. With a temperature reading of 160˚C on the thermocouple, the indium sample melted, which is in agreement with published data where T_m = 157˚C. Figure 3.3 and 3.4 shows the hot plate setup for oxidation experiments performed in air and the thermocouple/digital logger used to monitor and record temperature respectively.

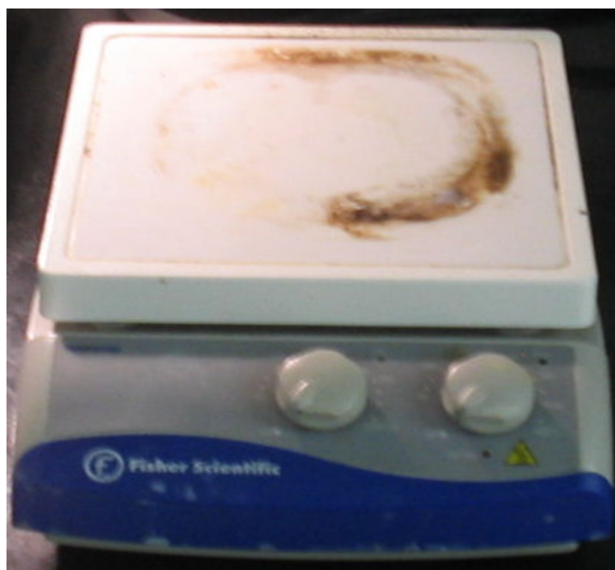

Figure 3.3 Image of hot plate

Figure 3.4 Image of Type K thermocouple and digital logger.

For oxidation experiments, the hot plate was first heated to the desired temperature, then the indium sample was placed approximately 1mm from the thermocouple. The thermocouple was attached to the glass slide using high temperature (260˚C rating)

Kapton adhesive tape. After two hours the slide was removed from the hot plate using tweezers, and cooled in air. For oxidation kinetics experiments the same procedure was followed. Samples were heat treated at 145˚C, 180˚C, and 220˚C between 1 and 120 minutes. Again after the allotted time the glass slide was removed from the hot plate and the samples were allowed to cool in air. After all oxidation experiments the samples were stored in a nitrogen environment.

3.2.2 – Oxidation of Indium under Controlled Environment

For the inert and reducing environment experiments, the hotplate was placed in a glove box (MBraun USA, 14 Marin Way, Stratham, NH) capable of reducing oxygen and moisture contents to < 0.1ppm and controlling hydrogen content to within 0.1%. Figure X is a picture of the glove box located in room F6 if the engineering building.

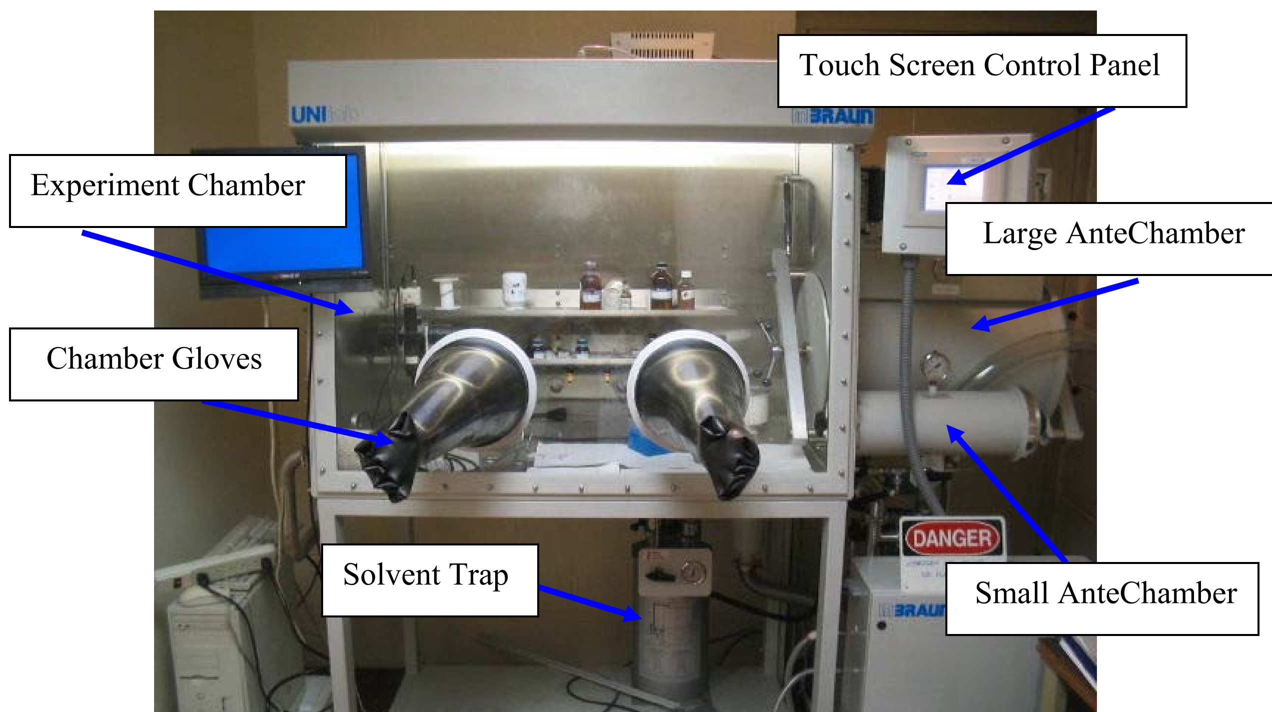

Figure 3.5 Image of glove box used for atmospheric control in oxidation/reduction experiments.

Special procedures must be followed when importing equipment/materials into the glove box chamber. Large items such as the hot plate were transferred using the large antechamber while smaller items such as glass slides and tweezers were transferred using the small antechamber. To import items into the experiment chamber, the items must first be placed in the antechamber. Next the anti-chamber is placed under vacuum, and then filled with box air. This step is repeated three times, however for the final step the vacuum is held for 30 minutes with the small chamber and several hours with the large chamber. After the out gassing procedure is completed, the antechamber is filled with box air and the chamber door inside the experiment chamber is opened to transfer the contents to the experiment chamber.

Control of the glove box atmosphere is accomplished using special gas purifiers. First the chamber was purged with high purity 99.999% nitrogen obtained from Airgas,

Binghamton New York. The gas purifiers use Molecular Sieve with a Cu catalyst to remove excess O_2, and H_2O from nitrogen gas. The concentration of oxygen, water vapor, and hydrogen were monitored by highly accurate sensors. The moisture analyzer is capable of detecting moisture from 0.1ppm to 350ppm in 0.2ppm increments. The oxygen analyzer is capable of detecting oxygen gas between 0.1ppm and 1000ppm in .3ppm increments. Figure 3.6 is a picture of the control panel touch screen showing the current concentration of water vapor and oxygen in the glove box environment. Additionally the glove box was equipped with a hydrogen analyzer to detect the concentration of hydrogen in the glove box atmosphere for the reducing environment experiments. However there is no hydrogen purification included with the system. Control of the hydrogen environment was accomplished by purging and filling.

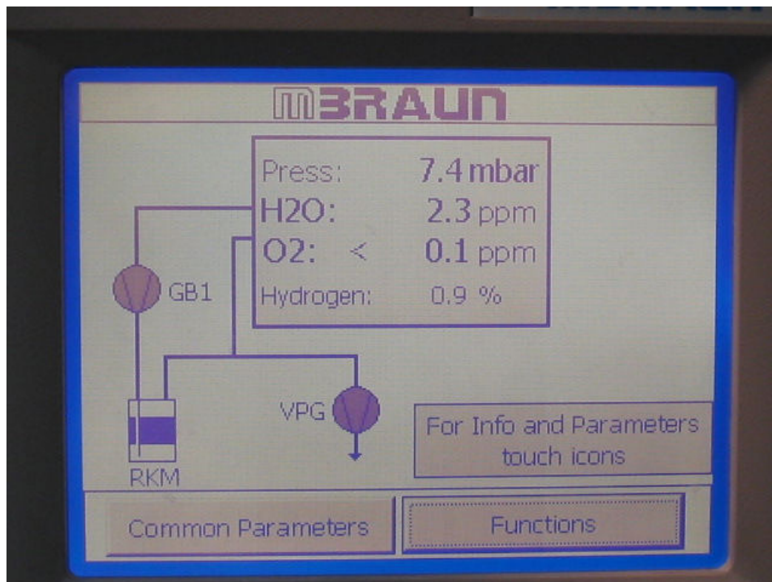

Figure 3.6 Digital touch display control panel for glove box.

The procedure for the oxidation experiments performed in the glove box is very similar to the procedure for oxidation experiments performed in air. For the “inert” environment

experiment, once the oxygen and moisture were both less than 0.1ppm the hot plate setup seen in figure 3.3 was heated to the appropriate temperature and the indium samples were heat treated for two hours. The glass slide was then removed from the hot plate and cooled in nitrogen.

For the reducing environment experiments, hydrogen gas was added to the atmosphere until the combination of temperature and hydrogen concentration created a thermodynamically defined reducing environment. Samples for reduction experiments were previously oxidized in air following the procedure outline in section 3.2.1, then heat treated at the reduction conditions. After several hours the samples were removed from the hot plate and allowed to cool in the glove box environment. Because of the proximity of the glove box atmosphere to thermodynamic equilibrium, oxidation upon cooling was assumed to be negligible.

3.3. –Thickness measurements

3.3.1 – Ellipsometry

After the samples were thermally oxidized thickness measurements were carried out using NanoFilm's EP3 Spectroscopic Ellipsometer shown in figure 3.7. Ellipsometry is an especially useful technique because of its nondestructive nature with little or no special preparation needed other than a smooth sample surface.

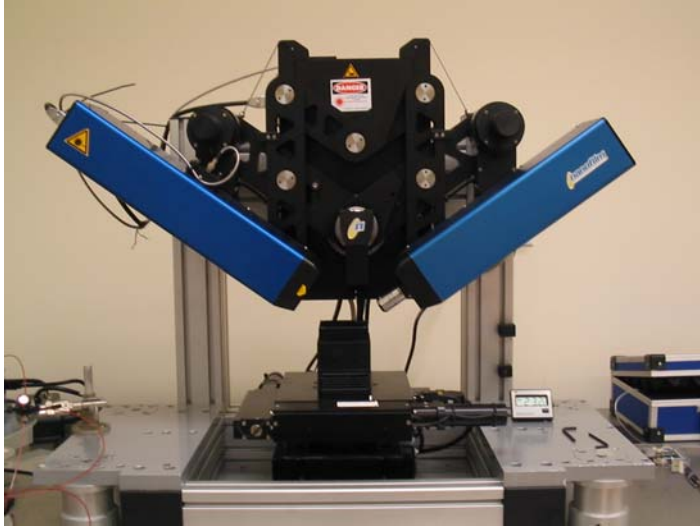

Figure 3.7 Image of NanoFilm's EP3 Spectroscopic Ellipsometer.

As demonstrated in the figure 3.8 below, an ellipsometer measures the thickness of thin films by reflecting known polarized light onto the sample. This polarized light reflects off both the thin film and the thin film-substrate interface resulting in a different polarization of the light. This change in polarization is analyzed in terms of s and p light which can be converted to the familiar ellipsometry variables Ψ and Δ via the following equation:

$$\frac{R_P}{R_S} = \tan\psi e^{i\Delta} \tag{3.1}$$

where Rp is the reflected p-light, and Rs is the reflected s-light.

A sample plot of Δ verses wavelength is shown in figure 3.9. In the plot Δ measured via ellipsometry is compared to Δ calculated theoretically from the index of refraction and extinction coefficient for indium-indium oxide system. The mean square error from figure 3.9 is then plotted verses film thickness to derive the film thickness.

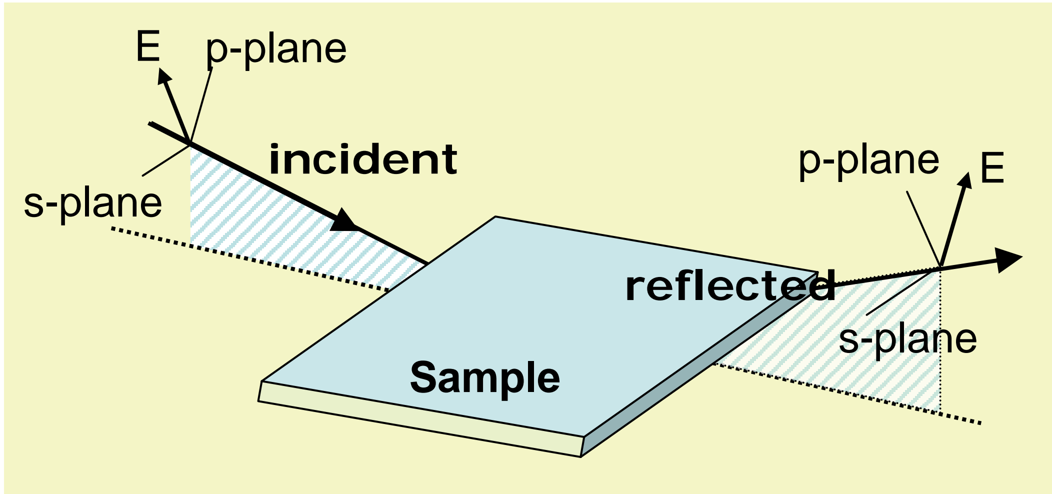

Figure 3.8 Illustration of principles of ellipsometery.

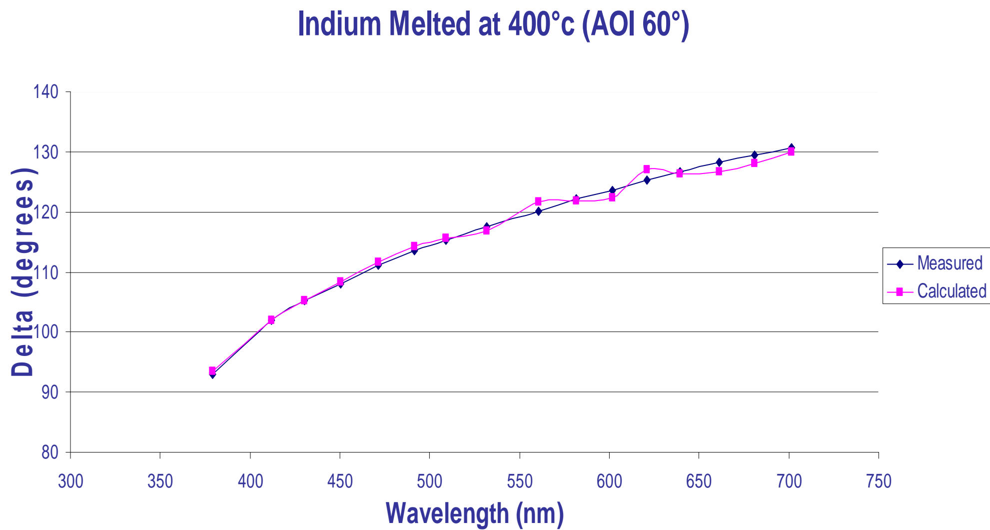

Figure 3.9 Plot of calculated delta verses measured delta for indium melted at 400C.

3.4 – Microstructural Characterization

As mentioned earlier, a smooth, debris-free sample surface is needed to accurately determine the oxidation behavior, conduct thickness measurements, and to measure the mechanical response through nanoindentation. After mechanical and electro-chemical polishing, indium's surface was investigated by several microscopic techniques.

3.4.1 – Optical Microscopy

Both optical and stereo microscopy where used for initial characterization of indium's surface. A Nikon optical microscope capable of magnifications from 50X-1000X and a stereo microscope 7X-40X are shown in figure 3.10. Because of the large grains of pure indium the stereo microscope was used to estimate the grain size.

Figure 3.10 Image of Nikon optical microscope.

3.4.2 – Scanning Electron Microscopy

To ensure indium's surface was free of particles which could influence oxidation behavior, high resolution microscopy was employed. Scanning Electron Microscopy (SEM) was used because it offers much higher magnification than optical techniques. The SEM is located in the geology department of Binghamton University and was operated by Debbie Dittrich.

3.4.3 – AFM

Before indentation, a high resolution image of the specimen surface was taken by atomic force microscope (AFM). AFM creates a topographical image of a surface by dragging a tip across the surface and recording changes in z-height.

3.5 – X-Ray Diffraction

X-Ray Diffraction (XRD) is a characterization technique that can be used to identify materials and their crystal structure. Samples are bombarded by x-rays of known wavelength at different angles. X-rays then diffract off the sample surface and either constructively or destructively interferes with one another to create a diffraction pattern. Constructive interference results in an intensity peak, while destructive interference results in no peak. Materials can then be identified by the angle of peak intensities and the magnitude of the peak at these angles. Once a diffraction pattern is measured the data was compared with a database of unknown materials to identify indium and indium oxide.

3.6 – Mechanical testing using Nanoindentation

Nanoindentation was used to characterize the mechanical properties of both indium and indium oxide. This particular technique was chosen because of ease of implementation, and to avoid the high material costs associated with tensile specimen preparation. All experiments were performed on the Triboindenter nanoindentation system manufactured by Hysitron in Minneapolis, Minnesota. Figure 3.11 is a picture of the system used located in room A5 of the engineering building.

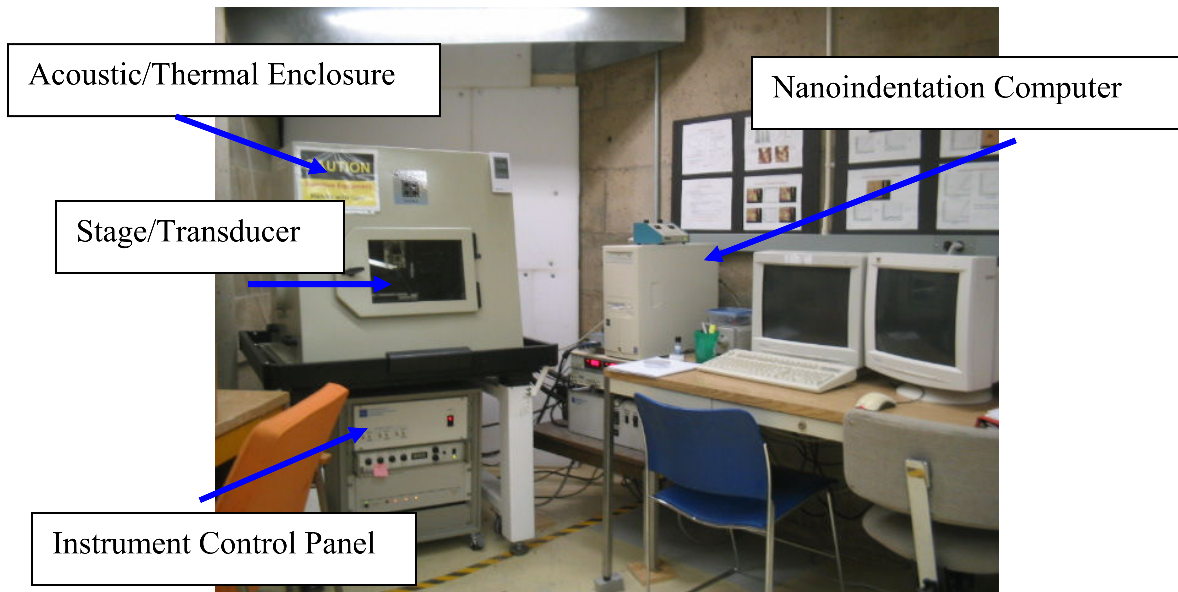

Figure 3.11 Image of Hysitron nanoindentation system.

The large unit to the left in figure 3.11 is the indentation apparatus. It consists of a stage, transducer, indenter tip, optical microscope, all housed under an acoustic/thermal enclosure. The lower half of the Triboindenter is the instrument control panel and associated electronics. Figure 3.12 is an image of the nanoindenter stage located under the enclosure. A maximum of nine samples can be place on the nanoindenter stage. Care

must be taken to place the tallest specimens to the right to avoid tip crashing after indentation.

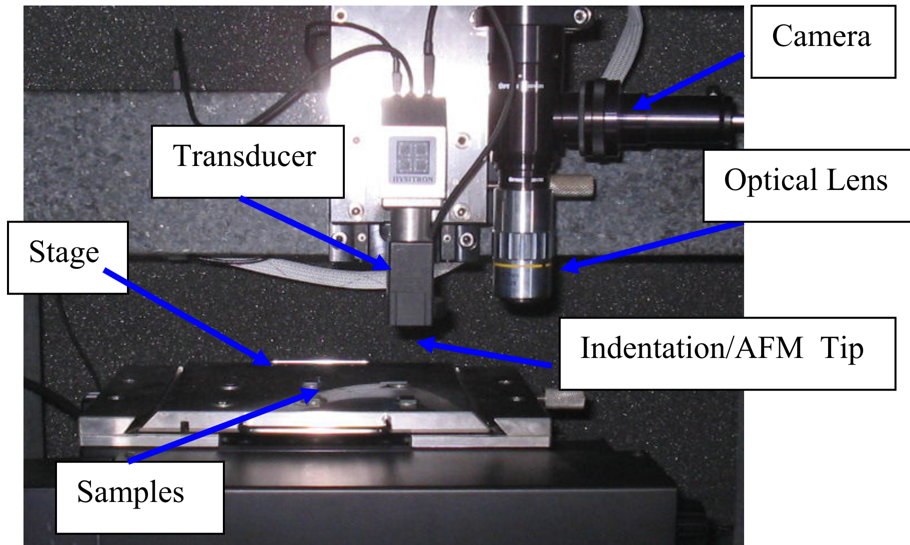

Figure 3.12 Image of the nanoindenter stage and transducer located under the enclosure.

To indent a sample, the sample must first be glued to a small magnetic AFM speciemen plate, the plate is then held on the stage by magnetic force. The optical lens shown in figure 3.12 is used to locate the samples on the stage. After selection and installation of an appropriate indenter tip, the optics must be calibrated to determine the X,Y,Z distance between the lens and the tip, this is accomplished through an H-indent calibration.

3.6.1 – H-Indent Calibration

The H-indent calibration makes a series of indents on an aluminum single crystal in the pattern of an H. Then the operator locates the position of the indents under optics

so it can be correlated back to the position of the tip. Without an H-indent calibration it is impossible to locate which area on the sample surface is being indented.

3.6.2 – Air-Indent Calibration

Displacements and forces applied to the indenter tip are measured via a two plate capacitive transducer. For the transducer to accurately measure these quantities the transducer constants must be calibrated. Both the spacing between capacitor plates and the electro-static force are calibrated during the air calibration.

3.6.3 – Tip Area Calibration

As mentioned earlier, unlike conventional hardness tests that measure the area of the indentation mark, nanoindentation uses the contact depth in conjunction with a tip area function to estimate the projected contact area. The tip area function, unique to each tip, is determined by making a series of indents at various loads on fused silica. The area for each of these indents can be determined from the reduced modulus of fused silica and the contact stiffness calculated from the slope of the unloading curve. Then the calculated area for each indent is plotted verses the contact depth. Finally this curve is fitted to constants C1-C5 in equation 2.54 to determine the area as a function of contact depth. An example plot of the contact area as a function of contact depth for a berkovich tip is shown in figure 3.13.

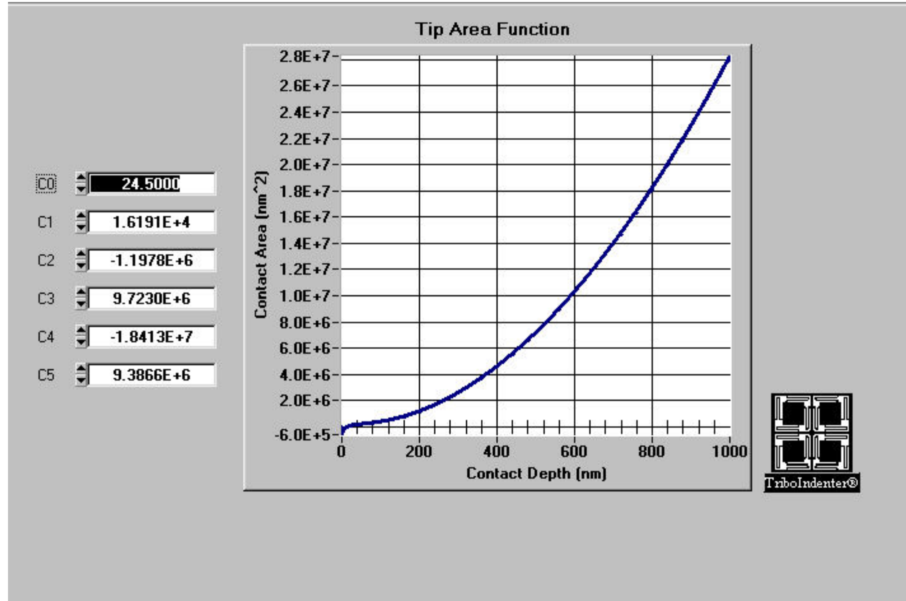

Figure 3.13 Measured heating stage berkovich tip area function.

3.6.4 – Machine Compliance Calibration

In addition to the above calibrations, the load frame compliance must be calculated to determine the elastic deformation of the indenter during testing. During an indentation experiment both the specimen being indented and the load frame experience elastic strains. These small elastic strains experienced by the load frame are particularly significant because of the small scale of the indents being performed. The parameter that quantifies load frame compliances is called machine compliance. Mathematically, the total compliance can be expressed as:

$$C_{Total} = C_m + C_c = C_m + \frac{\sqrt{\pi}}{2}\frac{1}{\sqrt{A}}\frac{1}{E_r} \tag{3.2}$$

where C_m is the compliance of the load frame, C_c is the compliance of the specimen, and C_{Total} is the total compliance. Rearranging equation 3.2 the machine compliance can be expressed as :

$$C_m = C_{Total} - \frac{\sqrt{\pi}}{2}\frac{1}{\sqrt{A}}\frac{1}{E_r} \tag{3.3}$$

The procedure for determining the machine compliance is similar to that of determining the area function. A series of indents are performed on fused silica with relatively large loads. Then the compliance (inverse of contact stiffness) is plotted verses $1/A^{1/2}$ to determine the machine compliance at the y-intercept.

3.6.5 – Quasi-Static Testing

Quasi-static testing is a single indentation where the specimen is loaded then unloaded. It is the unloading curve under quasi-static testing that is used for data analysis. The contact stiffness is determined from the slope of the upper portion of the unloading curve. The contact depth is calculated by extending the slope of the unloading curve to the x-intercept. Both the elastic modulus and hardness can be calculated from unloading curve during quasi-static testing. Figure 3.14 shows the loading profile used to determine the elastic modulus of indium. For this test indium was loaded to 2000μN at a rate of 200 μN/sec. Next during segment 2 of the loading curve the load is held for 5 second to alleviate transient creep effects which may introduce error into calculation of the contact stiffness. Creep effects will be discussed in more detail later. Finally, the specimen is unloaded at a very fast rate 2000 μN/sec to obtain the unloading response with minimal influence of creep.

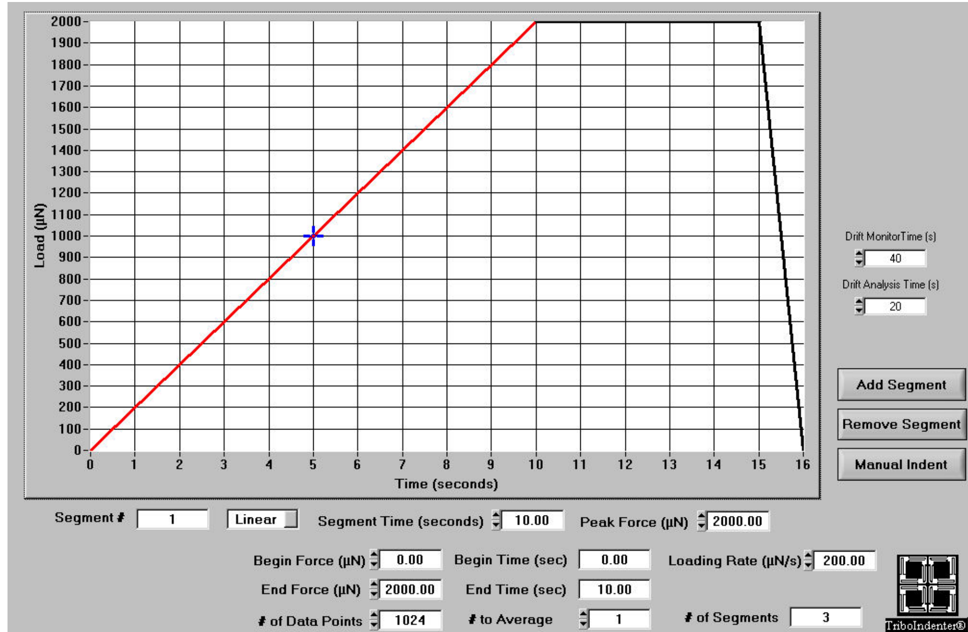

Figure 3.14 Quasi-static loading profile to determine elastic modulus and hardness of indium.

3.6.7 – Heating and Cooling Stage

In order to test the mechanical properties of indium as a function of temperature, a heating and cooling stage built by Hysitron was installed in place of the existing specimen stage. As seen in figure 3.15 the heating and cooling stage assembly consists of a heating and cooling stage incased in ceramic and a transducer heat-shield. The transducer shield protects the transducer heat generated by the heating stage.

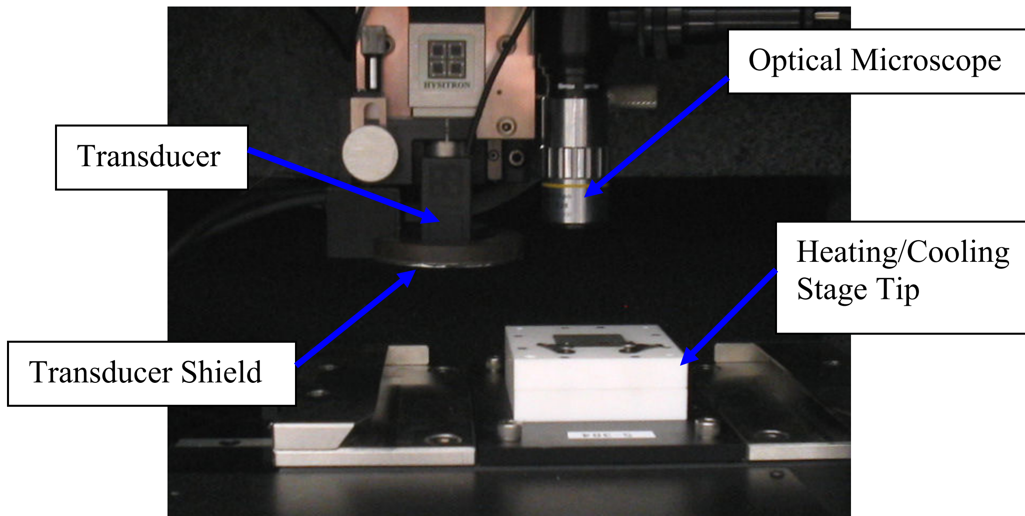

Figure 3.15 Hysitron's heating and cooling stage assembly.

The temperature of the heat/cooling stage is controlled by Tribo TC software. A screen shot of the controlling software is shown in figure 3.16.

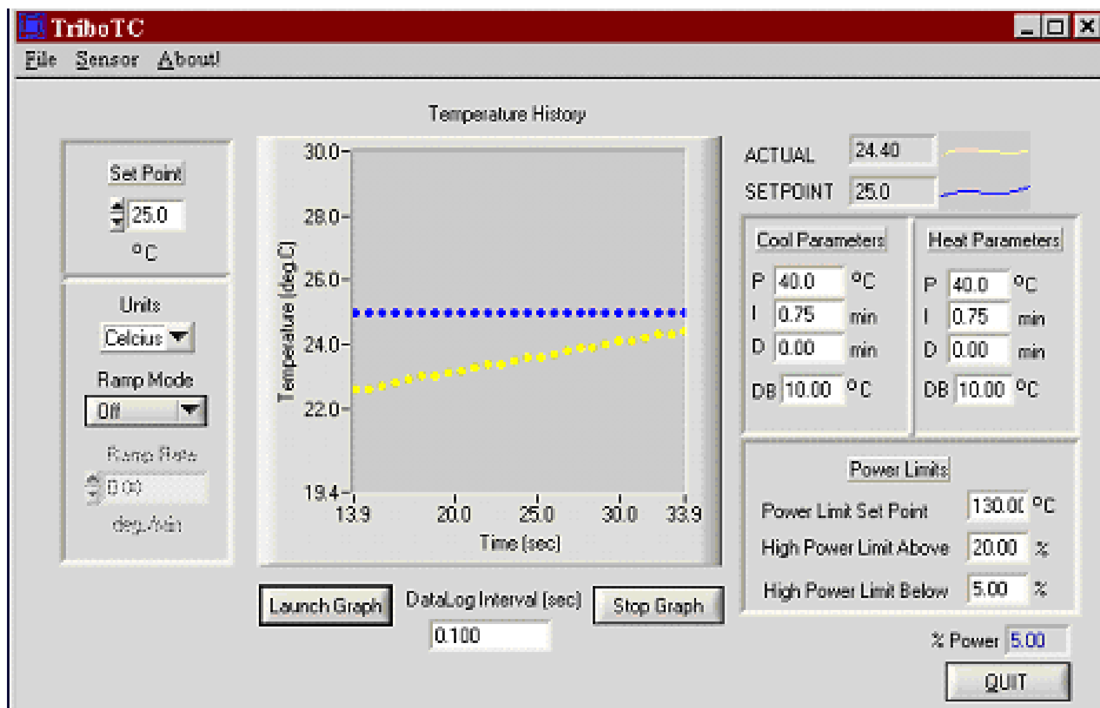

Figure 3.16 Screen shot of TriboTC control panel.

Before performing indentation experiments, the sample was glued to a specimen holder to raise the sample to the appropriate height. An image of indium on the sample holder is shown in figure 3.17.

Figure 3.17 Aluminum sample holder used for heating and cooling stage.

The sample holder was then mounted to the heating stage via two spring clips. The sample was then heated to the appropriate temperature and monitored for one hour by a Type K thermocouple attached to the sample surface with polyimide adhesive. After reaching steady state temperature the transducer was switched into AFM scan mode directly over the sample to allow the transducer to stabilize before testing. It's important to note an air calibration was performed at each temperature to account for thermal drift.

3.6.8 – Creep Testing

Even though nanoindentation creep is a fairly new technique, it offers advantages over standard creep testing in that testing requires significantly less material and tests are

completed in a fraction of the time. Creep tests were preformed in quasi-static mode under constant indentation load. An example creep test loading curve is show in figure 3.18. The sample was first loaded at 500μN/sec to a maximum load of 5000μN. To measure the creep response of the material, the load is held at 5000μN for 180sec then unloaded.

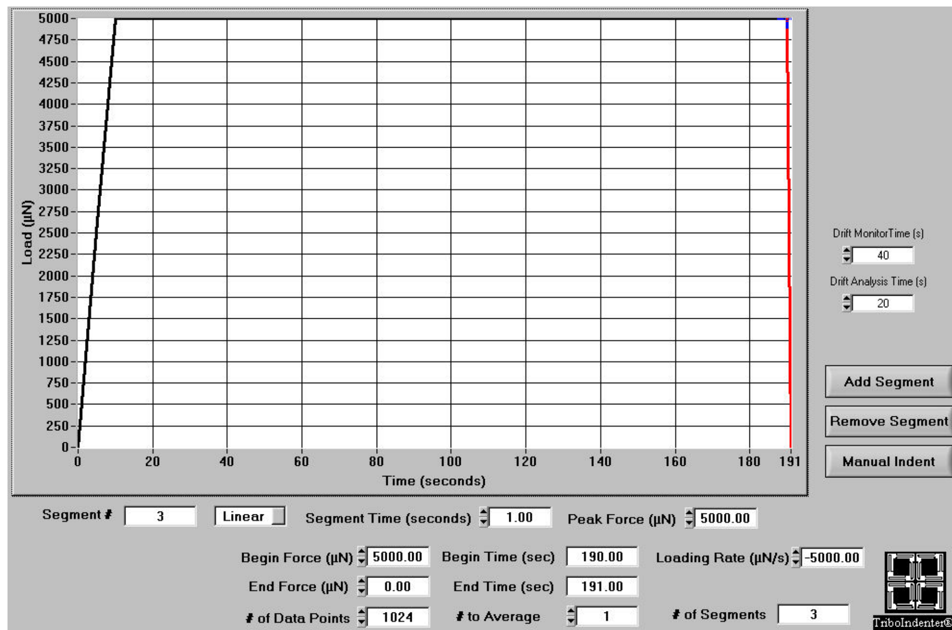

Figure 3.18 Quasi-static loading profile for constant load creep test.

Chapter 4 – Results and Discussion

4.1 Oxidation of Indium

Several studies have shown the detrimental effect of metal oxides on the reliability of solder joints. The direct measurement of joint strength by shear lap joint testing showed joint strength to decrease with increasing oxide thickness. Likewise, wetting angle measurements of indium on Ti/Au pad have shown the wetting angle to increase with increasing oxide thickness, implicitly suggesting poor joint strength with increasing oxide thickness. Each of these findings warrants a complete study of the oxidation behavior of pure indium solder. This includes a thorough thermodynamic assessment of the oxidation and reduction zones as a function of temperature, oxygen partial pressure, moisture content, and hydrogen content. Additionally, the kinetics of oxide growth should be studied as it relates directly to the development of a reflow profile. Lastly, the removal of oxide scales should be studied in the event oxidation cannot be avoided during processing.

There are very few studies on the oxidation behavior of indium in air at or around the reflow temperature. Eldridge et al. in their paper "Analysis of Ultra-thin Oxide Growth on Indium" studied the oxidation of indium at room temperature utilizing ellipsometry for thickness measurements. They found the growth of In_2O_3 on thin indium films to be self-limiting to about 50A. They fit the growth kinetics to an inverse logarithmic rate law developed by Cabrera and Mott (Fehlner 1970).

Another study by Jenco et al. entitled "AES studies of surface phenomena on liquid

indium solder" studied the oxidation and reduction behavior of polycrystalline and liquid indium solders. Using a microbalance for thickness measurements, they showed the growth kinetics to follow a logarithmic relationship at 145˚C, 180˚C, and 220˚C, although they did not classify it as such. Additionally, they found the maximum oxide thickness at each temperature to plateau at 3.5nm at very low oxygen partial pressures. Considering the lack of data concerning the oxidation of indium, a more complete examination is necessary.

4.1.1 Oxidation of Indium in Air

For the reasons outlined in the previous section, the oxidation behavior of pure indium solder in air was studied. First, to get a baseline for the oxidation of indium in air, indium was heat treated at several temperatures above and below its melting point for 120 min. This time (120 min) was chosen because initial experiments showed little increase in oxide thickness beyond this point. With the hot plate pre-heated to the designated temperature, electro-chemically polished indium squares were placed on a glass slide atop the hot plate. Figure 4.1 shows the resulting oxide thicknesses as a function of temperature for indium samples heat treated for 120min.

Several important points can be made from this plot. First, there is little or no oxidation before the melting point (157°C). Meaning, during processing, indium can be stored at elevated temperatures (below T_m) without significant oxidation. For example if there's another solder on the package or if an underfill needs to be cured, as long as the respective reflow and curing temperature does not exceed 157°C, indium should not experience significant oxidation. However, at and above T_m there is a significant

increase in oxide layer growth. As seen in figure 4.1, when the temperature is increased from the last data point before the melting temperature 145°C, to 220°C, the oxide thickness increases from approximately 4nm to 22nm. This finding is of importance since oxide layers in this thickness range have been found to affect the reliability of the solder joint.

Finally, after the rapid oxidation around indium's melting temperature, the oxidation behavior again showed relatively constant behavior. Increasing the heat treatment temperature from 220°C to 300°C showed no increase in oxide thickness on indium solder. This also is significant from the packaging processing point of view in the selection of a reflow temperature. Considering only the affect of oxidation on final joint strength, there is no significant difference in oxide thickness if we choose a reflow temperature between 200°C and 300°C. They all show similar oxidation behavior.

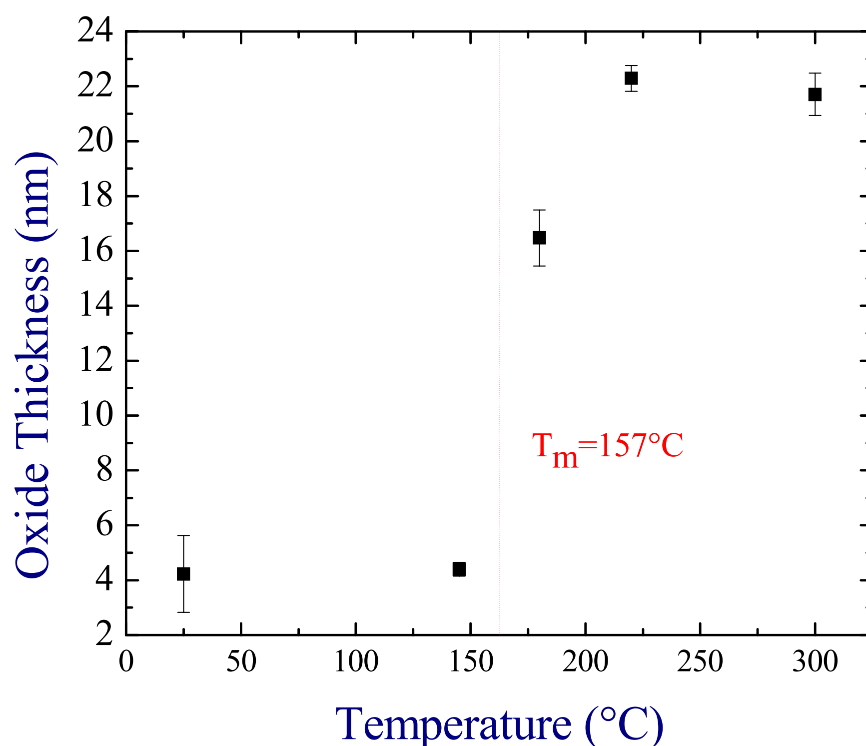

Figure 4.1: Indium oxide thickness as a function of temperature heat treated for 120min in air.

4.1.2 Oxidation of Indium in a Controlled Environment

From the thermodynamic calculations presented earlier, it was shown oxidation depends heavily on the constituents of the atmosphere in which it is processed. Oxygen, moisture, and hydrogen content in conjunction with temperature determine the stability of the reaction. For precise control of the reaction environment, samples were heat treated in a specially designed glove box which monitors hydrogen partial pressure. Both oxygen and moisture are filtered by the glove box leaving only temperature and hydrogen content as variables. The glove box environment consisted of ultra-high purity nitrogen gas

(99.999%), >0.1ppm oxygen, 0.3ppm moisture, and 0.6% hydrogen. For comparison against the baseline test established in the previous section, each sample was heat treated at the same temperatures as in the air environment. Figure 4.2 shows the resulting oxidation thickness versus temperature plot for samples heat treated in the glove box environment. Again, just as with the samples oxidized in the air environment, very little change in oxidation thickness is detected below indium's melting point. From 25°C to 145°C, the oxidation thickness stays relatively constant 4-5nm. However at indium's melting point there is a subtle increase in thickness followed by a decrease at 180°C. The trend seems to follow the thermodynamic prediction for this environment. Based on the concentrations of oxygen, moisture, and hydrogen in the glove box environment, indium is oxidizing in the temperature range from 25°C-160°C. However after 160°C, the reaction reaches equilibrium and crosses into the reduction zone. Because the reaction is so close to equilibrium it is assumed the reaction kinetics is very slow, therefore any significant disassociation of In_2O_3 is unlikely. However as the temperature is increased further (i.e. after crossing further into the reduction zone) the oxide thickness seems to be decreasing.

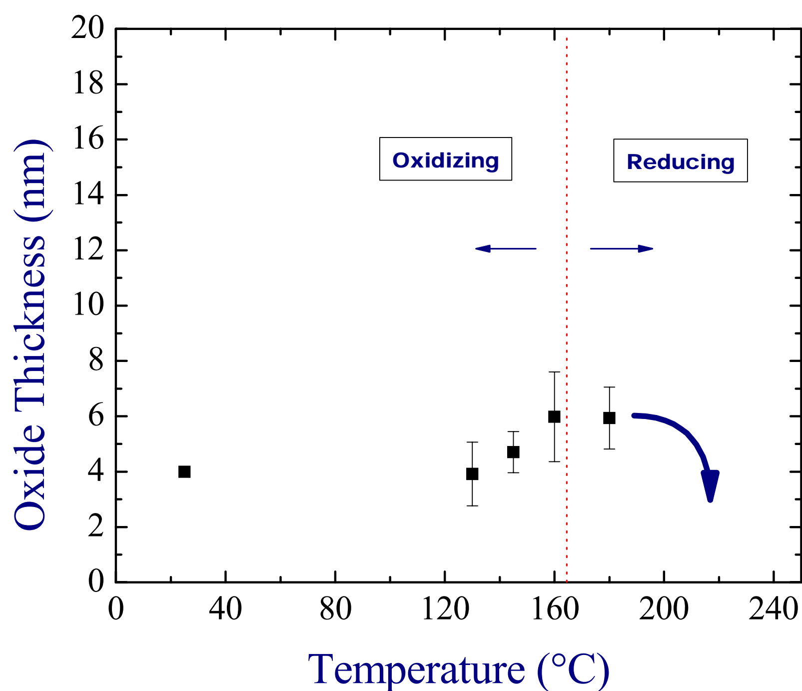

Figure 4.2: Indium oxide thickness as a function of temperature heat treated for 120min in a glove box environment with pH_2O = 0.3ppm, pO_2 <0.1ppm, and H_2 = 0.6%.

Unfortunately at this point in the experiment the shape of liquid indium changed from a rectangular shape into a sphere making oxide thickness measurements very difficult. Figure 4.3 is a series of images showing the evolution of indium's shape as a function of temperature when heat treated in air. Below the melting temperature at 130°C and 145°C little change in the sample surface can be seen. At and above the melting temperature, indium's surface becomes rough because of phase change, and a yellow scale develops. Throughout the various heat treatments in air indium always maintains its rectangular shape.

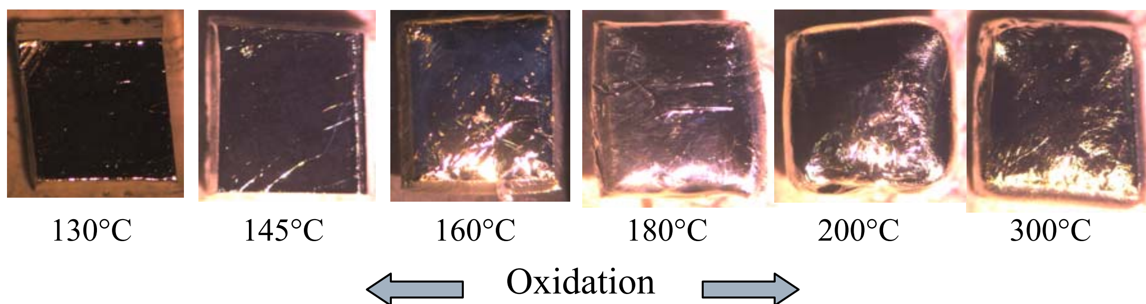

Figure 4.3: Evolution of indium shape as a function of temperature in air.

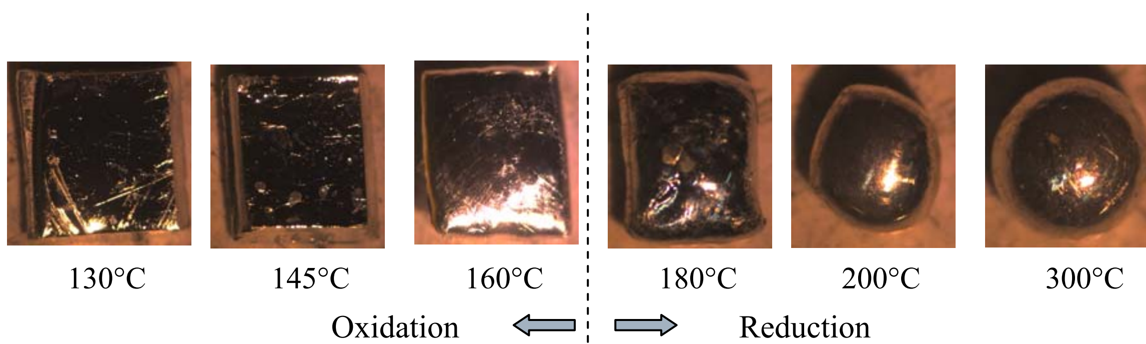

Figure 4.4: Evolution of indium shape as a function of temperature in glove box with pH2O = 0.3ppm, pO2 <0.1ppm, and H2 = 0.6%.

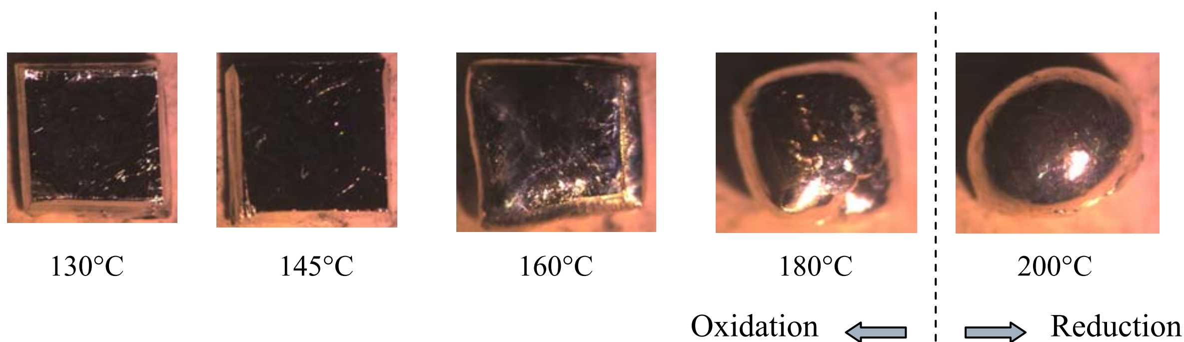

Figure 4.5: Evolution of indium shape as a function of temperature in glove box with pH2O = 5.5ppm, pO2 <0.1ppm, and H2 = 0.6%.

However, as seen in figure 4.4, indium's shape changes from rectangular to spherical when the reaction changes from oxidizing to reducing. Again below indium's melting point little change is seen on the sample surface. After melting, at 160°C, the glove box sample looks similar to the air sample because at this point the reaction is still in the oxidation zone. According to thermodynamic calculations at the glove box atmospheric conditions, the reaction should cross over into the reduction zone at approximately 160°C. It is at this point that indium starts to turn spherical as seen in figure 4.4. Increasing the temperature further to 200°C - 300°C turns the sample into a complete sphere. The indium sample changes shape to achieve a lower surface energy at higher temperatures, however when heat treated in air a thick oxide scale develops which prevents indium from obtaining a spherical shape. Therefore it can be assumed, qualitatively, that spherically shaped samples were not oxidized and possibly reduced.
With these assumptions, results from heat treatments preformed in the glove box environment (figure 4.2) coincide with thermodynamic predictions. For a more direct comparison, the results from the oxidation experiments were superimposed on a thermodynamic map of the oxidation and reduction zones. Figure 4.6 shows a thermodynamic map as a function temperature and hydrogen content at 0.3ppm, and pH2O/pH2 ratio. Samples heat treated in the oxidation zone (left-hand side of the map) oxidized readily. As the reaction approached equilibrium, (indicated by the line) samples experienced only slight oxidation as compared to samples heat treated in the air environment. This condition is illustrated by the green data points on the map.

Finally, inside the reduction zone (indicated on the right-hand side of map) samples showed no sign of oxidation. Again as discussed earlier, thickness

measurements were not possible because of the spherical shape of these samples, therefore reduction could not be confirmed. However it is assumed the spherical shape indicates no oxidation at these conditions.

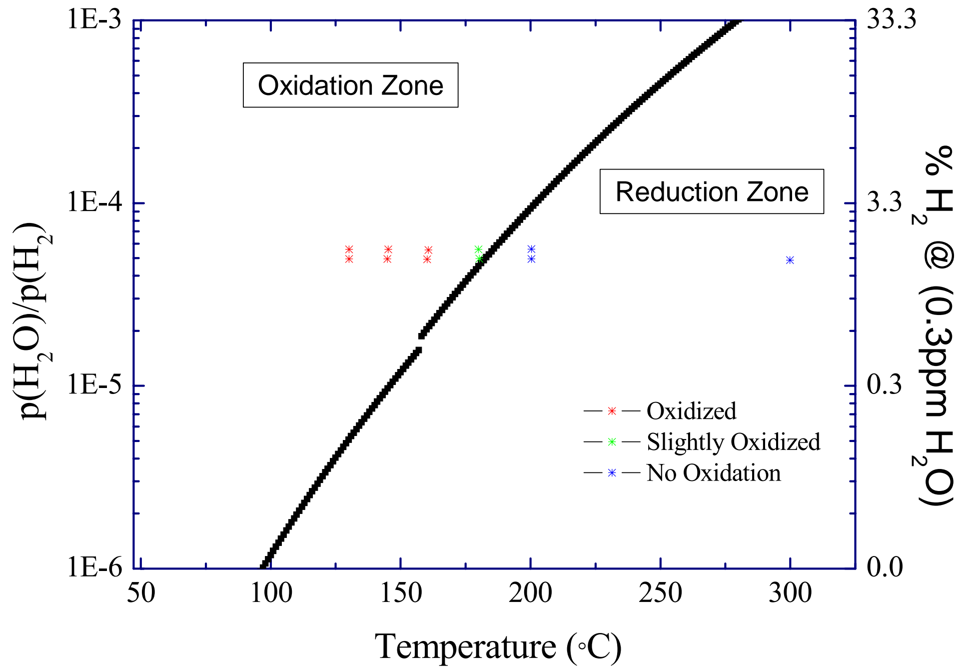

Figure 4.6: Thermodynamic map of oxidation and reduction zones with heat treatment results superimposed.

4.2 Oxidation Kinetics

Complementing the thermodynamic verification oxidation study, indium's oxidation growth kinetics was investigated in both air and inert environments. Information on oxidation kinetics is useful when developing a reflow profile or processing procedure. By knowing the rate at which indium oxidizes at a specific

temperature, processing can be engineered in such a way to avoid environments where thick oxides develop.

4.2.1 Oxidation Kinetics in Air

Oxidation kinetics of indium in air was measured at three temperatures 145˚C, 180˚C, and 220°C. These temperatures were chosen to compare growth rates before (145˚C) and after melting (180˚C), and at a possible reflow temperature (220˚C). As with previous experiments, samples were prepared and heat treated from 5 to 120 minutes. After the allotted time, samples were immediately removed from the hot plate and cooled in air. Between 3-5 thickness measurements were made for each sample.

Figure 4.7 shows the oxide growth kinetics for indium at 145˚C. After 5 minutes an oxide thickness of 2nm was measured, which increases to over 4nm after 120min. This result is in agreement with previous results showing very little oxidation before the melting temperature. After curve fitting the results to several different rate laws, logarithmic kinetics gave the best fit with a correlation coefficient greater than 0.9. Fitting to Uhlig's logarithmic rate law gave a time constant of 0.52 min for an initial oxide thickness of 0.8nm. From these results the initial oxidation rate was determined to be 1.5nm/min.

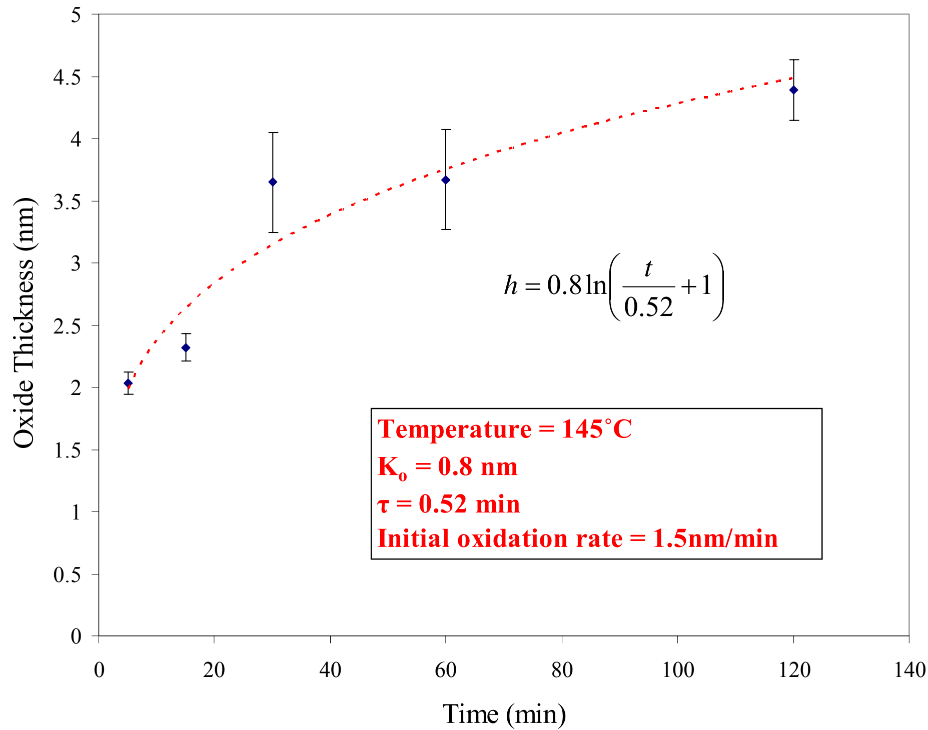

Figure 4.7: Growth kinetics of indium in air at 145˚C.

Likewise, the kinetics was measured after melting at 180˚C. Figure 4.8 shows the resulting kinetics curve. The growth rate at 180˚C also followed a logarithmic function with a correlation coefficient greater than 0.9, however with much greater oxide thicknesses. An initial oxide thickness of 6.8nm at 5min increased to 16nm after 120min. The initial oxidation rate also increased to 6.6nm/min.

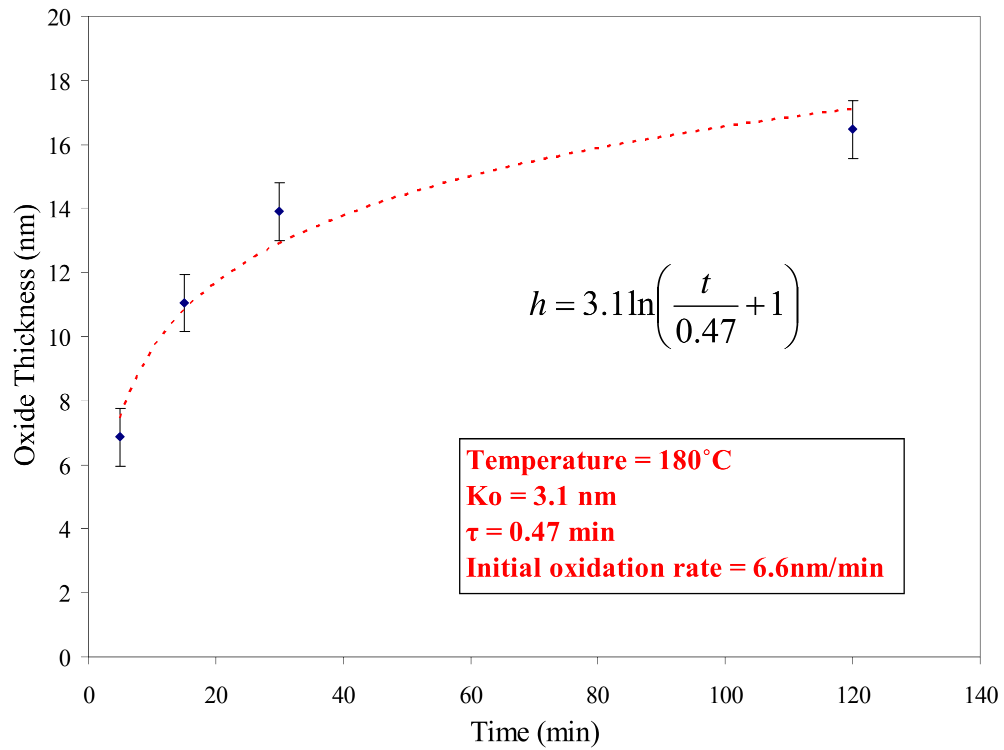

Figure 4.8: Growth kinetics of indium in air at 180˚C.

Finally the kinetics was studied around the reflow temperature of indium, 220˚C. Again the growth rate followed a logarithmic rate law with a correlation coefficient greater than 0.9 as shown in figure 4.9. The initial oxidation rate also increased to 23.8nm/min suggesting both K_o and τ are temperature dependent.

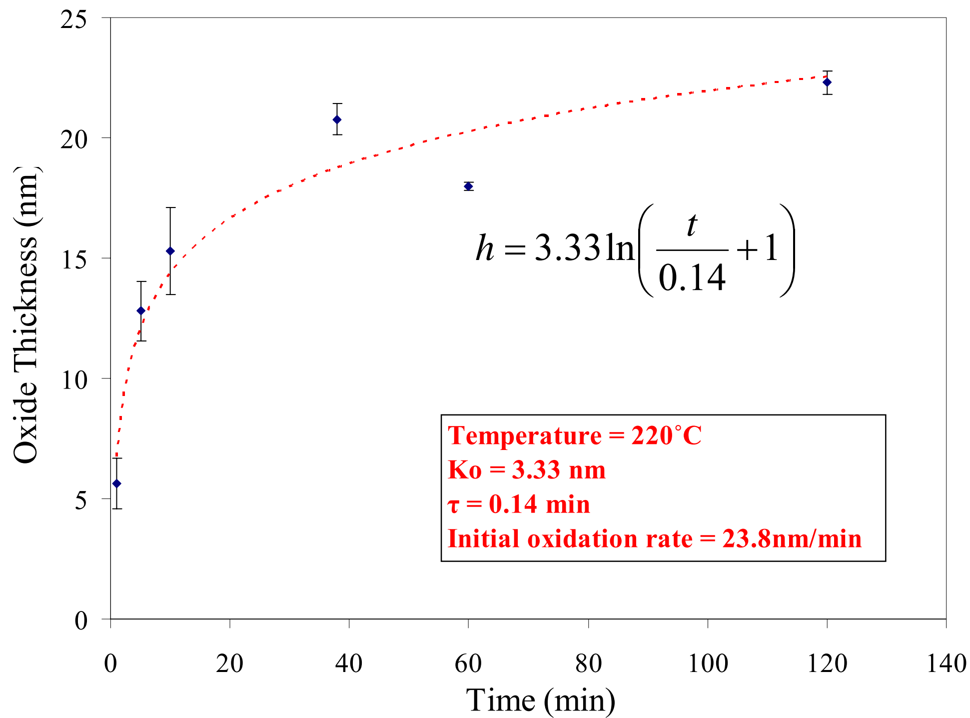

Figure 4.9: Growth kinetics of indium in air at 220˚C.

The physical significance of the logarithmic rate law is the dramatic decrease in oxidation rate with time. If oxidation was solely controlled by the diffusion of ions, oxide thickness would continue to increase with time, instead it reaches an almost steady state before 60min. To explain this phenomenon, Uhlig suggested electronic potential controls the rate of oxidation because of the differing electron affinities of the metal and oxide. Initially oxidation is quite rapid because of the oxide's high electron affinity, however after time, some of the acquired electrons become trapped at lattice defect sites in the oxide lowering the oxide's affinity for electrons, thus slowing the oxidation rate.

4.2.2 Oxidation Kinetics in Glove Box Environment

Oxidation kinetics experiments were also carried out in the glove box. The preliminary results from this experiment are shown in the plots below. It seems there is no discernable pattern in these results since all the values fall within the range of the native oxide layer. So it would be safe to assume the growth kinetics are very slow in such an environment (O_2< .1ppm, H_2O = 2.3ppm, H_2= 4%). Figures 4.10 and 4.11 show the oxidation kinetics of indium in the glove box environment (O_2< .1ppm, H_2O = 2.3ppm, H_2= 4%) at 130˚C and 145˚C respectively.

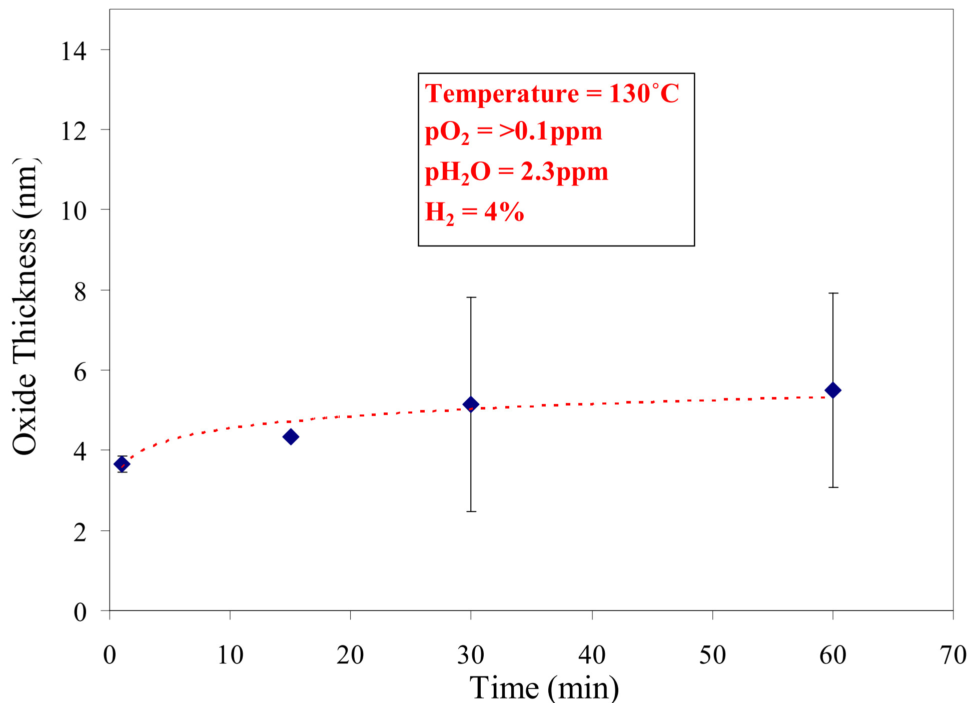

Figure 4.10: Growth kinetics of indium in glove box with pO2 <0.1ppm, pH2O = 2.3ppm, H2 = 4% at 130˚C.

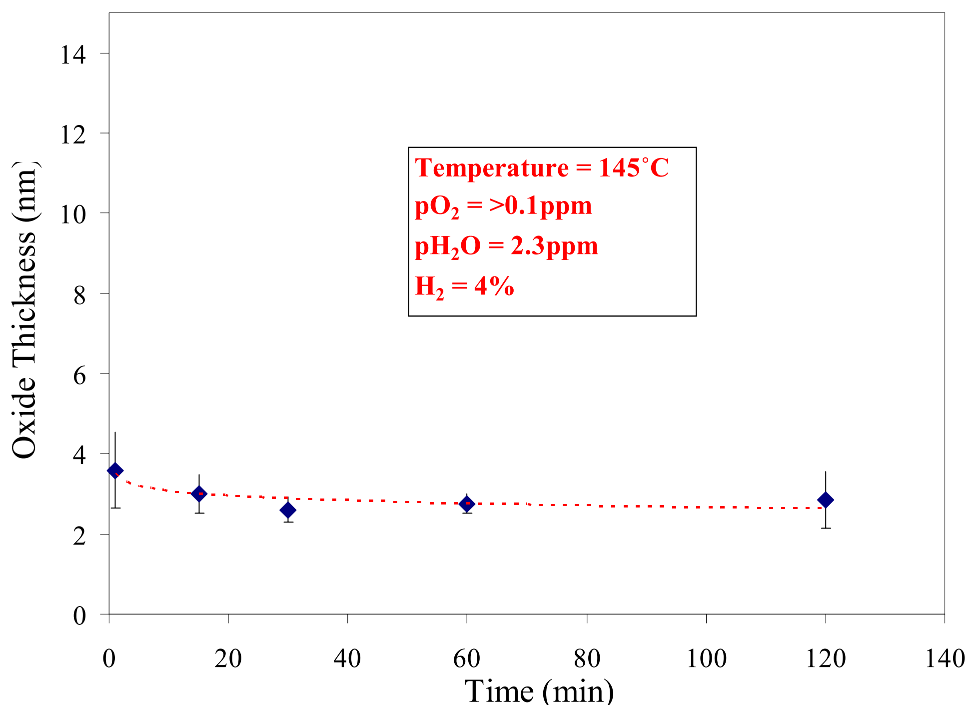

Figure 4.11: Growth kinetics of indium in glove box with pO_2 <0.1ppm, pH_2O = 2.3ppm, H_2 = 4% at 145˚C.

4.3 Activation Energy

To support his theory, Uhlig envoked Rideal and Wansbrough-Jones theory of electron transfer from the metal to an oxygen molecule (Rideal 1929). They found that for most metals, the energy necessary to transfer an electron from the metal to the oxide was given by difference between the metal's work function and the electron affinity of the oxygen molecule.

Applied to the oxidation of indium, because of the large difference in electron affinities of In and In_2O_3 it can be assumed a potential develops across the interface. According to

the Rideal and Wansbrough-Jones activation energy equation, the theoretical activation energy for the oxidation of indium is:

$$E_A = \phi_{In} - 3.6eV$$

$$E_A = 4.12eV - 3.6eV = 0.52eV$$

This result can be compared to the experimentally measured value for activation energy.

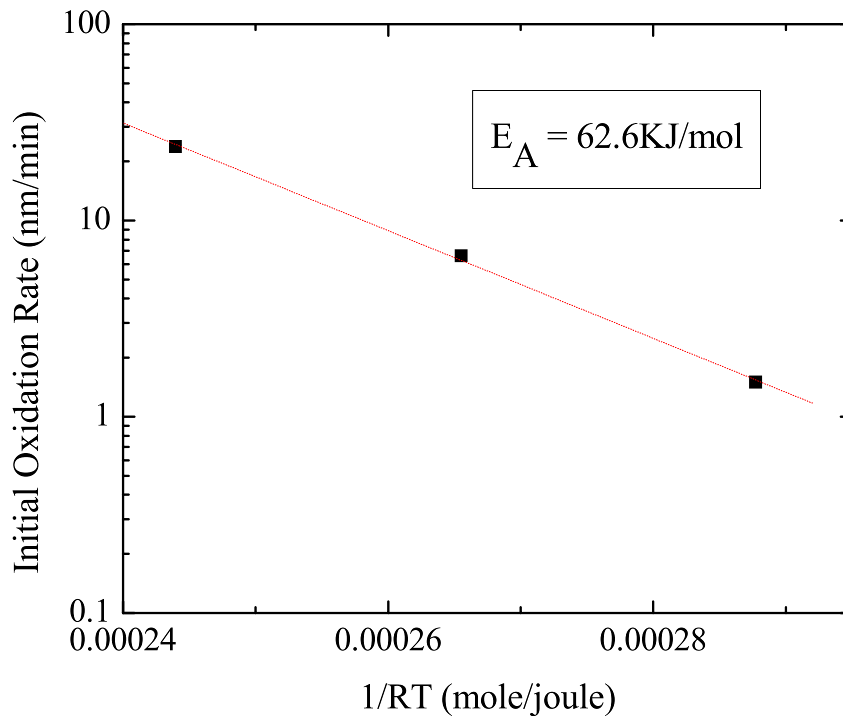

Figure 4.12: Initial activation energy experimentally determined to be 62.6 kJ/mol (0.65eV).

Figure 4.12 is a plot of the initial oxidation rate verses 1/RT to determine the activation energy of the oxidation reaction. The initial oxidation rate was determined from the kinetics curves at 145˚C, 180˚C, and 220˚C. The activation energy, determined from the

slope of the line, was 62.6kJ/mol or 0.65eV which is in reasonable agreement with the theoretically calculated value.

4.4 Reduction of Indium

Disassociation of In_2O_3 occurs when In_2O_3 is thermodynamically unstable relative to In, or when In_2O_3 is physically attacked by bombardment of ions or chemical etchants. As discussed earlier in the thermodynamic section In_2O_3 is very stable in ambient atmosphere because of its large enthalpy. Therefore a combination of a very low pH_2O/pH_2 ratio and high temperature must be used to disassociate In_2O_3 by thermodynamical means. Several studies have shown reduction of indium under auger electron spectroscopy (AES) by detecting a reduction of the I(In)/I(O) signal as a function of time under specific atmospheric conditions. However these studies required the use of a high vacuum 10^{-9}atm and very high temperatures 633K. Another study by Kuhmann et al. was able to reduce the temperature needed to a more practical 523K by introducing extra hydrogen after obtaining a high vacuum atmosphere (Kuhmann 1998).

4.4.1 Reduction of Indium in Glove Box

In this study, reduction was attempted by adding hydrogen to the glove box environment (10^{-7}atm pH_2O) to make In_2O_3 unstable relative to indium at oxygen partial pressures much greater than the equilibrium oxygen partial pressure. Figure 4.13 below shows a thermodynamic map where samples are heat treated. Atmospheric conditions to

the left of the equilibrium curve represent an oxidizing environment, and to the right represent a reducing environment.

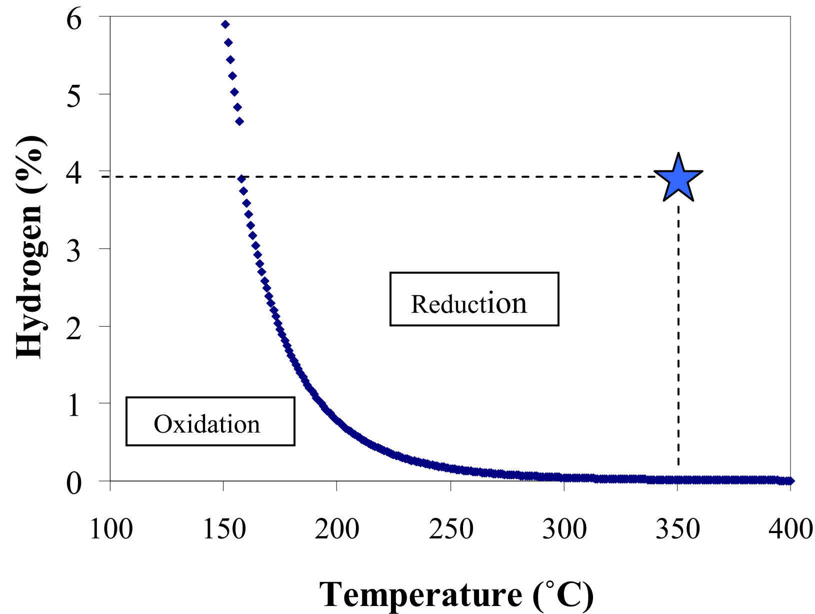

Figure 4.13: Thermodynamic map of indium reduction at 7ppm moisture.

Many experiments were preformed in the reduction zone with no measurable reduction of the oxide layer thickness. Only a harsh reducing environment showed a reduction in the oxide layer. With the temperature set to 623K, H_2 = 4.5%, O_2 < .1ppm, and H_2O = 7ppm the oxide layer was reduced from 21nm to 15nm after 6 hours, yielding an etching rate of 1nm per hour as seen in figure 4.14. This clearly demonstrates the need for very low moisture levels so the temperature can be reduced into an acceptable range. Figure 4.15 is an optical image of indium before and after the reduction experiment.

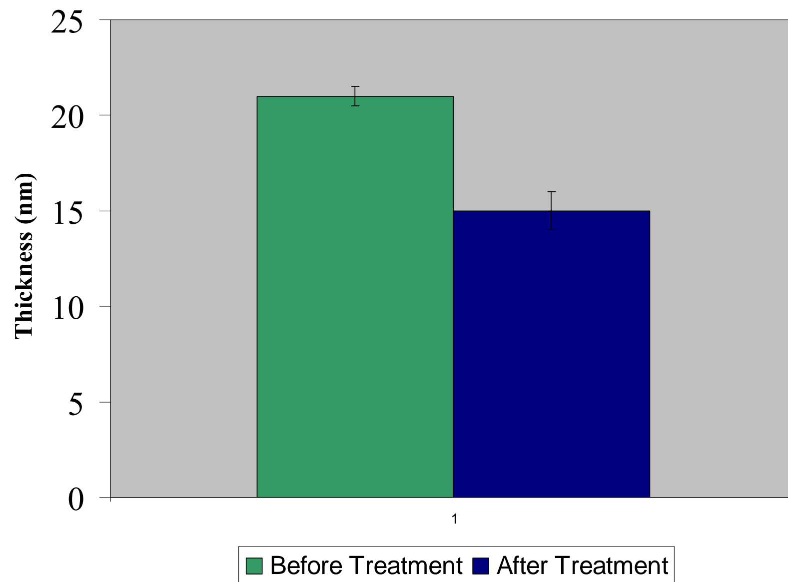

Figure 4.14: Thickness of indium oxide before and after reduction experiment

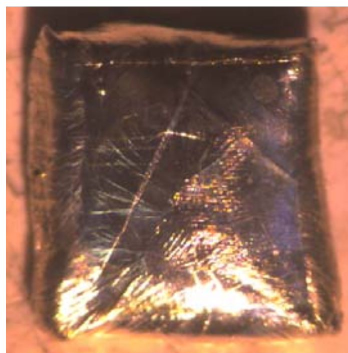

(Before Reduction)

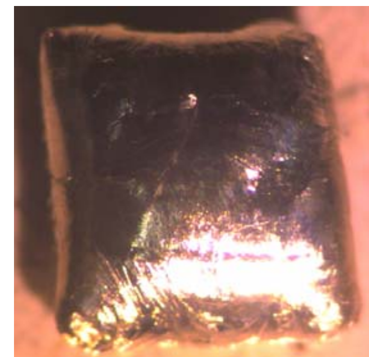

(After Reduction)

Figure 4.15: Stereo-microscope images of indium before and after reduction experiment.

4.4.2 Removal of Indium Oxide using Argon Plasma

Removal of In_2O_3 from a pure indium substrate was also attempted using argon plasma to bombard the sample with ions. Preliminary results from this experiment in the plot 4.16 show an etching rate of 5.3 nm/hr at 270 watts. However it should be noted indium, being high vapor pressure metal, redeposits in the chamber, causing contamination.

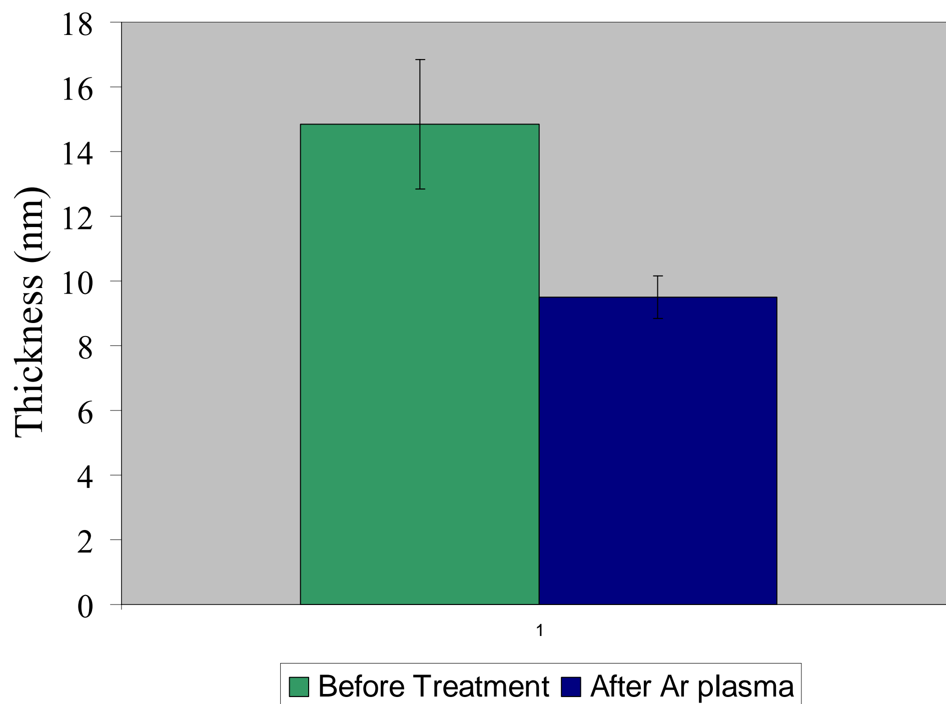

Figure 4.16: Thickness of indium oxide before and after argon plasma treatment at 270 watts for 60 min.

4.5 Microstructure Characterization of Indium and Indium Oxide

Materials characterization of both indium and indium-oxide were carried out using nanoindentation AFM, and optical microscopy. Because of the very large grains of pure indium, only very low magnification optical microscopy was needed to see the structure. Figure 4.17 is an image of the pure indium (99.999%) after electrochemical polishing. Although the grains vary in size, most measured greater than 1mm.

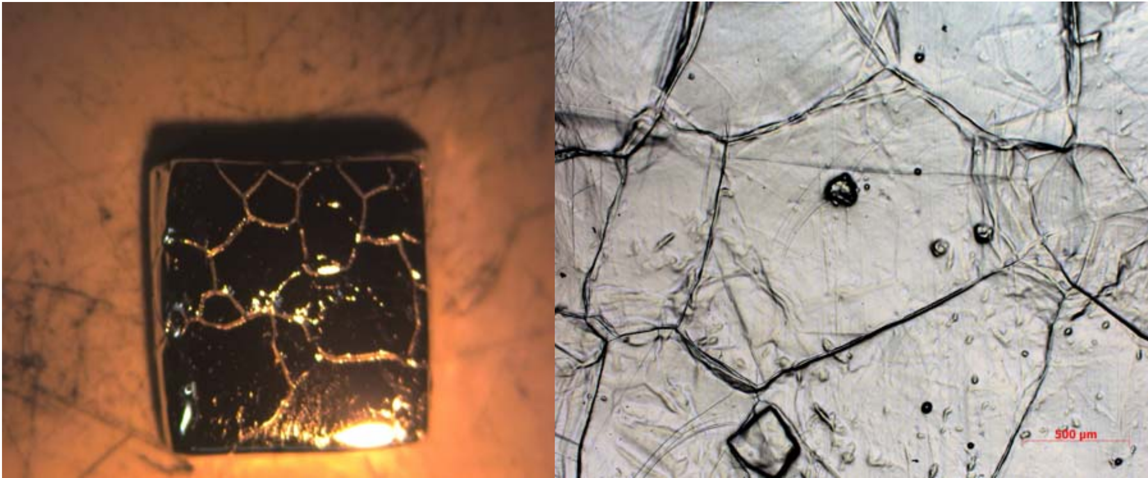

Figure 4.17: Left, Stereo microscope image of electrochemically polished 99.999% pure indium. Right, Optical image of indium grains.

To characterize the microstructure of In_2O_3, In_2O_3 was thermally grown on a pure indium substrate at 1000˚C for several hours. The sample was then imaged under nanoindentation AFM using a Berkovich tip. As seen in figure 4.18 below, the grains of thermally grown (1000˚C) In_2O_3 have an oval morphology and measure from 200-300nm on the long axis and 50nm-100nm on the short axis.

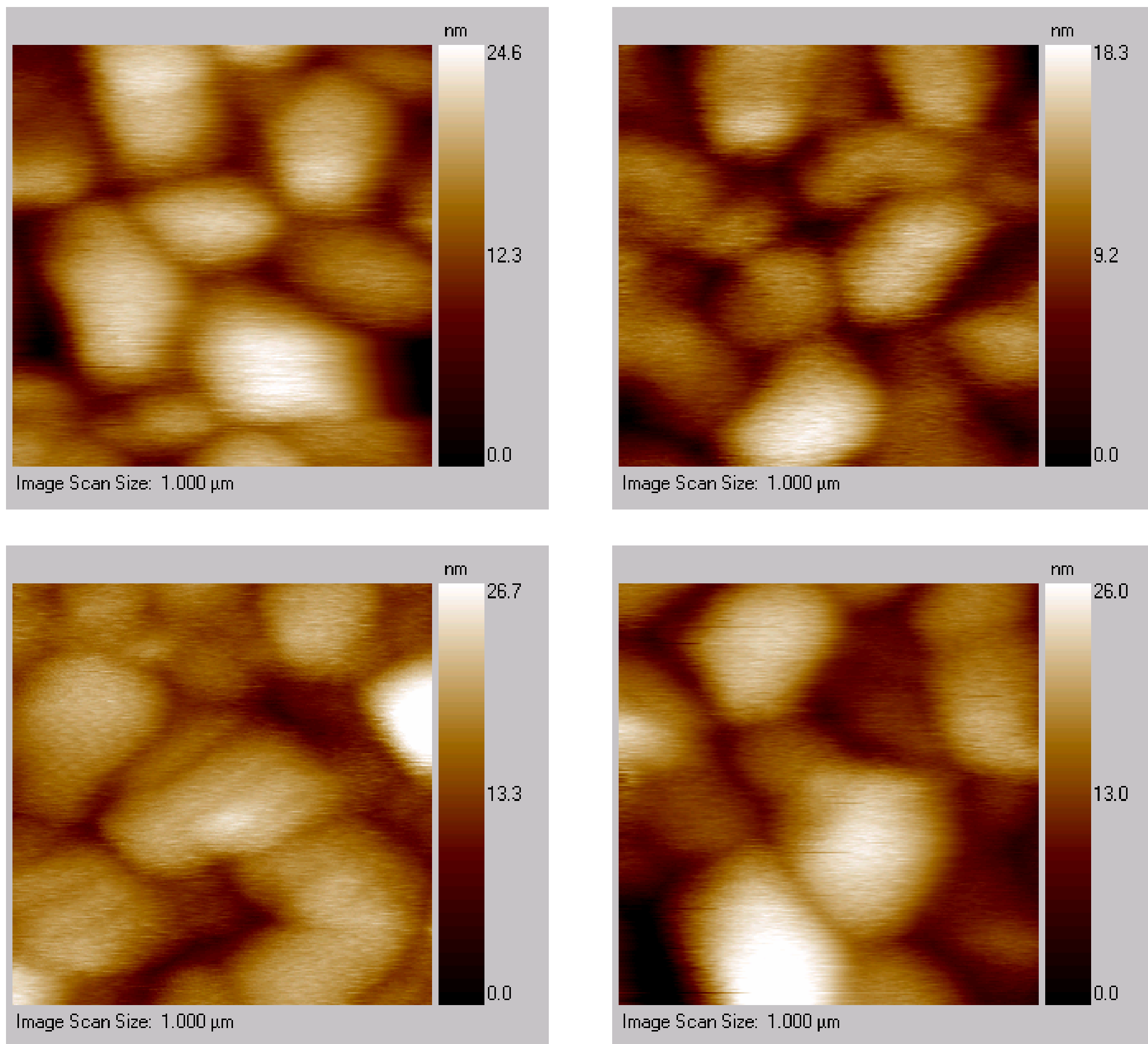

Figure 4.18 : AFM images of indium oxide grown at 1000 ˚C.

4.6 X-ray Diffraction (XRD)

The crystal structure of the thermally grown In_2O_3 and In samples was analyzed using X-ray diffraction. Samples below and above the melting temperature were tested to determine any changes in the crystal structure of indium oxide. Below in figure 4.19 is the resulting X-ray intensity verses 2θ plot for indium annealed below the melting

temperature. It can be seen from these plots, that below the melting temperature no crystalline phase of indium oxide was detected, only pure indium with a tetragonal crystal structure. Therefore, it is believed that indium oxide grown below the melting temperature is of an amorphous nature.

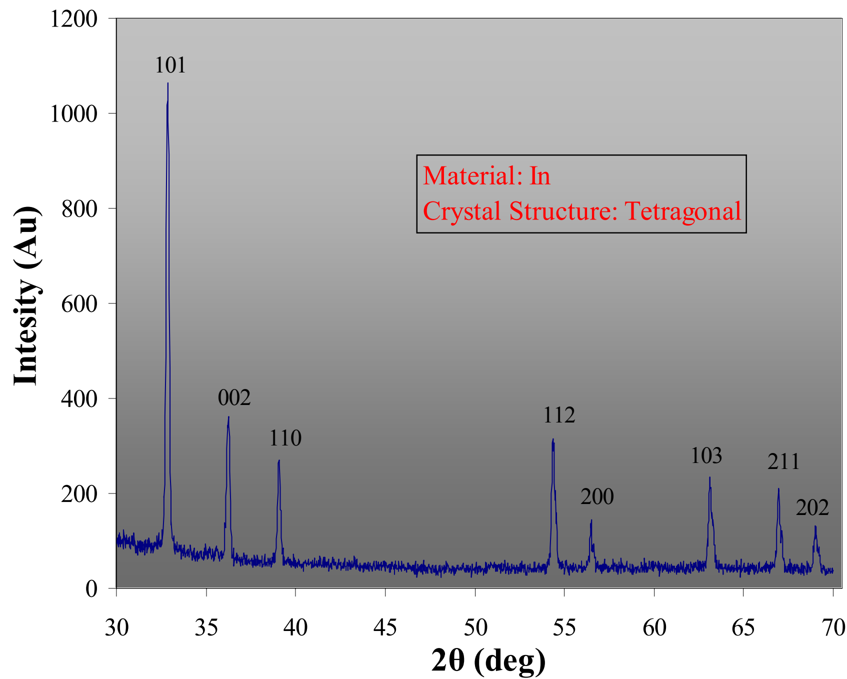

Figure 4.19: XRD plot of intensity verses 2theata for the sample annealed at 153°C for 4 hours. The peaks labeled are from pure indium metal (substrate).

Conversely, when indium was heat treated above the melting temperature a cubic indium oxide crystal structure was detected. Below in figure 4.20 the peaks correspond to a cubic crystal structure for indium oxide when the sample was heat treated for four hours at 200°C. When treated above the melting temp the sample begins to flow resulting in a rough, deformed surface. This may explain the excess “noise” in the plot.

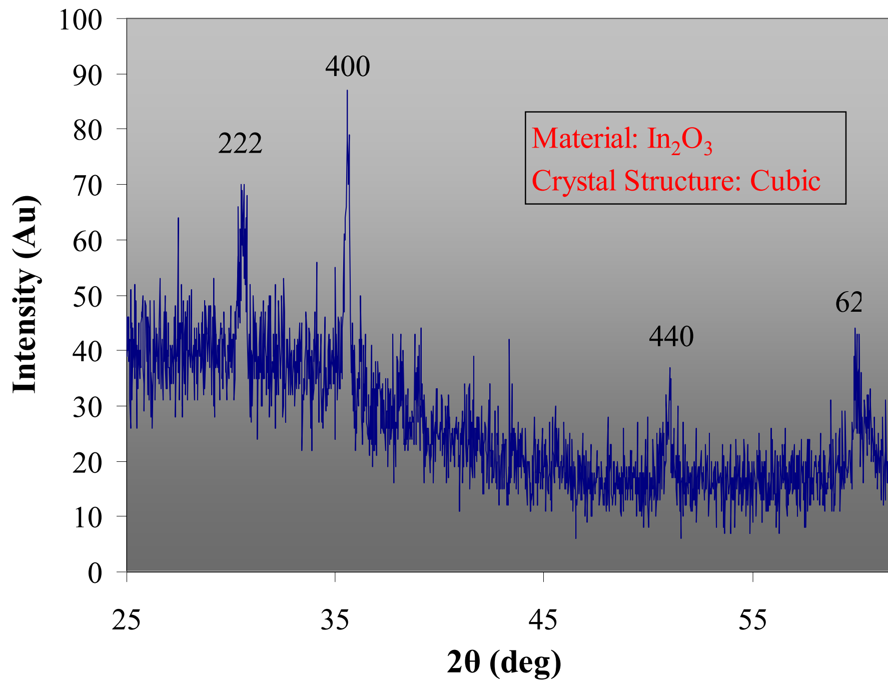

Figure 4.20 : XRD plot of intensity verses 2theata for the sample annealed at 200°C for 4 hours. The peaks labeled are from indium oxide.

4.7 Mechanical Characterization

The reliability of a solder joint is highly dependent on its mechanical behavior. As an electronic package is thermally cycled, the differing thermal expansions of the components introduce stresses on the solder joint which limit its lifetime. Finite element analysis software is typically used to estimate the fatigue life of solder joint assemblies by calculating the total deformation per cycle. However to ensure meaningful model results, accurate temperature-dependent mechanical properties are needed.

Nanoindentation is a convenient tool for this application because many tests can be performed on a very small quantity of material. It is impractical to measure the mechanical properties of indium using conventional tensile tests because of the high cost

of indium. In the present study both elastic modulus and hardness of indium were measured as a function of temperature. Additionally, the time-dependent plasticity of indium was measure by constant load indentation tests.

4.7.1 Optimization of Quasi-Static Nanoidentation Testing Parameters

Quasi-static nanoindentation testing of a sample involves the loading and unloading of a sample under a multi-axial indentation load. For samples which exhibit considerable time-dependent plasticity, the maximum load is held for several seconds to relieve primary creep effects. Testing parameters such as unloading rate and maximum load have considerable influence on the measured values of elastic modulus and hardness. To determine the effect of these parameters on the indentation testing of indium both an unloading rate, and maximum load study was carried out.

Figure 4.21 is a plot comparing the elastic modulus of indium at several different unloading rates. The time was varied from a relatively fast unloading time 1sec, to a slow unloading time of ten seconds. All other testing parameters were held constant to isolate the effects of unloading rate. As seen in figure 4.21 the elastic modulus seems to increase slightly with slower unloading rates, however a more pertinent observation is the increase in error as a function of unloading rate.

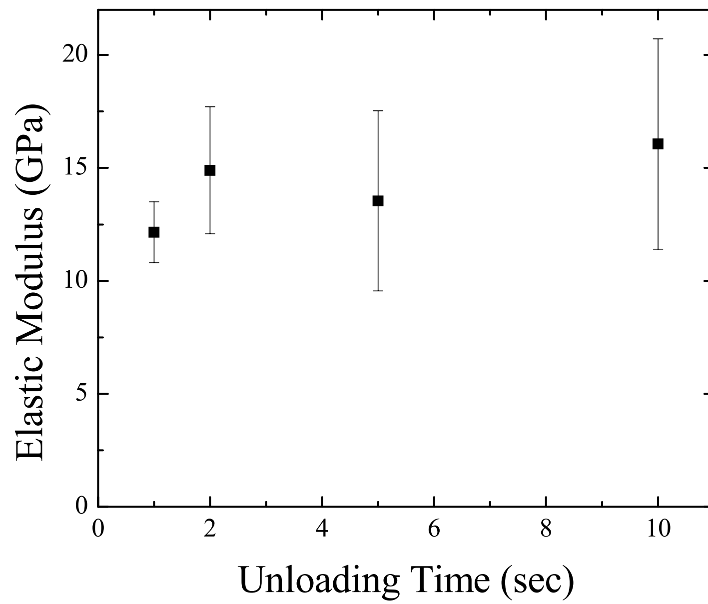

Figure 4.21 : Elastic modulus of indium as a function of quasi-static unloading time.

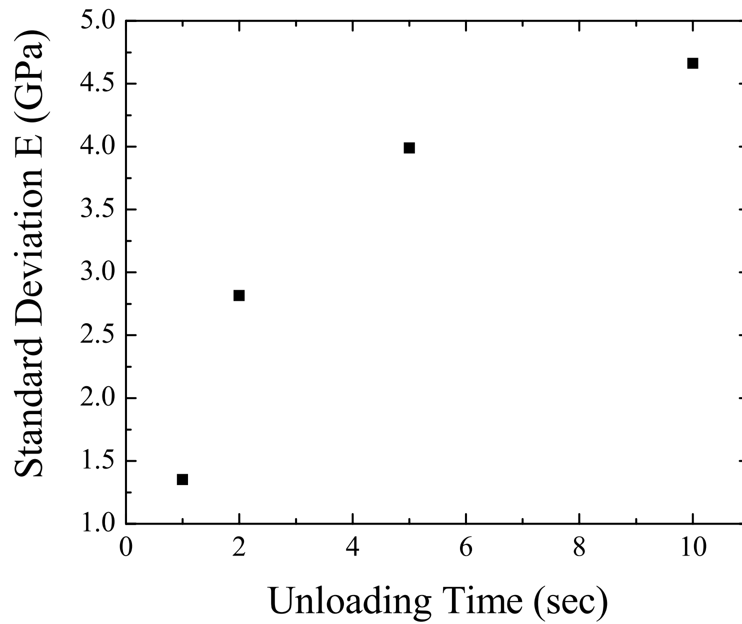

Figure 4.22 : Standard deviation of indium's elastic modulus as a function of quasi-static unloading time.

Figure 4.22 shows the standard deviation in the measured elastic modulus values as a function of unloading time in which the standard deviation steadily increase with unloading time. The cause of increasing scatter can be traced back to the measurement of contact stiffness. As explained earlier the contact stiffness is the measured from the slope of the upper region of the unloading curve. Slower unloading rates lead to more creep during unloading which can alter the shape of the unloading curve. Slight variations in the shape of the unload curve translate into large errors in the measured values. This theory is further confirmed by studying the effect of unloading rate on the hardness of indium.

Figure 4.23 is a plot of the hardness of indium as a function of unloading time. Unlike the measured elastic modulus values, there is much less scatter in the data, and the scatter doesn't show a particular trend. Since hardness is not a function of contact stiffness, and therefore doesn't depend on the slope of the unloading curve, there is less scatter when varying the unloading rate.

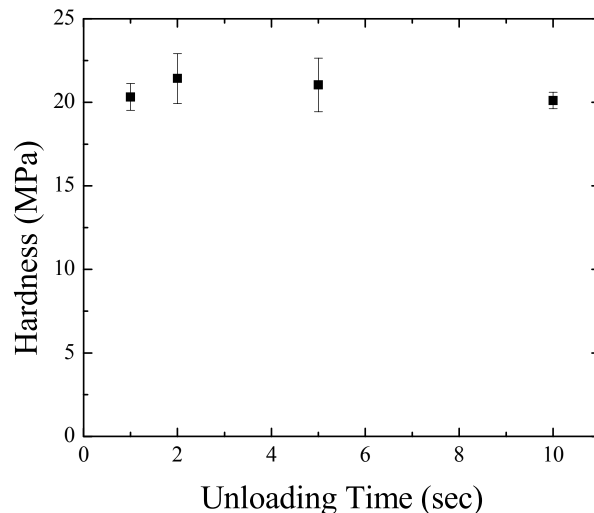

Figure 4.23 : Hardness of indium as a function of unloading time.

The effect of maximum indentation load or indentation depth on measured elastic modulus and hardness values was also studied. Again, all other testing parameters were held constant to isolate the load effect. Figure 4.24 shows the average elastic modulus at 1000μN, 1500μN, 2000μN, 2500μN decreasing slightly with increasing maximum load. One possible explanation is error related to the estimation of the contact depth. The phenomenon known as pile-up occurs when indenting soft materials and material accumulates around the perimeter of the indentation area. This leads to an overestimation of the contact depth and an overestimation of the elastic modulus. Averaging the elastic modulus over the range of max loads results in a value of 12.9GPa which is in good agreement with several studies. The hardness of indium also showed variation with maximum indentation load. Again this is thought to be the result of an error in the estimation of the contact depth. At room temperature the average value for the hardness from 1000μN-2500μN is 17.9MPa as seen in figure 4.25.

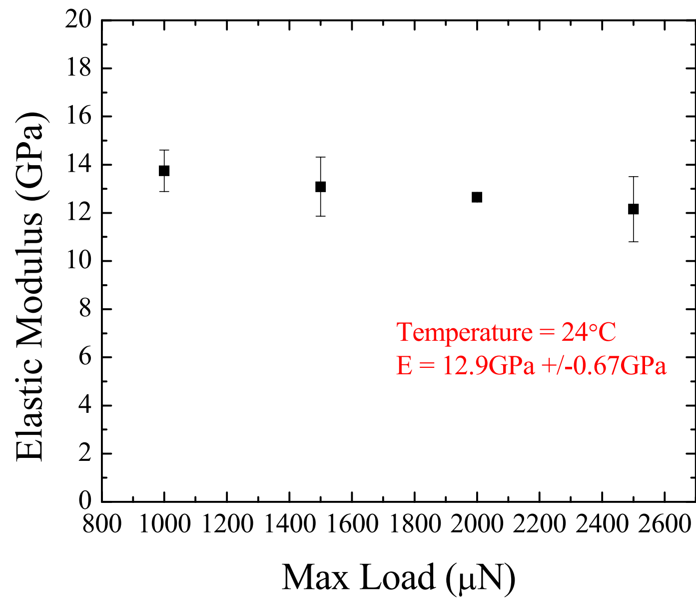

Figure 4.24 : Elastic modulus of indium as a function of maximum load with a unloading time of 1 sec.

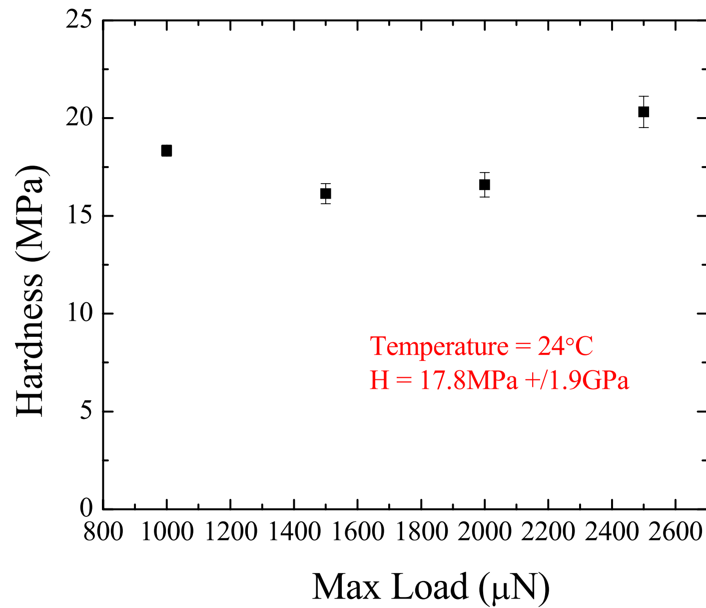

Figure 4.25 : Hardness of indium as a function of maximum load with a unloading time of 1 sec.

4.7.2 In-situ High Temperature Nanoindentation Testing

As temperature increases, the mechanical properties of metals change dramatically. At elevated temperatures, there's more diffusion, additional slip systems become activated, and grains grow, all of which decrease the mechanical strength of metals. To accurately model the mechanical behavior of metals, properties should be measured as a function of temperature.

The mechanical behavior of indium was measured between room temperature and 120˚C in-situ with a specially designed nanoindentation heating stage. The sample was heated to 60˚C, 90˚C, and 120˚C for two hours before testing to allow the temperature to reach a steady state value, and to stabilize the force transducer at elevated temperatures.

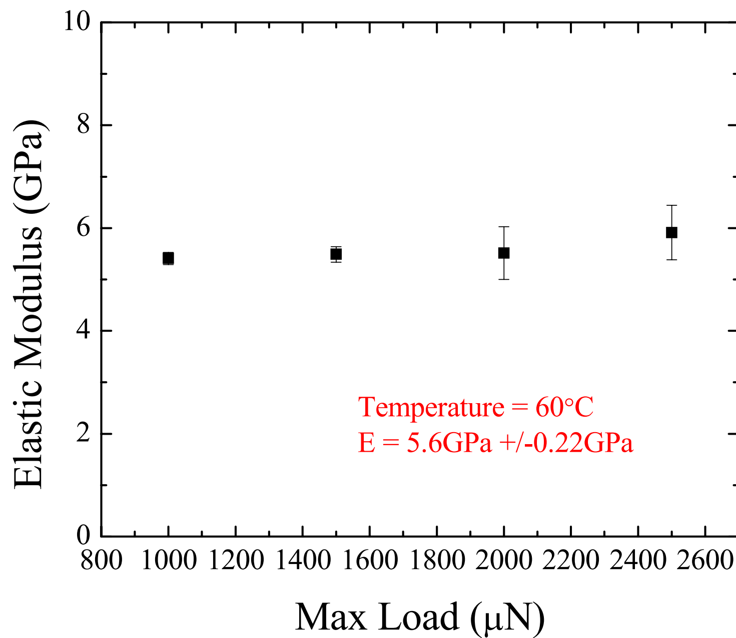

Figure 4.26 : Elastic modulus of indium as a function of maximum load at 60˚C.

Figure 4.26 shows the elastic modulus as a function of load at 60˚C. The average value was calculated to be 5.6GPa +/-0.22GPa, more than a 50% decrease in elastic modulus. Hardness on the other hand decreased at a much slower rate. Figure 4.27 shows an average hardness of 16.2MPa +/-0.16MPa at 60˚C.

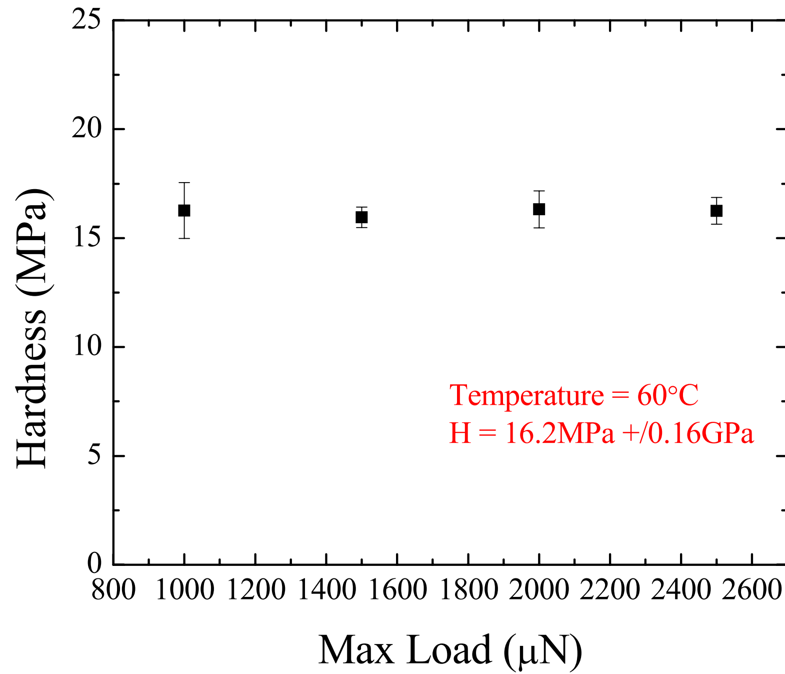

Figure 4.27 : Hardness of indium as a function of maximum load at 60˚C.

The corresponding reduction of elastic modulus and hardness at 90˚C and 120˚C are shown in figures 4.28, 4.29 and 4.30, 4.31 respectively. Indium's elastic modulus decreases to 3.53GPa +/- 0.29GPa at 90˚C and 2.06GPa +/-0.29GPa at 120˚C an 84% decrease in modulus at 0.92Tm. Indium's hardness on the other hand decreases to

12.9MPa +/-0.47MPa at 90˚C and 8.8MPa +/-0.9MPa at 120˚C, only a 51% decrease in hardness at 0.92Tm.

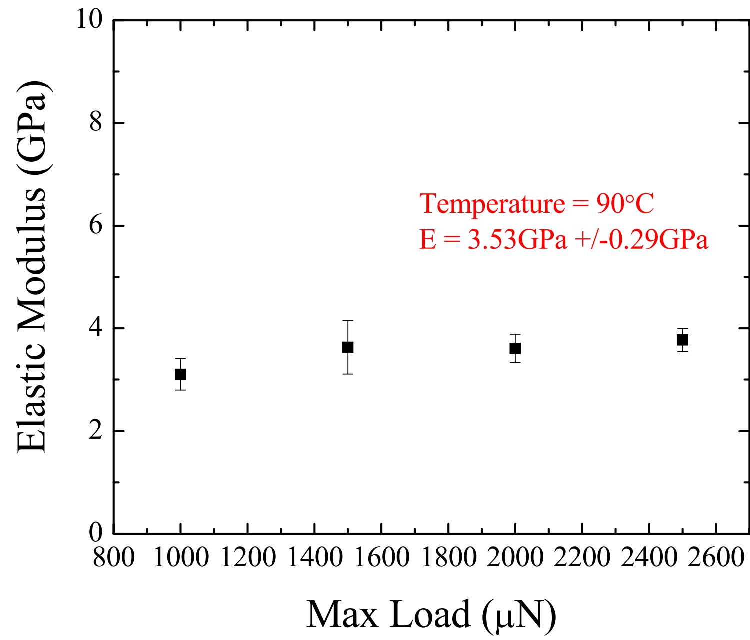

Figure 4.28 : Elastic modulus of indium as a function of maximum load at 90˚C.

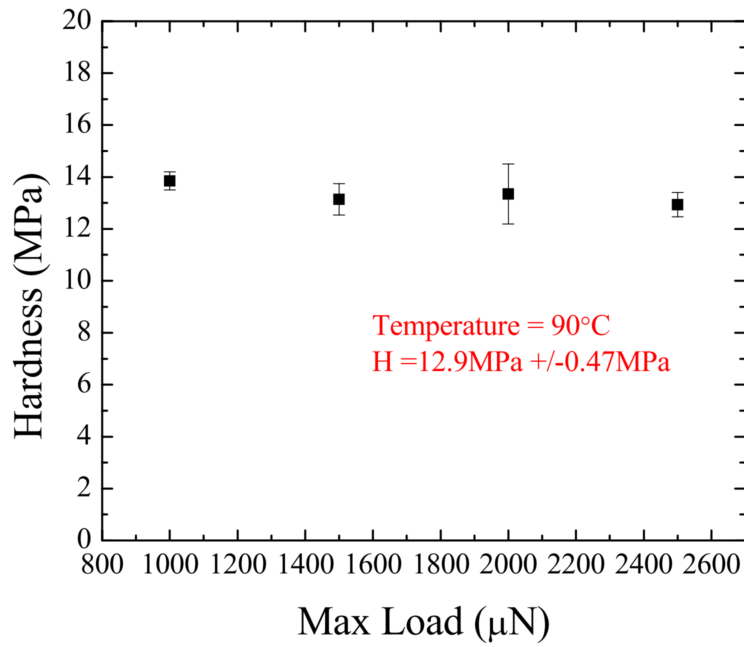

Figure 4.29 : Hardness of indium as a function of maximum load at 90˚C.

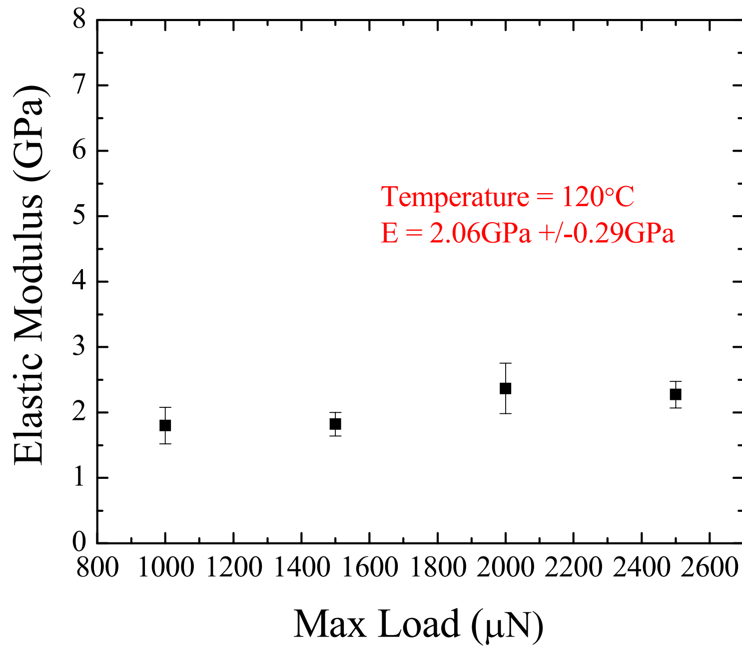

Figure 4.30 : Elastic modulus of indium as a function of maximum load at 120˚C.

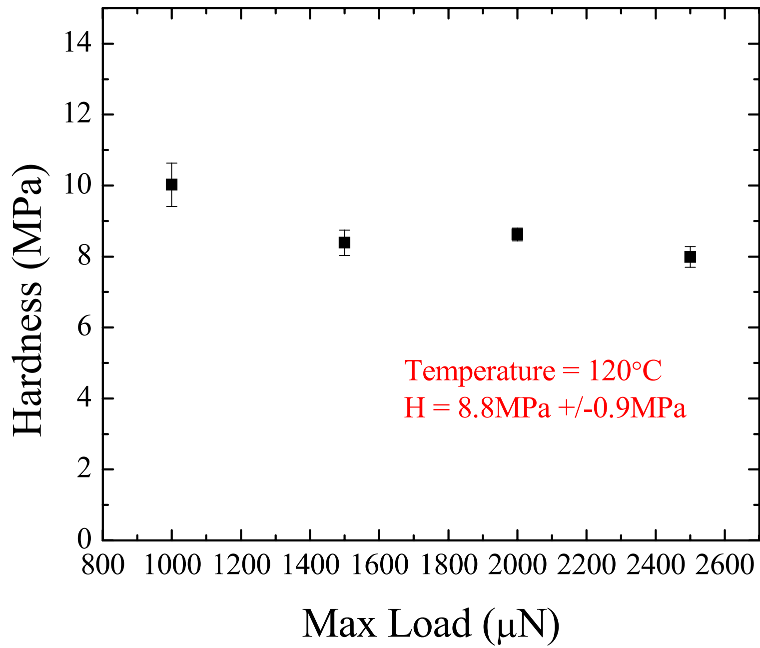

Figure 4.31: Hardness of indium as a function of maximum load at 120˚C.

Combining the high temperature results, a plot of the elastic modulus of indium as a function of temperature is presented in figure 4.32. The data was fitted to a decaying exponential curve with a correlation coefficient greater than 0.99. It should be noted the exponential curve fitting is only valid from 25˚C to 120˚C. Likewise indium's hardness was plotted as a function of temperature in figure 4.33. The decrease in hardness was fitted to a linear curve with a correlation coefficient of 0.96.

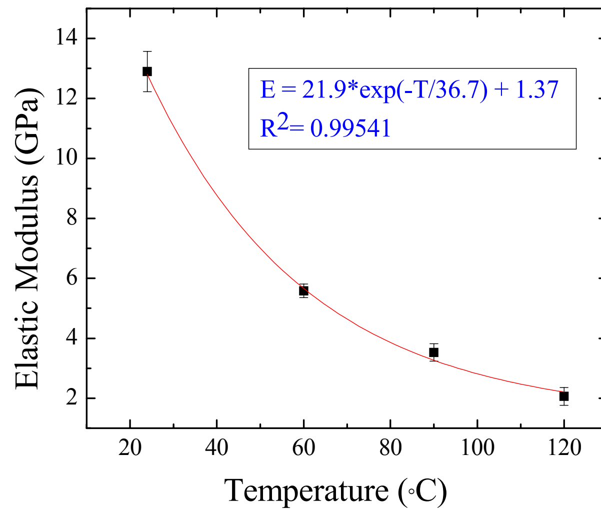

Figure 4.32 : Elastic modulus of indium as a function of temperature.

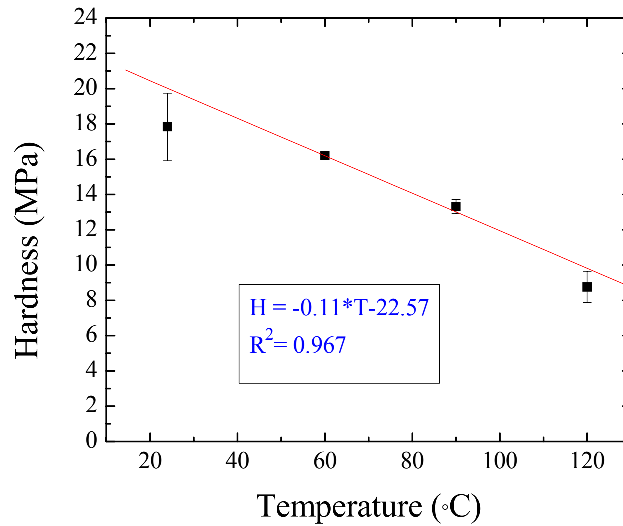

Figure 4.33 : Hardness of indium as a function of temperature.

4.8 Nanoindentation Creep

Nanoindentation was also used to characterize the time-dependent plasticity of indium. Even though nanoindentation creep is a fairly new technique, it offers advantages over standard creep testing in that testing requires significantly less material

and tests are completed in a fraction of the time. The stress exponent, which gives the mechanism of creep, is determined from slope of the log strain/log stress plot. Figure 4.34 is a plot of strain rate verses stress for indium tested at 23˚C. From the average of three tests the stress exponent was calculated to be 6.4. This value suggests dislocation climb as the controlling mechanism according to the power-law relation. Creep experiments were also attempted at elevated temperatures however there was very large scatter in the data. More work is needed to optimize parameters in order to obtain more consistent results.

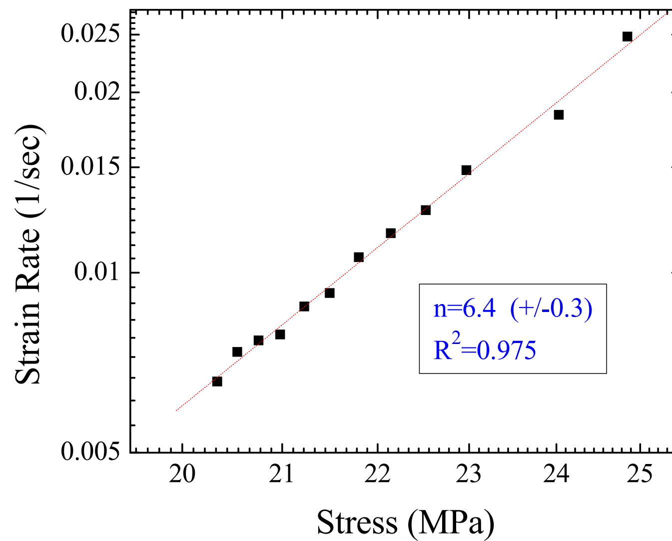

Figure 4.34 : Log-Log plot of strain rate verses stress to determine indium's stress exponent at 23˚C.

4.9 Dynamic Indentation of In_2O_3

Quasi-static nanoindentation has certain limitations in the characterization of materials, this is especial true of thin films. Depending on the thickness of the thin film,

the measured contact stiffness may be dependent on the compliance of the substrate. Some researchers suggest indenting to a depth of no more than 20% of the films thickness, to obtain film only properties, however this method arbitrary, and depends on the compliance of the thin film. For such applications, a continuous stiffness indentation method was developed detect changes in contact stiffness as a function of contact depth [6]. Dynamic nanoindentation superimposes a sinusoidal load on top of a quasi-static load to obtain contact stiffness measurements continuously as a function of displacement. Thus the substrate effect can be monitored by the change modulus and hardness as a function of displacement.

To measure the film only properties of In_2O_3, In was first annealed at 1000˚C to growth several micron thick oxide film. The sample then, was indented at room temperature using dynamic nanoindentation. Figure 4.35 is a profile of the elastic modulus as a function of depth from 100nm to 220nm. After 100nm the elastic modulus is fairly constant showing no substrate effect from the much softer indium base. Averaged from 100nm-220nm the elastic modulus is 105GPa +/-7.6GPa. Although a literature value for the elastic modulus of In_2O_3 has not been found, this number is in good agreement with the measured elastic modulus of indium tin oxide (ITO).

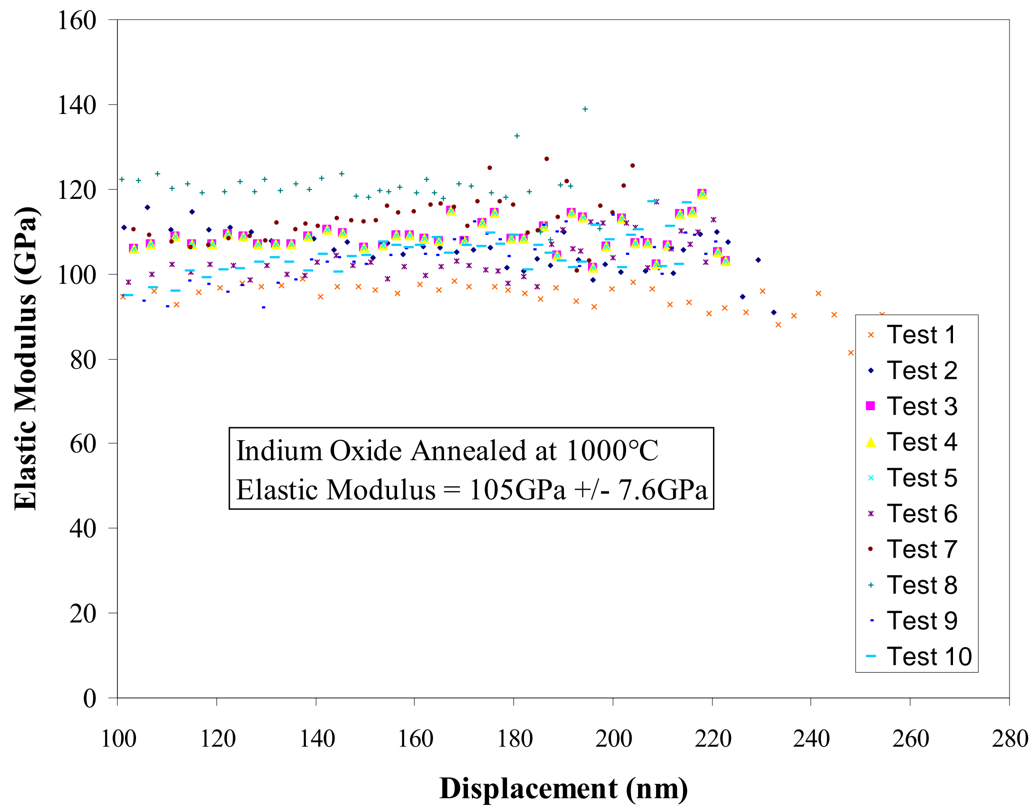

Figure 4.35 : Dynamic nanoindentation plot of elastic modulus of indium oxide verses displacement.

Chapter 5 – Concluding Remarks

The objective of this work was to document and characterize the oxidation behavior of pure indium solder, and to relate it to joint reliability. The first part of the oxidation study focused on the thermodynamics of oxidation and reduction. Using reaction equilibrium, several thermodynamic models were developed precisely indicating the location of the oxidation and reduction zones based on temperature, pO_2, pH_2O, pH_2, pCO, pCO_2.

Creation of a reducing environment using a hydrogen reaction was found to be highly dependent on pH_2O. To reduce indium within a reasonable reflow temperature range (220˚C-300˚C), pH_2O should be kept below 10ppm, to keep the necessary hydrogen concentration below the flammability limit. Reduction of indium using a carbon monoxide reaction was also modeled. Due to the larger enthalpy associated with the carbon monoxide reaction, reduction of indium using carbon monoxide requires a less stringent vacuum, and much lower temperatures. In fact, under a moderate vacuum of 10^{-7} atm less than 0.1% CO is needed to reduce indium at room temperature. It was also shown that oxygen content is not a critical parameter for producing a reducing environment using a H_2 or CO reaction. Increasing the oxygen partial from 1ppm to 500ppm will not significantly shift the location of thermodynamic equilibrium.

Experimental verification of the thermodynamic models was accomplished through oxidation experiments performed in a precisely controlled glove box environment. It was shown that oxidation in a controlled environment agrees quite closely with our thermodynamics model. For the reduction of indium with a hydrogen reaction, the kinetics was found to be very slow in regions close to thermodynamic equilibrium. Only

very harsh conditions (T > 350°C, H_2 > 4%, pH_2O = 7ppm, pO_2 > 0.1ppm) etched In_2O_3. However, by further reducing the moisture content, the service temperature should also be reduced into an acceptable range for faster reduction kinetics. Using the provided thermodynamic program will aid in the search for the proper reflow environment.

The growth rate mechanism in air at 145˚C, 180˚C, and 220˚C was found to fit a logarithmic rate law proposed by Uhlig. There was a time required for onset of oxidation that depends strongly on temperature. Activation energy of the oxidation reaction calculated from the Rideal and Wansbrough-Jones relation (0.52eV) was in agreement with the experimentally determined value (0.62eV), further evidence of initial rate control by electron emission.

The second half of this study involved the mechanical characterization of indium using nanoindentation techniques. Prior to the systematic study of the mechanical properties of indium as a function of temperature, both the quasi-static unloading rate and maximum load were varied to determine their effect on contact stiffness. Unloading rate was shown to have the greatest influence on testing results. Faster unloading rates were found to eliminate creep deformation leading to more reproducible elastic modulus values.

Since the mechanical behavior of metals changes as a function of temperature, both elastic modulus and hardness were tested at 23˚C, 60˚C, 90˚C, and 120˚C using a nanoindentation heating and cooling stage. Indium's elastic modulus decreased roughly 84% when the temperature was increased from 23˚C to 120˚C. Similarly indium's hardness was found to decrease by approximately 50% when the temperature was increased from 23˚C to 120˚C. The relatively smaller decrease in hardness is thought to be a function of nanoindentation's localized indentation volume. Because of the large

size of indium's grains, a localized testing method such as nanoindentation cannot capture the effect of grain growth on mechanical strength.

Lastly, indium's time-dependent behavior was measured using constant load nanoindentation creep tests at 23˚C. Calculated from the log indentation strain rate verses log indentation stress, the stress exponent was measured to be 6.6 in the 17-20MPa stress range. The stress exponent in conjunction with the normalized stress level suggest dislocation climb as the rate controlling mechanism at 23˚C.

Appendix

Thermodynamic Reflow Code:

```
%Harry Schoeller
%Thermodynamic Program
%This program determines whether your environment will oxidize or reduce
%indium solder

Y = input('Welcome To The Indium Solder Reflow Environment Calculator:  Run (1) or
Exit (2):   ');
while Y == 1,
Z = input('\nWhich parameter would you like to hold constant pH20 (1), pH2 (2), pH20
and pH2 (3):   ');
if Z == 1,
    P = input('Enter the total pressure of the system (atm):   ');
  pH201= input('Enter the pH20 (ppm):  ');
  p021= input('Enter the p02 (ppm):  ');
    T1 = input('Enter the reflow temperatue (C):  ');
    p021 = p021* (10^-6);
    pH20 = pH201*(10^-6);
    T = T1 + 273;
    if T <= 430,
        G = 183300 - 151.5*T;
    else
        G = 189300 - 168.1*T;
    end
    H = (pH20/(exp(G/(-8.3144*T))^(1/3)))*100;
    if H > 100,
        fprintf('Indium oxide cannot be reduced with this moisture/temperature
combination, please increase temperature or reduce moisture content');
    else
    fprintf('Your enviroment needs at least %4.4f percent hydrogen gas to reduce indium
oxide', H);
    end
    Y = input('\nWelcome To The Solder Reflow Environment Calculator:  Run (1) or
Exit (2):   ');
elseif Z == 2
   P = input('Enter the total pressure of the system (atm):   ');
   p021= input('Enter the p02 (ppm):  ');
  H= input('Enter the percentage of hydrogen gas:  ');
    T1 = input('Enter the reflow temperatue (C):  ');
    T = T1 + 273;
    if T <= 430,
        G = 183300 - 151.5*T;
```

```
      else
         G = 189300 - 168.1*T;
      end
      pH20 = ((H/100)* (exp(G/(-8.3144*T))^(1/3)));
      p021 = p021* (10^-6);
      ppm = pH20/(.00001);
       fprintf('Your enviroment should contain less than %4.4f ppm H2O to reduce indium
oxide', ppm);
       Y = input('\nWelcome To The Solder Reflow Environment Calculator:  Run (1) or
Exit (2):   ');
elseif Z == 3
    P = input('Enter the total pressure of the system (atm):   ');
    p021= input('Enter the p02 (ppm):  ');
    pH201= input('Enter the pH20 (ppm):  ');
    H= input('Enter the percentage of hydrogen gas:  ');
    pH20 = pH201*(10^-6);
    p021 = p021* (10^-6);
    H1 = H/100;
    T = (-22767.7/(log((pH20/H1)^3)-20.2));
    T2 = T - 273;
    fprintf('Your reflow temperature should be at least %4.2f C  to reduce indium oxide',
T2);
    Y = input('\nWelcome To The Solder Reflow Environment Calculator:  Run (1) or Exit
(2):   ');
end
end
```

References

Armitage, A. F., Liu, H. T., Woodruff, D. P. "Initial oxidation kinetics on cylindrical crystals" *Vacuum*, v 31 (1981): 519-522.
Cardwell, A.B. "Photoelectric and thermionic properties of nickel" *Physical Review*, v 76 (1949): 125-127.
Chatterjee, B. "Metal properties and thin film oxidation" *Thin Solid Films*, v 35 (1976): 397- 404.
Chattopadhyay, B., Measor, J.C. "Uhlig Model of Logarithmic Oxidation" *Scripta Metallurgica*, v3 (1969): 75-76.
Dieter, George. 1986. Mechanical Metallurgy. Boston: McGraw-Hill.
Doerner, M.F., Nix, W.D. "A method for interpreting the data from depth-sensing indentation instruments" *Journal of Materials Research*, v 1, (1986): 601-609.
Eldridge, J.M., Van Der Meulen, Y.J., Dong, D.W. "Analysis of ultrathin oxide growth on indium" *Thin Solid Films*, v 12, (1972): 447-451.
Evans, U.R. "Laws governing growth of films on metals" *Electrochemical Society – Transactions*, v 83 (1943): 336-342.
Farnsworth, H.E., Winch, R.P. "Photoelectric work functions of (100) and (111) faces of silver single crystals and their contact potential difference" *Physical Review*, v 58, (1940): 812-819.
Fehlner F. P. 1981. Low Temperature Oxidation. New York: Wiley-Interscience Publication.
Fehlner, F.P., Mott, N.F., "Low-temperature oxidation" *Oxid Metals*, v 2, (1970): 59-99.
Fromhold, A.T. "Parabolic oxidation of metals" *Physics Letters*, v 29 (1969): 157-158.
Gaskell, David. 2003. Introduction to the Thermodynamics of Materials (4th edition). New York: Taylor & Francis.
Geller, Joseph, Engle, Paul, "Sample preparation for electron probe microanalysis – Pushing the limits" *Journal of Research of the National Institute of Standards and Technology*, v 107, (2002): 627-638.
Graham, M. J., Hussey, R. J., Cohen, M. "Influence of oxide structure on the oxidation rate of nickel single crystals" *Journal of the Electrochemical Society*, v 120 (1973): 1523-1529.
Graham, M.J., Ali, S.I., Cohen, M., **"**Low temperature oxidation (24° to 200°C) and krypton adsorption studies on polycrystalline and single crystal iron surfaces" *Journal of the Electrochemical Society*, v117 (1970): 513-516.
Hendrix V., Cox, P.A. 1994. The Surface Science of Metal Oxides. New York: Cambridge University Press.
Houdremont, E., Rudiger, O. *Naturwiss*, v39, (1952).
Humpston, Giles, Jacobson, David M. "Indium solders" *Advanced Materials and Processes*, v 163 (2005): 45-47.
Kim, J., Schoeller, H., Cho, J., Park S. "Effect of oxidation on indium solderability", *Journal of Electronic Materials*, (2007).
Kubaschewski, O., Hopkins, B. 1962. Oxidation of Metals and Alloys (2nd Edition). New York: Academic Press Inc.
Kuhmann, J., Preuss, A., Adolphi, B., Maly, K., Wirth, T., Oesterle, W., Pittroff, W., Weyer, G., Fanciulli, M. "Oxidation and Reduction Kinetics of Eutectic SnPb, InSn,

and AuSn: A Knowledge Base for Fluxless Solder Bonding Applications" *IEEE Transactions on components, packaging, and manufacturing technology,* v21 (1998).

Li, X., Bhushan, B. "A review of nanoindentation continuous stiffness measurement technique and its applications" *Materials Characterization*, v 48, (2002): 11-36.
Lucas, B.N., Oliver, W.C. "Indentation power-law creep of high-purity indium" *Metallurgical and Materials Transactions A (Physical Metallurgy and Materials Science)*, v 30A, (1999): 601-610.
Measor, J.C., Afzulpurkar, K.K. "Initial oxidation rate of pure iron and effect to curie temperature" *Philosophical Magazine*, v 10, (1964): 817-826.
Mil'shtein, S., Parsey, John M. Jr., Lang, David V., Joy, David C., Temkin, Henryk "Low-stress low-temperature micro-soldering technique for making electrical contacts to semiconductor crystals and thin film materials" *IEEE Transactions on Components, Hybrids and Manufacturing Technology*, v CHMT-8, (1985): 397-402.
Oliver, W.C., Pharr, G.M. "Improved technique for determining hardness and elastic modulus using load and displacement sensing indentation experiments" *Journal of Materials Research*, v 7 (1992): 1564-1580.
Rhodin, T.N. "Low Temperature Oxidation of Copper" *J. Amer. Chem. Soc.,* v73, (1951).
Rideal and Wansbrough-Jones "An Investigation of the Combustion of Platinum" *Proc. Roy. Soc*. v123A, (1929).
Rocaries J. C. "Oxidation of pure nickel around the curie point" *Scripta Metallurgica*, v5 (1971).
Schottky, *Phys. Rev*.,' vol. 31, p. 236 (1928).
So, W.W., Lee, C.C. "Fluxless process of fabricating In-Au joints on copper substrates" *IEEE Transactions on Components and Packaging Technologies*, v 23 (2000): 377-382.
Tammann, G., Vogel, R. "The tenary system iron-boron-carbon" *Zeitschrift fur Anorganische und allgemeine Chemie*, v 123, (1922): 225-275.
Tick, P.A.,Witt, A.F. "Computational approach to equilibrium relaxation in central force systems" *Surface Science*, v 26 (1971): 165-183.
Uhlig, H. "Initial Oxidation Rate of Metals and the Logarithmic Equation" *Acta Metallurgica*, v4, (1956).
Wable, Girish S., Chu, Q., Damodaran, P., Srihari, K. "A systematic procedure for the selection of a lead-free solder paste in an electronics manufacturing environment" *Soldering and Surface Mount Technology*, v 17 (2005): 32-39.
Wagner, C., *Z. phys. Chem*. 21B, (1933).
Wagner, Jr., J.B., Lawless, K.R., Gwathmey, A.T. "Rates of formation and structure of oxide films formed on single crystal of iron" *Metallurgical Society of American Institute of Mining, Metallurgical and Petroleum Engineers -- Transactions*, v221 (1961): 257-261.
West, A. 2005. Basic Solid State Chemistry. New York: John Wiley & Sons, LTD.
Yaws, C. L. 1999. Chemical properties handbook : : physical, thermodynamic, environmental, transport, safety, and health related properties for organic and inorganic chemicals. New York: McGraw-Hill.